Towards High Performance Lithium-ion Batteries using Crumpled Graphene-Protected Silicon Anodes

by

Zimin She

A thesis

presented to the University of Waterloo

in fulfillment of the

thesis requirements for the degree of

Doctor of Philosophy

in

Chemical Engineering (Nanotechnology)

Waterloo, Ontario, Canada, 2021

Examining Committee Membership

The following served on the Examining Committee for this thesis. The decision of the Examining Committee is by majority vote.

External Examiner	Dr. Xiaolei Wang Assistant Professor
Supervisor(s)	Dr. Michael Pope Associate Professor
Internal Member	Dr. Jeff Gostick Associate Professor
Internal Member	Dr. Germán Sciaini Associate Professor
Internal Member	Dr. Aiping Yu Associate Professor

Author's Declaration

This thesis consists of material all of which I authored or co-authored: see Statement of Contributions included in the thesis. This is a true copy of the thesis, including any required final revisions, as accepted by my examiners.

I understand that my thesis may be made electronically available to the public.

Statement of Contributions

The main works in this thesis can be divided into three manuscripts which are under review or ready for submission, the statement of contributions for each work is briefly listed as below

Chapter 3 is adapted from:

Z. She, M. Gad, Z. Ma, Y. Li and M. A. Pope. "Enhanced Cycle Stability of Crumpled Graphene Encapsulated Silicon Anodes via Polydopamine Sealing". *ACS Omega,* 6 (18), 12293-12305, 2021.

- Z. She planned and performed all experiments and wrote the manuscript draft.
- M. Gad, Z. Ma, Y. Li and M. A. Pope helped plan experiments and reviewed the manuscript.

Chapter 4 is adapted from:

Z. She, M. Uceda and M. A. Pope. "Controlling Void Space in Crumpled Graphene-Encapsulated Silicon Anodes using Sacrificial Polystyrene Nanoparticles". (Submitted to ChemSusChem, just accepted)

- Z. She planned and performed all experiments and wrote the manuscript draft.
- M. Uceda and M. A. Pope helped plan experiments and reviewed the manuscript.

Chapter 5 is adapted from:

Z. She, M. Uceda and M. A. Pope. “Controlling void space in crumpled graphene using responsive hydrogels for stable silicon anodes”. (Ready for submitting)

- Z. She planned and performed all experiments and wrote the manuscript draft.
- M. Uceda and M. A. Pope helped plan experiments and reviewed the manuscript.

Other Published Contributions Beyond the Scope of this Thesis:

Z. Ma, X. Gao, **Z. She**, M. A. Pope and Y. Li. “Ultrasmall TiOx Nanoparticles Rich in Oxygen Vacancies Synthesized through a Simple Strategy for Ultrahigh‐Rate Lithium‐Ion Batteries”, ChemElectroChem 7.19 (2020): 4124-4130.

J. Chen, WR. Walker, L. Xu, O. Krysiak, **Z. She** and M. A. Pope, “Intrinsic Capacitance of Molybdenum Disulfide”, ACS nano 14.5 (2020): 5636-5648.

U. Farooq, S. Rehman, **Z. She** and M. A. Pope, “Cross-linked Si-C framework: a stable (de)lithiation material for energy storage”, which is ready for submission.

Abstract

Despite silicon being a promising candidate for next-generation lithium-ion battery anodes due to its high theoretical capacity of 3590 mAh/g ($Li_{15}Si_4$, at room temperature), self-pulverization and the formation of an unstable solid electrolyte interface, caused by the large volume expansion during lithiation/delithiation, have slowed its commercialization. To overcome these challenges, this thesis aims to design a stable and deformation-resistant crumpled reduced graphene oxide (rGO) shell to accommodate the severe volume expansion/shrinkage of silicon during lithiation/delithiation and meanwhile limit the exposure of fresh silicon surface to the electrolyte.

In the first experimental chapter, a comprehensive study was conducted to understand the effect of basic spray drying conditions (including nitrogen flow rate, dispersion concentration and mass ratio of rGO/silicon) on the physical morphology and electrochemical performance of the resulting electrode material. Although the optimized crumpled structure exhibited significantly improved rate performance and cyclic stability, it was hypothesized that the crumpled rGO shell may not be mechanically robust enough or leak-tight enough to buffer the volume expansion alone and prevent direct exposure of the electrolyte to the silicon anode. Therefore, we further expanded on the crumpled rGO approach by sealing the graphene shell with an additional layer of polydopamine. As demonstrated by a significant improvement to the initial coulombic efficiency (76.3% from 57.2% for the bare silicon control) and a remarkable cycle life with the anodes exhibiting a capacity of 1038 mAh/g after 200 cycles at 1 A/g, this approach indeed improved the structural stability of the shell and helped to reduce the amount of solid electrolyte interface

(SEI) formed. The resulting composite displayed a high capacity of 1672 mAh/g at 0.1 A/g and can still retain 58% when the current density was increased to 4 A/g. This work established a comprehensive understanding of the importance of spray drying conditions and how to affect the resulting morphology and battery performance, which layed the foundation for the later thesis chapters.

Building on this approach, it was recognized that graphene tightly wraps around the silicon core during the spray drying process and provides little void space for volume expansion of the silicon. Thus, a simple strategy was developed to engineer void-space within the rGO framework which was used to buffer the volume change of Si nanoparticles by incorporating varying amounts of similarly sized polystyrene (PS) nanoparticles in the spray drier feed mixture. The PS completely decomposes during thermal reduction of the GO shell and results in Si cores of varying porosity. The best performance is achieved at a 1:1 ratio of PS/Si, leading to high capacities of 1638 mAh/g, 1468 mAh/g, and 1179 mAh/g at 0.1 A/g, 1 A/g, and 4 A/g, respectively. Moreover, at 1 A/g, the capacity retention was 80.6% after 200 cycles. At a practical active material loading of 2.4 mg/cm^2, the electrodes could achieve an areal capacity of 2.26 mAh/cm^2. This work further improved the resulting cyclic stability compared to the first work, especially at high mass loading, suggesting that the reserved void space is important even after graphene encapsulation. Moreover, the rate capability was found to be much better after the introduction of an optimal amount of void space, which may have been a result of a thinner, more Li-ion permeable shell and an improved distribution of rGO within the core. The method also reduced the number of processing steps compared to the polydamine sealing approach. However, it still required a

high-temperature heat treatment to 800°C and slow ramp rate which negatively impacts potential manufacturability.

To eliminate the slow and energy-intensive high temperature step, a novel method was developed whereby a responsive poly (ethylene oxide) - carboxymethyl cellulose hydrogel was incorporated into the core of the crumpled rGO framework during spray drying. Taking advantage of the volume change of the hydrogel in the hydrated vs. dehydrated state, we demonstrated the ability to control the void space within the core which can be spontaneously created by immersion of the powder in water and "locked-in" upon chemical reduction of the GO shell. In this design, the strong interaction between the polymer core and the silicon and rGO and its ionic conductivity were expected to lead to improved performance. This composite displayed impressive cyclic stability, which retained ~ 81.7% of the initial capacity (1055 mAh/g after 320 cycles at 1 A/g with active material loading of 1 mg/cm^2. Even at an increased mass loading (2.5 mg/cm^2), the areal capacity of this material only dropped from 2.04 mAh/cm^2 to 1.61 mAh/cm^2 after 200 cycles at 1 A/g. While the rate performance of this composite was not as impressive as the high temperature case, we believe that the low temperature, higher-throughput, aqueous processing method and significantly enhanced cycle-life make the resulting composite promising for commercial applications.

Acknowledgements

First, I would like to sincerely thank my supervisor Dr. Michael Pope, who always supports and inspires me in the last six years. I am grateful for his encouragement to help me overcome various difficulties in my graduate study and his patient guidance to make me gradually grow into a capable researcher.

Next, I would like to thank all of my committee members, Dr. Xiaolei Wang from the University of Alberta, Dr. Germán Sciaini, Dr. Jeff Gostick and Dr. Aiping Yu from the University of Waterloo, for their wise suggestions and comments.

I would like to greatly appreciate all my friends and colleagues in this country, who gave me lots of suggestions, inspiring me to do better works in these years. I do not think I could have done all of these works without their support and encouragement. Thanks for all of them being with me,

I would also thank my parent, who always support me unconditionally. Because of their protection, I can freely pursue my dreams anytime and anywhere.

Finally, and most importantly, I would like to thank my girlfriend Lina Chu, who has been doing the utmost to support and love me in all these four years since she has come into my life. Her company is my biggest motivation to move forward. I owe her everything.

Table of Contents

List of Figures

List of Tables

List of Abbreviations

AES	Auger electron spectroscopy
BET	Brunauer-Emmett-Teller surface area analysis
CNT	Carbon nanotube
cpDOPA	Carbonized poly(dopamine)
CVD	Chemical vapor deposition
DVS	Dynamic vapor sorption
EDXS	Energy-dispersive X-ray spectroscopy
EELS	Electron energy loss spectroscopy
FTIR	Fourier-transform infrared spectroscope
Gel	Hydrogel
GO	Graphene oxide
rGO	Reduced graphene oxide
crGO	Crumpled reduced graphene oxide
HF	Hydrofluoric acid
KPS	Potassium persulfate
MPS	3-(trimethoxysilyl) proply methacrylate
OCV	Open circuit voltage
Pe	Peclet number
SEI	Solid electrolyte interface
SEM	Scanning electron microscope
SSA	Specific surface area
TEM	Transmission electron microscopy
HRTEM	High-resolution transmission electron microscopy
TGA	Thermogravimetric analysis
XRD	X-ray diffraction

1 Introduction

1.1 Background and Motivation

In December 2015, 195 countries adopted the first-ever universal, legally binding global climate change agreement at the twenty-first session of the Conference of the Parties (COP21).[1] To avoid accerlating climate change and in an attempt to get the global climate back on track, COP21 developed a global action plan for all countries to limit the global temperature rise to below 2°C and pursue efforts to limit it to 1.5°C compared to the pre-industrial level. Before the Industrial Revolution,[2] the concentration of carbon dioxide (CO_2) in the atmosphere was 280ppm (0.028%), which is also the average level for most of human history. However, the current concentration has exceeded 400 ppm (0.04%), hence limiting carbon emissions has become the key to addressing this global environmental crisis.

The utilization of fossil fuels is the primary source of excess carbon emissions from human activities. According to the Fifth Assessment Report (AR5) released by the Intergovernmental Panel on Climate Change (IPCC) in 2014,[3] the combustion of fossil fuels and industrial processes contributed more than 78% of the total greenhouse gas emissions increase from 1970 to 2011. Hence, in order to effectively reduce the global annual carbon emissions, it is imperative to develop renewable energy sources (such as wind, solar, etc.)[4] as well as corresponding advanced energy storage technologies to substitute traditional fossil fuels. Electrochemical energy storage devices such as lithium-ion batteries have begun to enable advances toward these goals.[5, 6] Actually lithium-ion batteries have already

become ubiquitous in modern daily life and serve as the power source for nearly all smart phones and laptops.[7] However, for applications requiring higher energy density,[8] such as pure or hybrid electric vehicles,[9] lithium-ion batteries are still not sufficient to completely replace traditional internal combustion engines due to their cost, short distance per charge, long charging times, fast decay of battery capacity, and various safety issues. Therefore, in order to accelerate the adoption of these various clean technologies, more advanced Li-ion batteries with higher energy densities, longer cyclic stability, lower costs and improved safety performance are required.

The anode material is one of the key factors determining the performance of lithium-ion batteries. Different anode materials can achieve lithium storage by 1) intercalation, 2) alloying or 3) conversion reactions.[10] At present, most commercial lithium-ion batteries use graphite anodes.[11] Although the graphite anode has outstanding cyclic stability, rate capability and safety, its theoretical capacity is only 372mAh/g,[12] which significantly restricts the overall theoretical capacity of lithium-ion batteries. Therefore, we need to study new anode materials to replace graphite, thus breaking one of the main bottlenecks limiting the energy density of commercial lithium-ion batteries. Silicon, which is regarded as one of the most promising candidates to substitute graphite for next-generation lithium-ion batteries, converts electrical energy into chemical energy by reacting with lithium ions to form a Li-Si alloy.[13, 14] Silicon has a much higher theoretical capacity (3590 mAh/g) at room temperature than that of graphite (372 mAh/g) and has a low nominal half-cell potential (~0.1 V vs. Li/Li^+), making it suitable for significantly enhancing the energy density of a Li-ion cell. Furthermore, silicon has many other advantages, including low cost, environmental friendliness and is one

of the most abundant materials in the earth's crust, motivating significant attention over recent decades. However, the significant volume change (~300% - 400%) during battery charge/discharge and the formation of an unstable solid electrolyte interface (SEI) hinder its large-scale commercialization.[15] In industry, people mainly address these issues by introducing carbon-based materials with small volume change and high conductivity to stabilize silicon.[16, 17] Presently the commercialization of Si/C anodes have achieved periodic victory, the battery used (made by Panasonic) in Tesla`s Model 3 electric vehicles starts with an anode made up of 10% silicon, providing 30% boost in energy density.[18] In this thesis, the main goal is to design a stable carbon-based scaffold to accommodate the large volume expansion that occurs in high silicon content anodes, enabling the utilization of more silicon and resulting in further improvements to energy density.

1.2 Thesis Outline

Table 1.1 The flow chart of thesis overview

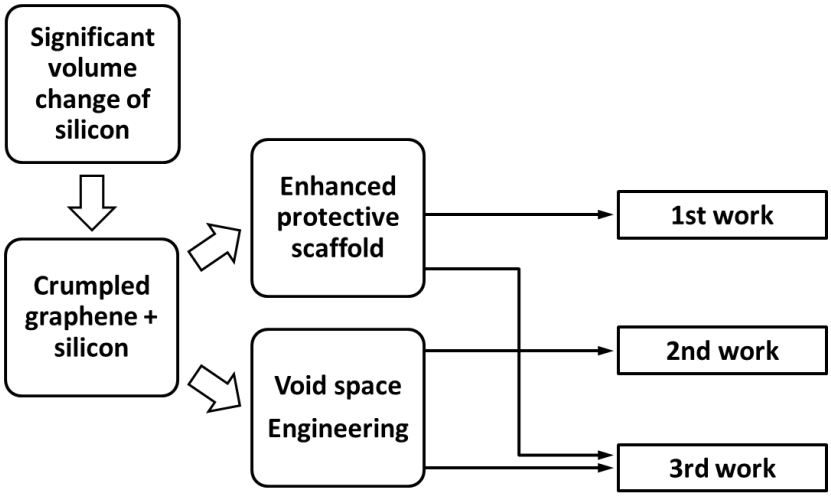

This thesis aims to design a graphene-based scaffold capable of buffering the volume change of a high loading, high silicon content anode (> 35wt%) while maintaining an efficient

electric and ionic transport pathway capable of achieving high cyclic stability and sustaining fast charging rates. This goal is achieved in three sequential works that build upon each other as shown in **Table 1.1**, which are briefly introduced below. **In the first work**, a comprehensive understanding was constructed about how to produce the optimized crumpled graphene to encapsulated silicon nanoparticles with optimal electrochemical performance by a mini spray dryer. Then, a layer of polydopamine, which can be carbonized to amorphous N-doped carbon, was polymerized at the surface of graphene shell to further seal the graphene and enhance its structural stability. **In the second work**, polystyrene nanoparticles were synthesized and mixed with silicon nanoparticles as the sacrificial template. Polystyrene is easily removed by heating, leaving well-distributed void space separating the silicon core from the graphene shell. Upon the controllable engineering of void space volume, the resulting voided composite provided enhanced battery performance, especially the rate performance and high-loading cycle life. **In the last work**, a novel method is designed to spontaneously create void space between silicon and graphene by swelling of a hydrogen binder encapsulated in the core. The resulting polymer also acts as ionic conductive binder to further ehance the stability of crumpled structure. The resulting composite exhibited a significantly improved cycle life as well as rate capability.

The thesis is organized into six chapters: **Chapter 1** provides a general background about the motivation of this thesis. **Chapter 2** briefly introduces the operation mechanism and advantages of lithium-ion batteries, and also provide an overview in the field of anode materials, especially fousing on challenges and recent strategies to overcome the challenges of silicon based anode materials. General theory about spray drying, the main process used

to make crumpled graphene is also introduced in this chapter. **Chapter 3**, **Chapter 4** and **Chapter 5** present the three main works of my thesis, which are described in the first paragraph, in terms of experimental details, results, discussion and conclusion. Finally, **Chapter 6** summarizes the various contributions and discusses suggested future work in this area.

2 Literature Review

2.1 Lithium-ion Batteries

Lithium-ion batteries, also known as lithium-ion secondary (i.e., rechargeable) batteries, are one of the most common energy storage systems commercialized so far. After the electrochemical intercalation of lithium ions into graphite was demonstrated by Samar Basu at the University of Pennsylvania in 1977, which provided an alternative to lithium metallic electrode batteries, lithium-ion batteries have achieved rapid development and occupied 66% of all portable secondary battery sales in Japan in 2011.[16] In 2019, the Nobel Prize in Chemistry was awarded to John Goodenough, Stanley Whittingham and Akira Yoshino due to their outstanding contributions in the development of lithium-ion batteries.[17]

A lithium-ion battery typically consists of a cathode, an anode, a separator, two current collectors and the electrolyte as shown in **Figure 2.1**. Common cathode materials are lithium intercalation compounds formed with transition metal oxides, such as $LiCoO_2$,[18] $LiNiO_2$,[19] $LiMn_2O_4$,[20] etc. Commercialized anodes are usually made of carbon,[21] including graphitized carbon materials and amorphous carbon materials such as soft carbon and hard carbon. Since the electrochemical alloying of lithium metal with other metals including Sn, Pb, Al, Au, Pt, Zn, Ag, Mg, and Cd was demonstrated by Dey et al.,[22] and some metallic or semi-metallic elements, such as Sn,[23] Ge,[24] Sb,[25] and Si[13, 14] alloy-based anodes have attracted significant attention during the past few decades. The function of the separator is to isolate the positive

and negative electrodes and prevent the internal short circuit of the battery. This is typically a layer of microporous polymer membrane that only allows ions to pass through freely and

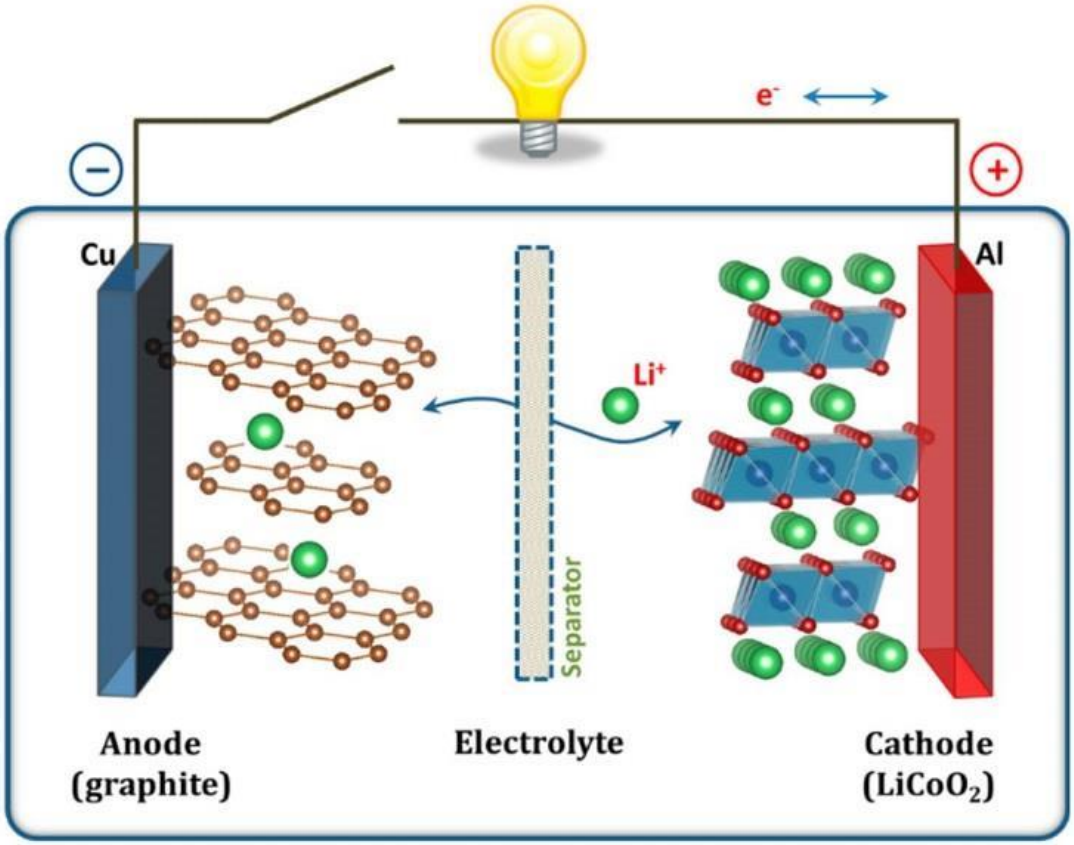

Figure 2.1 A typical commercial lithium-ion battery schematic (adapted from ref. 32)

thus prevent electrical shorting of the anode and cathode.[26] The current commercially used separators are made of microporous, multi-layer composites of polyethylene (PE) and polypropylene (PP).[27] The electrolyte for the lithium-ion battery is usually a polar organic solvent in which a lithium salt ($LiPF_6$, $LiAsF_6$, $LiBF_4$, $LiClO_4$, etc.)[28] is dissolved. The most commonly used organic solvents are ethylene carbonate (EC), dimethyl carbonate (DMC), ethyl-methyl carbonate (EMC), propylene carbonate (PC) and diethyl carbonate (DEC) and so on chosen for their electrochemical stability and moderate dielectric constant enabling the dissolution of high concentrations of lithium salts.[29] The form factor of commercial

lithium-ion batteries can be mainly divided into coin cell, cylindrical cell, prismatic cell and pouch cell, which often include many layers of anode/separator/cathode in order to minimize the relative mass/volume of inactive casing or packaging.[30]

Lithium-ion batteries store energy by converting electrical energy to chemical energy through the transfer of lithium ions, whose operation mechanism is briefly introduced here.[31] A typical lithium-ion battery[32] with a positive electrode material of $LiCoO_2$ and a negative electrode material of graphite is taken as an example, and its internal structure and working principle are shown as in the **Figure 2.1**. The reactions that occur during charging and discharging are written as follows:

Positive electrode: $$\mathrm{LiCoO_2} \leftrightarrow \mathrm{Li_{1-x}CoO_2} + \mathrm{xLi^+} + \mathrm{xe^-} \quad (1.1)$$

Negative electrode: $$\mathrm{6C} + \mathrm{xLi^+} + \mathrm{xe^-} \leftrightarrow \mathrm{Li_xC_6} \quad (1.2)$$

Overall Reaction: $$\mathrm{LiCoO_2} + \mathrm{6C} \leftrightarrow \mathrm{Li_{1-x}CoO_2} + \mathrm{Li_xC_6} \quad (1.3)$$

Li^+ ions are extracted at the positive electrode from the unit cell of $LiCoO_2$ during the battery charging process by an external power supply. At the same time, the Co^{3+} in $LiCoO_2$ is oxidized to Co^{4+} and releases electrons to the external circuit. At the negative electrode, the charge is balanced by lithium intercalating into the graphite layers, which combined with electrons from the external circuit. In the discharge process, the equilibrium potential of the positive electrode (now the cathode) is higher than that of the negative electrode (now the anode) and is capable of a spontaneous, galvanic reaction in which the reactions are shown above reverse in direction and can be used to discharge power through a load. In the fully lithiated state (LiC_6), Li^+ ions de-intercalate and electron are released to the external circuit.

Li^+ ions then re-insert into the $LiCoO_2$ cathode via the electrolyte, Co^{4+} ions are reduced to Co^{3+} ions while the cathode obtains electrons from the external circuit.

Except for lithium-ion batteries, there are four other main commercialized rechargeable batteries, including lead-acid, Ni-Cd and Ni-MH batteries. Key characteristics based on average ratings for these four types of batteries are summarized in **Table 2.1**. Although the lithium-ion battery is a relatively young technology, it is superior in nearly all aspects, especially in gravimetric and volumetric energy density. However, compared to other secondary batteries, lithium-ion batteries are still suffering from some disadvantages, such as high cost and low safety. In addition, current commercial lithium-ion batteries cannot meet the rapidly increasing demand for energy density in varying fields, such as electric vehicles and portable electronics. Hence, further study and improvement are required for all components in lithium-ion batteries. Considering that this thesis focuses on the design of Si/rGO based anodes, we will briefly introduce some of the other most promising anode materials being considered in the next section.

Table 2.1 Main characteristics of varying secondary batteries (adapted from ref. 8)

Characteristics	Lead-acid battery	Ni-Cd battery	Ni-MH battery	Li-ion battery
Gravimetric energy density (Wh kg^{-1})	30-50	40-60	60-120	170-250
Volumetric energy density (Wh L^{-1})	60-110	150-190	140-300	350-700
Battery voltage (V)	2.0	1.2	1.2	3.7
Cycle life (to 80% of the initial capacity)	300	1500	1000	500-2000
Self-discharge per month (%)	5	20	30	<10
Fast charging time (h)	8-16	1	1-4	1 or less
In use since	Late 1800s	1950	1990	1991
Toxicity	High	High	Low	Low
Overcharge tolerance	High	Moderate	Low	Low
Operating temperature range (°C)	−20 to 60	−40 to 60	−20 to 60	−20 to 60

2.1.1 Anode Materials

To develop next-generation lithium-ion batteries with enhanced safety, high energy density, long cycle life and low cost, the ideal anode materials for lithium-ion batteries should have the following properties: 1) high theoretical gravimetric and volumetric capacities, 2) low and stable operating voltage (vs Li/Li^+, which decides the working voltage of the full cell), 3) being insoluble in the selected electrolyte, 4) good structural stability during lithiation and delithiation, 5) high electric and ionic conductivities, 5) abundant, low-cost and eco friendly.

Anode materials for lithium-ion batteries can be classified into three types according to their lithiation mechanisms:[10] 1) Intercalation/deintercalation - This mechanism typically requires a material with a two-dimensional layered structure (e.g., graphite, $Li_4Ti_5O_{12}$ and TiO_2)[33-36] or 1D channels (e.g., CNT)[37, 38], which are capable of intercalating lithium-ions without irreversibly destroying the host lattice; 2) conversion reactions – transition metal oxides (e.g., NiO,[39] Co_3O_4,[40] Fe_2O_3[41] and MnO_2[42]etc.) usually store lithium ions via this reaction, that metal oxides are converted to their pure metallic state along with Li_2O during lithiation and then reversibly return to their initial oxide state after delithiation; 3) alloying/dealloying – some elements (mainly from Group IV and Group V), such as silicon (Si),[13] germanium (Ge),[24] tin (Sn)[23] and zinc (Zn)[43] can alloy with multiple lithium ions (per atom). Thus, these materials usually possess very high capacity, which have tremendous potential for next-generation lithium-ion batteries requiring high energy density. Next, some main commercial anode materials are briefly introduced below.

For the past two decades, graphite has been the most important anode material in the field of rechargeable lithium-ion batteries, and still accounts for most of the anode market.[44] Compared with other anode materials, it has many advantages, including low cost, abundant raw material source, low working potential, excellent electric conductivity, high lithium-ion diffusivity and a relatively small volume change (~10%) during lithiation/delithiation. The small volume change is the key to its success as this has enabled a relatively stable solid-electrolyte interface (SEI) to form at the low potentials experienced at high levels of lithiation. This stable passivation layer prevents the electrolyte from continuously decomposing during cycling.

Another important anode is lithium titanate[45, 46] ($Li_4Ti_5O_{12}$, LTO), which is converted from a face-centered cubic spinel structure into $Li_7Ti_5O_{12}$ with a rock-salt structure after lithiation. LTO has become a successful commercial anode due to its excellent thermal stability, cycle life (> 6000 cycles), first charge Coulomb efficiency (> 98.8%), rate capability, low temperature performance and high volume specific capacity.[47] The volume change of LTO is very small (only ~0.2%) upon intercalation of lithium ions, hence, it is often referred to as a "zero strain" material.[48, 49] Furthermore, its high equilibrium potential (1.55V vs. Li/Li^+) is above the decomposition potential of most electrolytes and thus LTO anodes avoid the formation of SEI altogether and the risk of lithium platiing and dendrite formation is effectively eliminated. This reduces irreversible capacity loss and improves safety. However, LTO still has many shortcomings such as low overall cell voltage (due to its high equilibrium potential), low theoretical capacity (175 mAh/g) and high production cost. At present, it has

certain application prospects in the field of high-power lithium-ion batteries through modification by nanostructuring and carbon coating.

The theoretical specific capacity and corresponding potential vs Li/Li^+ are plotted in **Figure 2.2**, illustrating that silicon has ideal properties (which are close to lithium metal) to archieve the goal of designing next-generation lithium-ion batteries with high energy density. Although lithium metal is still the most ideal anode material, low coulombic efficiency and severe lithium dendrite growth have largely limit its pratical applications. Similarly, silicon also suffers from various related challenges, which will be further discussed in section 2.2.

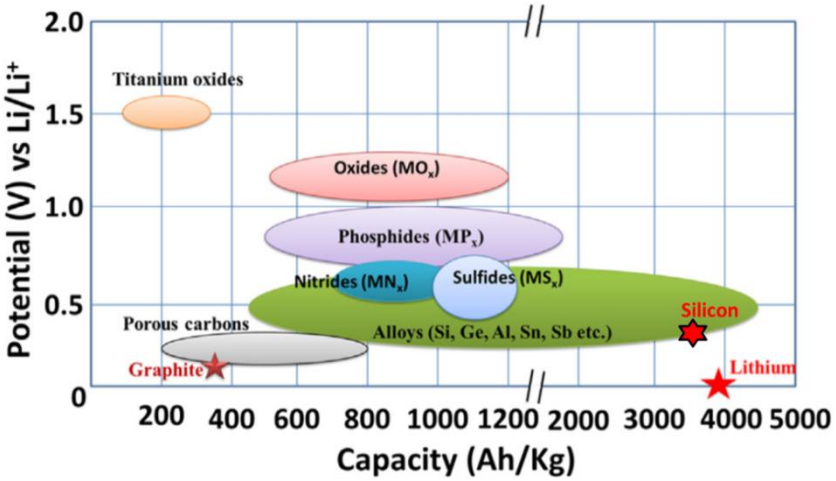

Figure 2.2 Schematic of anode materials for next-generation lithium-ion batteries and their corresponding specific capacity vs. Li/Li^+.(adapted from ref.50)

2.1.2 Batteries Metrics

This section will introduce some important metrics which indicate the performance of a rechargeable battery. The first important metric is the theoretical gravimetric capacity (*Q*) of each electrode, which is related to the specific half-cell reaction according to Faraday's law:

$$Q = \frac{nF}{3.6M}, \tag{2-1}$$

where *n* is the number of electrons transferred, the factor of 3.6 is used to convert the units from C/g to mAh/g and *M* is the molecular weight of electrode material. The theoretical total capacity Q_{total} of a full cell composed of an anode and a cathode can be calculated by capacity matching as:

$$\frac{1}{Q_{total}} = \frac{1}{Q_{cathode}} + \frac{1}{Q_{anode}} \tag{2-2}$$

where the units of Q_{total} are in mAh per gram of total active material. It does not include the masss of any inactive materials such as separator, electrolyte, membrane, packaging, etc.

Another significant parameter, the cell voltage (U_{cell}), is the thermodynamic driving force, which is dictated by the difference in equilibrium potential between the cathode ($U_{cathode}$) and anode (U_{anode}):

$$U_{\text{cell}} = U_{cathode} - U_{anode}\ , \tag{2-3}$$

These reduction potentials are related to both the standard reduction potential of the electrode, as well as the activities of the oxidized and reduced species through the Nernst equation:

$$U = U^0 + \frac{RT}{nF} \ln \frac{a_O^{\nu_O}}{a_R^{\nu_R}}, \tag{2-4}$$

where *U* is the reduction potential of the electrode, U^0 is the standard reduction potential of the electrode, *R* is the gas constant, *T* the working temperature, *n* is the number of electrons

transferred in the half-cell reaction, F is Faraday's constant, a_R and a_O are the activities of reduced species and oxidized species in the half-cell reaction respectively, v_R and v_O are their stoichiometric coefficients.

Another important metric of full cells is the energy density of the cell, which is decided by both cell voltage and total cell capacity. Assuming a constant potential, the theoretical gravimetric energy density, reported in Wh/kg is:

$$E = U_{\text{cell}} Q_{total} \tag{2-5}$$

Upon different requirements in practice, the theoretical gravimetric energy density can be converted into areal energy density or volumetric energy density by multiplying areal density, ρ_A or volumetric density, ρ_v.

However, a real battery does not only consist of two electrodes but also includes separators, electrolyte, current collectors and packaging. Hence a correction factor, F, has to be considered to calculate cell`s total gravimetric energy density:

$$E_{\text{real}} = F U_{cell} Q_{total} \tag{2-6}$$

$$F = \frac{m_{active}}{m_{total}}, \tag{2-7}$$

where m_{active} is the weight of active materials, including cathode and anode materials, and m_{total} is the weight of a single battery cell. For commercial cells, F ~ 30wt% is enabled by using thick or high loadings (in mg/cm^2) of active material to increase their fraction compared to other battery components.

2.2 Silicon Anode

Silicon is the second most abundant element (~28wt%) in the earth's crust, which only follows oxygen.[51] Thanks to decades of explorations and accumulations in the semiconductor industry, the source of elemental silicon is very rich, and the preparation and purification processes are quite mature. As an anode material for lithium-ion batteries, silicon is alloying/dealloying during the charge/discharge process to achieve energy storage and release of lithium ions. At around 450°C, silicon can form a variety of alloy phases with lithium ions, including $Li_{22}Si_5$, $Li_{13}Si_4$, $Li_{14}Si_6$ and $Li_{12}Si_7$.[52] The corresponding theoretical capacity with the fully lithiation states ($Li_{22}Si_5$) reaches 4200 mAh/g, which is around 11.3 times larger than that of the graphite anode (372 mAh/g) for commercial lithium-ion batteries. Such a remarkable value makes silicon one of the most promising candidates for next-generation lithium-ion batteries, and related research has become a hot topic in the scientific community.

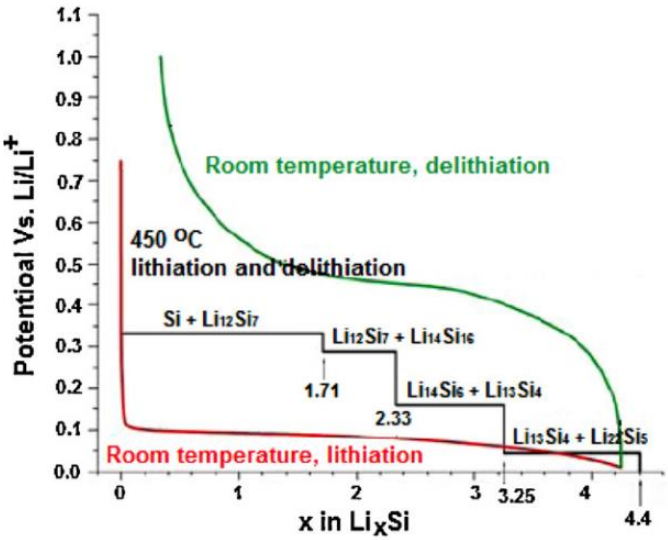

Figure 2.3 Si charge/discharge curves including the theoreticl voltage curve (black) at 450 ℃, lithiation curve (red) and delithiation curve (green) of crystalline Si at room temperature. (adapted from ref. 53)

Figure 2.3 shows the ideal charge (delithiation process, green curve) and discharge (ltihiation process, red curve) curves of the silicon anode during the first cycle.[53] According to the equilibrium phase diagram, silicon undergoes a series of different alloy phase transitions when it reacts with lithium. Theoretically, this reaction happens at gradually decreasing voltage plateaus (as the black voltage curve in **Figure 2.3**) with the increasing degree of lithiation, and finally reaches its fully lithiated state ($Li_{22}Si_5$). However, this process with multiple reactions only takes place at high temperature.[52] At room temperature, only a long discharge plateau appears in the range of 0.1V - 0.05V (as shown by the red line in **Figure 2.3**) in most silicon anode discharge curves. Via in-situ XRD, Obrovca et al.[54] demonstrated that the full lithiation state of silicon during discharge is $Li_{15}Si_4$ instead of $Li_{22}Si_5$ at room temperature, which corresponds to a theoretical specific capacity of about 3590mAh/g. Li et al.[55] further confirmed the structural change of silicon in the initial charge and discharge. Crystalline silicon first reacts with lithium ions to form an amorphous Li_ySi (y=~3.5) alloy during the first discharge, which exhibits a long voltage plateau at about 0.1 V. When the voltage decreased to around 0.05 V, amorphous Li_xSi (0 <x<3.5) rapidly changed to a metastable crystalline structure of $Li_{15}Si_4$ to reach the full lithiation state. Upon delithiation, the voltage plateau is stabilized at about 0.3-0.4V, and the crystalline $Li_{15}Si_4$ is re-decomposed into amorphous Li_zSi (z=1-2) and finally delithiated to amorphous silicon. Given that two-phase coexistence regions can result in capacity fading due to inhomogeneous volume change, they suggested that the working voltage can be limited to be greater than 0.05V to eliminate crystal phase generation, which can make silicon always stay in an amorphous state after the first discharge.[55, 56] Due to the alloying process, silicon

undergoes a severe volume change and inner stress, we will introduce these main challenges in the next section.

2.2.1 Main Challenges

This section will briefly introduce the most serious issues that hinder the large-scale commercialization of silicon anodes:[13, 14] 1) large volume change during alloying/dealloying and transitions between crystalline and amorphous states, which generate large internal stress leading to rapid self-pulverization during initial cycling, and 2) formation of unstable SEI due to the volume change.

Material Pulverization

Electrochemical lithiation of silicon at room temperature is consistent with a two-phase reaction mechanism.[54, 55] During lithiation, crystalline silicon is gradually converted into amorphous lithiated silicon (Li_xSi), there is an obvious voltage platform at around 0.1 V in its constant current discharge curve. When the voltage drops below 0.05 V, Li_xSi will crystallize and form metastable $Li_{15}Si_4$. In this lithiation process, the silicon material undergoes a severe volume expansion (~300%-400%). And the lithiation reaction rate for crystalline silicon (c-Si) at the interface between the c-Si core and the amorphous Li_xSi is different upon lattice faces, resulting in an anisotropic volume expansion.[57] Since the growth rate at the <110> is the fastest, the volume expansion in the <110> direction is also the most severe.[58, 59] For amorphous silicon, the volume expansion during lithiation is isotropic. However, whether it is crystalline silicon or amorphous silicon, the volume expansion is over 300% after complete lithiation, which generates large stress inside the material.[60] Chon et al.[61] demonstrated that

during initial lithiation, a moving phase boundary advances into the Si wafer starting from the surface facing the lithium electrode, transforming crystalline silicon into amorphous Li_xSi. The resulting biaxial compressive stress in the amorphous layer is measured in situ and it was determined to be around 0.5GPa. By carrying out high resolution TEM, they also revealed that the crystalline/amorphous phase boundary is very sharp, with a thickness of ~1nm. During delithiation, the stress rapidly reverses, becomes tensile and the amorphous layer begins to deform plastically at around 0.5GPa. The tensile stress rapidly increased with further delithiation, leading to sudden cracking originating from the surface of the silicon water.

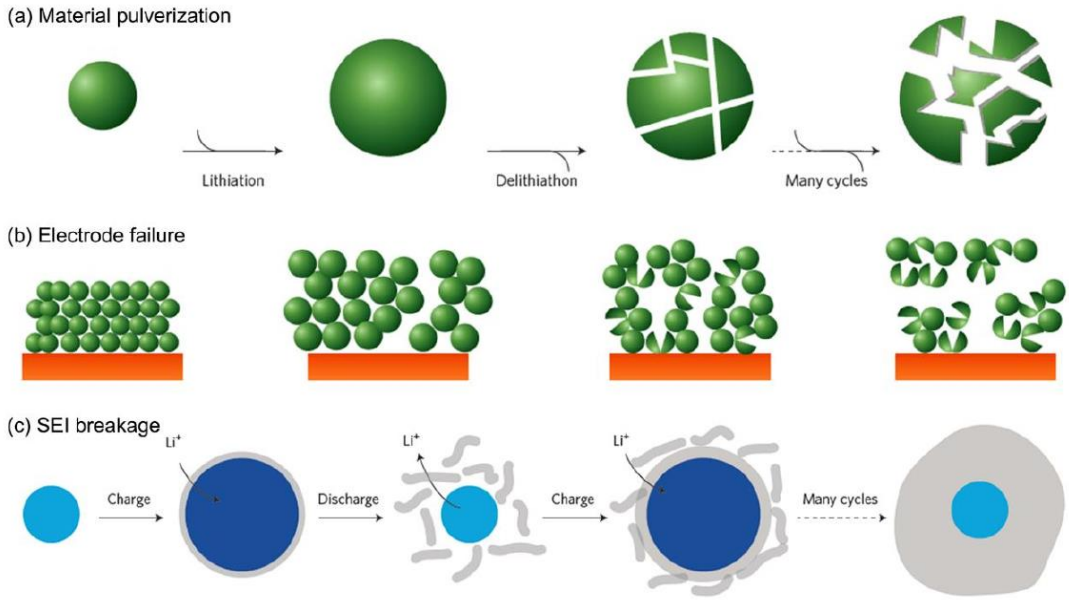

Figure 2.4 Schematic of three main failure mechanisms for pure Si anodes, including the mechanical degradation at (a) particle level and (b) electrode level, (c) electrode failure due to the formation of unstable SEI (adapted from ref.62)

Repeating lithiation/delithiation of silicon particles is required during battery cycling, hence the resulting volume expansion and shrinkage may further affect the overall structural stability of silicon-based electrodes. During lithiation, silicon particles expands and impinge

on their neighbours (including binder, conductive additive and other Si particles), while the volume shrinkage during delithiation may cause the detachment of silicon from the conductive network. This drastic structural change leads to the potential cracking of the electrode and even may cause the anode material to fall off from the current collector and lose electrical contact as shown in **Figure 2.4**, which seriously affects its cyclic stability and rate capability. However, Liu et al.[63] discovered that the self-pulverization of silicon particles at very initial cycles can be effectively slowed down by limiting its size below a critical value (~150 nm) as shown in **Figure 2.5**. According to Griffith`s theory,[64] the propagation of a crack only happens when the pre-existing crack length is long enough or the applied stress is strong enough to overcome the increase in surface energy created by exposing the fresh interface. When the diameter of Si NPs is less than 150 nm, the stored strain energy inside the nanopaticlrs during lithiation/delithiation is not enough to drive crack propagation. This suggests that the nanostructuring of silicon is very important for its application in lithium-ion batteries.

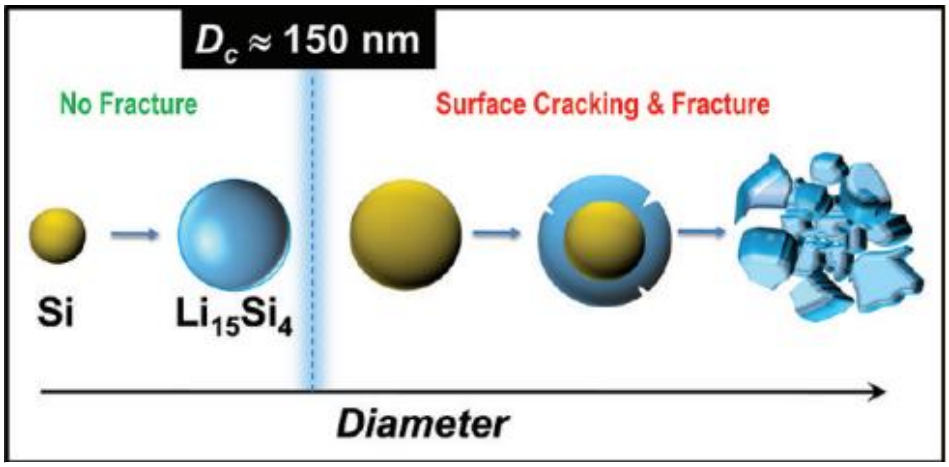

Figure 2.5 The schematic illustration of critical size for Si self pulverization, Si nanoparticles can be lithitated without cracking when the diameter is below 150 nm. (adapted from ref. 63)

Unstable Solid-State Electrolyte Surface

When the potential of anode is below about 1 V (vs. Li/Li^+), the electrolyte decomposes on the electrode surface and forms a SEI layer.[65, 66] The dense and stable SEI can effectively prevent further decomposition of the electrolyte and other side reactions. However, the SEI formed on the surface of the silicon material is destroyed by the expansion and contraction of silicon during the lithiation/delithiation process as shown in **Figure 2.4(c)**. In the subsequent lithiation process, the SEI is reformed on the surface of the newly exposed silicon material. On the one hand, the repeated formation of SEI continues to consume electrolyte and lithium ions, reducing the coulombic efficiency and cycle life. On the other hand, the thickening of SEI will hinder the charge transport and lithium-ion diffusion, reducing the rate performance and causing the deterioration of the cycle performance of the electrode. Although the addition of electrolyte additives (such as fluoroethylene carbonate (FEC) and vinylene carbonate (VC)) can significantly enhance the stability of SEI at the surface of silicon, other performance is sacrificed for improved cyclic stability.[67] For example, the addition of VC increased the thickness of SEI, resulting in increased impedance of the cell. Moreover, silicon has a lower conductivity (~10^{-3} S/cm, 10^2 S/cm after lithiation) and a lower lithium-ion diffusion coefficient (10^{-14}-10^{-13} cm^2/s) compared to that of graphite.[13] This leads to poor rate performance, which also affects the application of silicon-based materials in the negative electrode of lithium-ion batteries.

In the next section, the brief recent progress will be introduced from silicon nanostructuring and Si/C based composites.

2.2.2 Recent Progress

Silicon Nanostructuring

Nanostructuring of silicon can be achieved in variosu ways, like limiting the particle size (silicon nanoparticles), engineering the shape to make at least one dimension reach the nano-level (e.g., silicon nanotubes, nanowires) or introducing nano-sized pores into a monolithic silicon structure.[53] Not only does nanostructuring effectively prevent the silicon anode from self pulverization in initial cycles, but it improves the resulting electrochemical performance and volume change tolerability because 1) the shortened distance enables faster lithium-ion diffusion and improved electron transport supporting the higher rate battery operation; 2) the smaller dimension leads to improved fracture resistance because the total elastic energy generated in a small structure may not be sufficient to initiate cracking and crack propagation; 3) the resulting larger specific surface area (SSA) increases the interfacial area between silicon and binder, conductive additives or electrolyte to release the stress. Some significant advances are briefly introduced here.

Taeseup Song et al.[68] prepared a sealed hollow silicon nanotube as the anode for lithium-ion batteries. The axial free void space in the nanotube provided the additional surface to accommodate the volume expansion and meanwhile avoided direct contact with electorlyte, making the electrode displayed high initial coulombic efficiency (>85%) and stable capacity retention (>80% after 50 cycles). It was demonstrated that the internal surface of the silicon nanotubes bears the mechanical stress, resulting in a reversible volume change along the axial direction where only a relatively small (< 35%) volume change

occurred as shown in **Figure 2.6**. Byoung et al.[69] utilized 10 μm micro-silicon powder to obtain 3D porous silicon particles by silver-induced chemical etching by HF/H_2O_2. This porous silicon was prepared as anode after carbonization, showing improved reversible specific capacity of 2050 mAh/g with an excellent coulombic efficiency of 94.4%. Ge et al.[70] proposed a low-cost and large-scale production method of porous silicon. Commercial metallurgical silicon powder was ground into micron silicon powder via ball milling, and then nanoporous silicon was obtained by stain-etching using ferric etchant to remove the high concentration of impurities in metallurgical silicon. The resulting electrode exhibited a very high SSA of 70 m^2/g with a pore volume of 0.133 cm^3/g, making this material able to maintain above 1100 mAh/g after 600 cycles at 2000 mA/g.

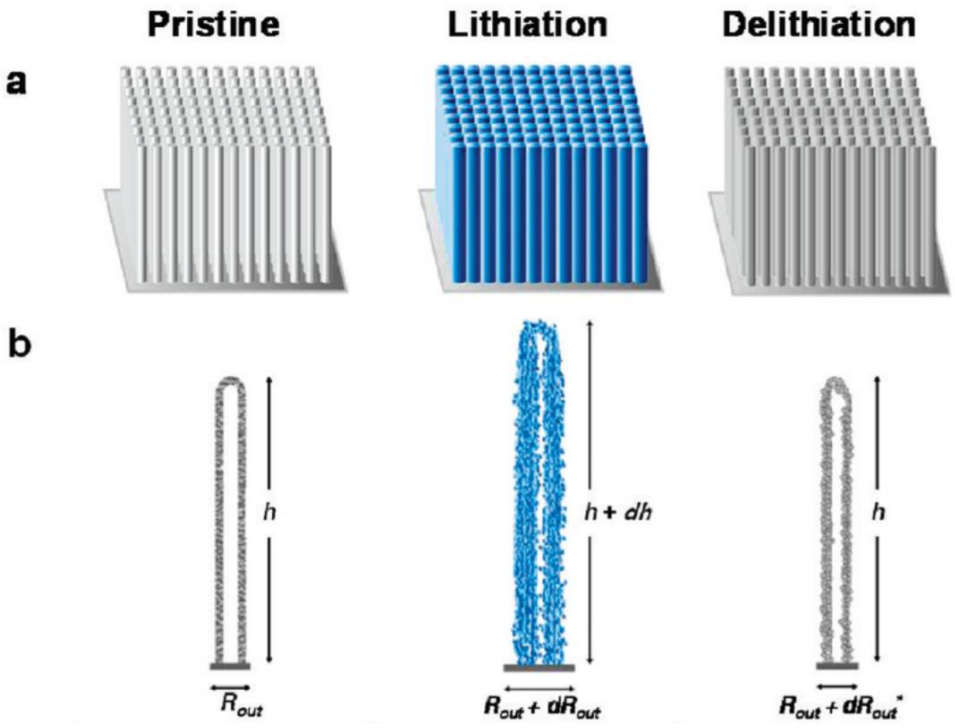

Figure 2.6 Schematic illustration of hollow silicon nanotube before reachtion and after full lithiation and delithiation (a) and corresponding volume change in different directions (b). (adapted from ref.68)

Carbon Coated Silicon Composites

In addition to the large volume change, the conductivity of silicon is also unsatisfactory as a typical semiconductor material. Compositing silicon with a second phase having excellent structural stability and electrical conductivity, such as carbon[71] and other metallic conductors[72, 73], enables the improvement in both cycle life and capacity retention at large current density.

Interfacing Si particles with conductive carbonaceous additives is one of the most common methods used to buffer the volume fluctuation of the silicon and limit or decrease the direct formation of SEI on the silicon surface.[74, 75] This has been demonstrated via several methods including mechanical mixing,[76] in situ chemical polymerization,[77] and chemical vapor deposition.[78] However, a conformal but relatively inelastic carbon coating cannot sustain a stable electrode structure from the large volume change of Si during long-term cycling as shown in **Figure 2.7**.

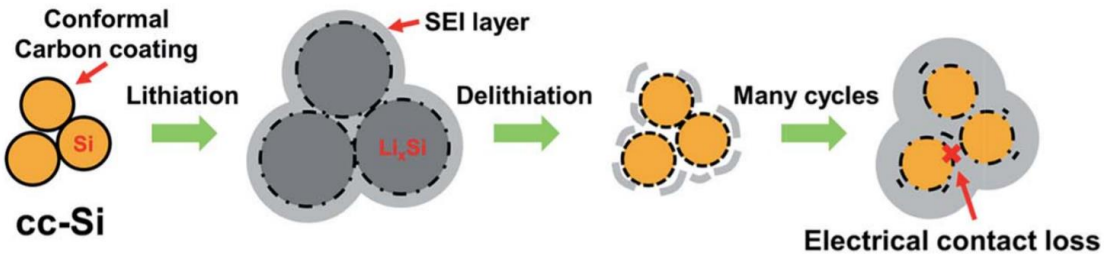

Figure 2.7 The hypothetical failure mechanism of conformal carbon carbon coated silicon without reserved void. (adapted from ref.79)

2.2.2.1 Carbon Coated Silicon Composites with Reserved Void Space

To prevent the rupture of the carbon protective layer, methods that introduce void space between silicon and carbon have been developed to accommodate the expansion/contraction of the Si. For example, Liu et al.[80] proposed a novel method to prepare carbon-coated Si nanoparticles with a yolk-shell structure as shown in **Figure 2.8**. A void space for buffering the volume change was created by removing an artificially created silicon oxide (SiO_2) layer between a carbonized polydopamine shell and silicon core via HF etching. Using this structure, the electrode material maintained a reversible capacity of ~ 1110 mAh/g (retention of 74%) after 1000 cycles. Based on a similar method, Liu et al.[44] synthesized a pomegranate-like structure of a micro-size Si/C particle using a bottom-up microemulsion method. This large pomegranate-like structure effectively increased the density of the electrode material which further increased its volume-specific capacity by enabling a higher tap density due to the larger particle size. Moreover, one pomegranate-like particle is composed of hundreds of nano-size Si/C particles, which largely decreased the SSA exposed to electrolyte resulting in improved initial coulombic efficiency. Based on the design of the yolk-shell structure, Zhang et al.[81] demonstrated a co-deposition method to obtain $CaCO_3$-Si microspheres, which were successively coated by SiO_2 and carbon. Finally, the void space was introduced by removing the $CaCO_3$ by immersing the structure in diluted hydrochloric acid (HCl) solution. This method avoids the use of HF and also improves the material density upon the introduction of ferric oxide (Fe_2O_3) nanoparticles and carbon nanotubes (CNTs). However, these methods involve more complex or even hazardous synthesis techniques (e.g., HF-etching) that also add to the costs

associated with fabricating the anode. Hence, a simpler and more efficient strategy for carbon coating is desired to promote the role of silicon-based anodes in the market of commercial Li-ion batteries.

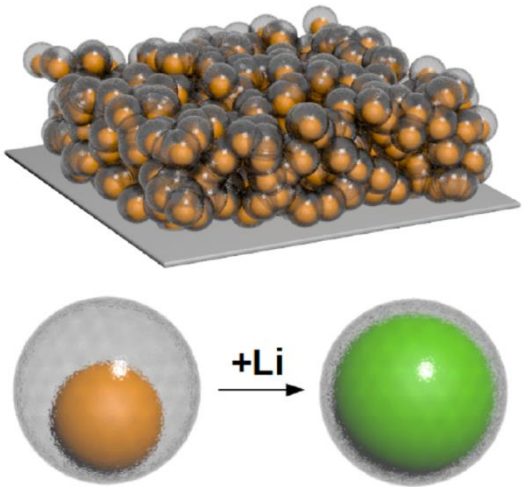

Figure 2.8 The schematic of a yolk-shell design C/Si anode with reserved buffer space between carbon shell and silicon yolk. (adapted from ref.80)

In contrast, silicon can be also be loaded into a carbon scaffold with pre-reserved voids or pores. Liu et al.[82] deposited silicon particles with a particle size of about 10 nm in the interior of porous carbon by chemical vapor deposition (CVD), taking advantage of these pores to accommodate the volume expansion of silicon particles while the carbon framework also provides good electric and ionic conducting pathways. Wang et al.[83] prepared carbon nanotube (CNTs) array by CVD method and obtained CNT/Si composites after depositing silicon particles on their surface. Taking advantage of the free space between aligned pristine carbon nanotubes, the volume change of silicon is effectively accommodated, leading to a tiny decay in the capacity of ~0.15% per cycle over the first 25 cycles. Due to the high mobility of lithium ions and electrons in CNTs, the rate capability was also be significantly improved. Wu et al.[84] creatively encapsulated silicon nanoparticles

inside the carbon nanotubes through electrospinning upon the hollow structure of CNTs and its large aspect ratio. This design effectively insulated the direct contact between silicon and electrolyte, making the composite exhibited a 90% capacity retention rate after 200 cycles in the charge and discharge test.

Although these novel designs by using chemical etching, CVD or other methods have achieved significantly impressive progress, this thesis aims to find a more scalable method to produce Si/C based anodes with improved electrochemical performance. In the next section, I will briefly introduce the preparation, properties and relevant applications of crumpled graphene, which is a very promising protective scaffold to buffer the volume change of silicon.

2.3 Crumpled Graphene Shells Produced by Spray Drying

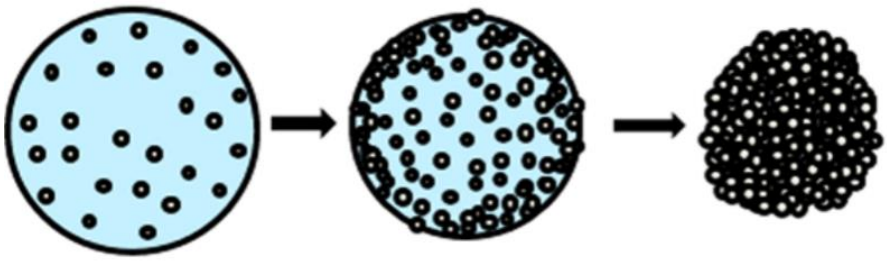

Figure 2.9 Schematic illustrating the drying of microdroplet containing dispersed nanoparticles (adapted from ref.85)

The spray drying technique has been widely applied in the fields of food, medicine and energy storage, which can easily transfer materials from dispersion to dry powder with tailored structure and components distribution. The process can be simply described as below, which mainly includes three steps: 1) formation of microdroplets; 2) solvent

evaporation and segregation of dispersed components inside the microdroplet; 3) capillary collapse. The features of the precursor suspension (e.g., initial particle size, type of material, physical and chemical properties, and surface charge) and process conditions (e.g., temperature, atomization pressure) play an important role in producing products with various morphologies (such as spherical structures, hollow spherical structures and donut-like structures).[85-87] Here, we only briefly discuss the formation of spherical products. As shown in **Figure 2.9**, after the formation of microdroplets via the spray nozzle, the solvent starts to evaporate at the air/liquid interface. As the droplet shrinks, more and more dispersed particles accumulate at the vicinity of air/liquid interface, resulting in a concentration gradient form surface to core. Hence, the dispersed particles spontaneously move to the core driven by diffusion. The dimensionless number known as the Peclet number (Pe) defined as $(R^2/t_{dry})/D$ describes the ratio of convective transport to diffusive transport and can be used to compare the time-scales associated with products at the moving interface (i.e., convective transport) vs. redistribution into the core (i.e., diffusive transport).[88, 89] Here, R is the radius of the droplets, D is the diffusivity of the dispersed component, and t_{dry} is the drying time. When Pe is small, convection does not play a significant role and particles can diffuse within the droplet which causes a relatively homogeneous radial distribution of primary particles within the final dried micro-particle. In contrast, a hollow structure forms when diffusion is relatively very slow. Similarly, the Pe number of different dispersed components can decide their radial distributions since materials with large diffusivity prefer to maintain their concentration balance in the

microdroplet while materials with low diffusivity are controlled by convective process and accumulate at the surface of the dried micro-particle.

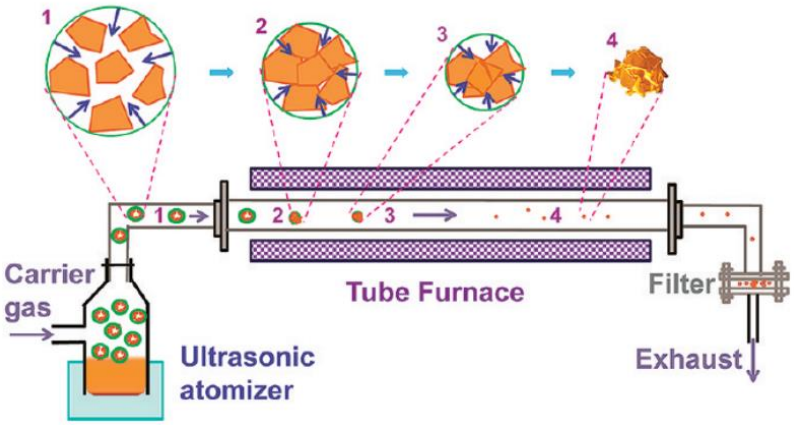

Figure 2.10 Schematic of ultrasonic atomization drying and formation mechanics of graphene crumpled balls (adapted from ref.90)

Graphene is a well-known 2D nanomaterial that is composed of a monolayer of sp^2 hybridized carbon atoms arranged in a hexagonal lattice.[91] In this thesis, the work "graphene" is used in particular to refer to reduced graphene oxide (rGO) rather than pristine graphene, whose precursor (graphene oxide (GO)) has plenty of oxygen-containing functional groups providing sites for further modifications. Its sub-nanometer thickness makes it flexible enough to be converted to a 3D crumpled graphene[92, 93] by spray drying. In 2011, Huang et al.[90] were the first to demonstrate crumpled graphene oxide ball by a home-made spray drying system, which mainly includes an ultrasonic atomizer and a tube furnace. Considering that the tube furnace can provide a very high temperature to driven varying thermal reactions, it is better to be termed as spray pyrolysis rather than spray drying. As shown in **Figure 2.10**, the crumpled graphene balls were collected in hundreds of nanometers after graphene sheets containing microdroplets, which were produced by ultrasonic atomization, passed through a tube furnace. In this process, GO sheets were reduced and meanwhile

compressed at the same time in the furnace. They found this crumpled structure is stabilized by the plastically deformed graphene wrinkles due to strong π-π interaction, displaying several special properties: 1) the resulting folded paper ball structure has excellent aggregation resistance, which can still maintain 45% of original SSA even under compression at 55 MPa; 2) the crumpled balls have a high specific surface area (567 m^2/g by thermal shock) and rich electric/ionic conducting channels, leading to excellent performance for use in fuel cells and supercapacitors.

In recent years, more researchers have realized the promise of the large-scale spray drying technique by using widely available and relatively inexpensive commercial spray dryers.[94, 95] Although their drying temperature (outlet temperature: < 100°C, which is controlled by inlet temperature in the range of 100°C - 220°C) is much lower than spray pyrolysis methods which use tube furnace, the mild processing temperature is more appropriate for processing thermally sensitive materials. Meanwhile, the low-temperature drying process can effectively limit the SSA of rGO, resulting in decreased electrolyte consumption by SEI formation. Ruoff's group[96] adopted the spray drying method to prepare the crumpled GO microspheres, followed by microwave reduction and potassium hydroxide activation, exhibiting a high capacity of 172 F/g at 2 A/g which only dropped by ~6% after 1000 cycles. Zhou et al.[97] introduced nano iron trioxide (Fe_20_3) into the GO dispersion, and then used a commercial spray dryer to prepare crumpled Fe_20_3@GO microspheres. The low drying temperature slowed the reaction between Fe_20_3 and carbon to ensure all of the Fe_20 was successfully preserved and could be used as an anode material. This composite displayed a capacity of 800 mAh/g with excellent cyclic stability (retaining ~83% of initial

capacity after 200 cycles at 1 A/g) and small volume change, which was significantly better than that of pure iron trioxide and graphene. The enhancement was attributed to the increase of the overall conductivity by the coating of crumpled rGO and the reserved elastic space for the volume expansion of the iron trioxide, reducing the aggregation of nanoparticles, which can stabilize the structure in the multiple charging and discharge cycles.

Crumpled graphene, which has enhanced mechanical strength and controllable inner space, is also a strong carbon scaffold used to tolerate the large volume change of Si anode. Huang and his co-operators[98] firstly trapped silicon nanoparticles into crumpled graphene balls, this composite retained 83% of the charge capacity after 250 cycles at 1A/g with relative low mass loading (0.2 mg/cm^2). As shown in **Figure 2.11**, Lin et al.[99] prepared pomegranate-like Si/GO composite vial spray dring and doped N via hydrazine reduction so as to promote Li storage ability. The resulting reversible specific capacity at 100 mA/g remained as large as 1141.6 mAh/g after 150 cycles, with a high capacity retention of 96.1% from the 2nd to 150th cycle. However, only ~300 mAh/g was displayed at 5000 mA/g due to the poor conductive network. Recently, Chen et al.[100] designed a double-coated silicon-based composite, carbon coated Si nanoparticles (50-80 nm) were uniformly wrapped in crumpled graphene using a novel radio frequency induction plasma technology. The composite electrode at 0.1 A/g presented a high initial discharge/charge capacity of 2389.8 mAh/g, representing high initial coloumbic efficiency of 87.1%. However, its capacity dropped by 44.6% after 200 cycles and only 20.4% of capacity was retained when current density was increased from 0.1 A/g to 1.6 A/g.

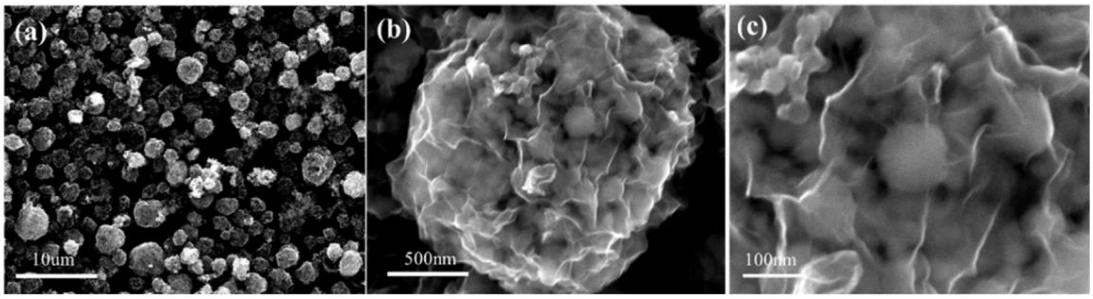

Figure 2.11 SEM images of pomegranate-like Si/rGO composite at increasing magnifications (adapted from ref. 93)

However, all above results showing the improved structure stability are mainly attributed to crumpled graphene's excellent compression-resistance. To be used as a scaffold to buffer the significant volume expansion of Si nanoparticles, the deformation-resistance of crumpled graphene from inside is more important to prevent it from unfolding. Besides, the increasing concentration of dispersed components, which are trapped in crumpled graphene balls, will affect the degree of crumpling. Chen et al.[101] spray dried GO sheets together with varying loading of silver nanoparticles. At high loading, the crumpled structure can still be observed as shown in **Figure 2.12b and c**, but with fewer creases compared to the sample prepared at low loading (**Figure 2.12a**). Hence, the optimal ratio between Si nanoparticles and graphene is required to be further studied. Furthermore, according to the current literature on Si/C anodes, the cycle life with a reasonable degradation (> 80% of capacity retention) of crumple graphene encapsulated silicon anodes[98-100] is usually much worse than that of conformal carbon coated silicon with properly reserved buffer space,[44, 80, 81] suggesting that crumpled graphene shell may require further enhancement or additional void space is essential to buffer the volume expansion to observe further improvements in electrode performance. The above discussion about

crumpled graphene supports my hypothesis that it may not have a strong enough deformation-resistance to sufficiently prevent silicon from destroying the structure via its severe volume change. Hence, the deformation-resistance of crumpled graphene and methods that enable control over the void space created within the core require further investigation and may yield further improvements to performance. Moreover, the poor rate capability results also suggest that the conductive framework of this crumpled structure requires further optimization.

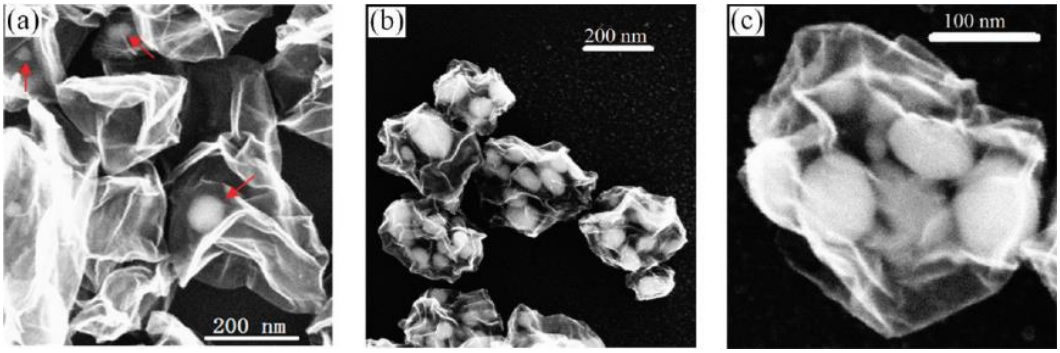

Figure 2.12 SEM images for GO/Ag with (a) low silver loading (Ag/GO: 0.06) and (b and c) high silver loading (Ag/GO: 2) (adapted from ref. 100)

3 Enhanced Cycle Stability of Crumpled Graphene Encapsulated Silicon Anodes via Polydopamine Sealing

This chapter is based on the paper published in ACS Omega:

Z. She, M. Gad, Z. Ma, Y. Li and M. A. Pope. "Enhanced Cycle Stability of Crumpled Graphene Encapsulated Silicon Anodes via Polydopamine Sealing". *ACS Omega,* 6 (18), 12293-12305, 2021.

Please see **Statement of Contributions** for details.

In this work, a controllable and efficient synthesis route to create crumpled reduced GO (crGO) encapsulated Si nanoparticles is achieved using a mini spray drying system (Figure 1). The effects of spray drying parameters on the morphology and battery performance of the resulting powders were studied by synthesizing crumpled GO/Si (cGO-Si) and crGO/Si (crGO-Si) composites with varying N_2 flow rates, feed concentrations, and GO/Si ratios. Finally, polydopamine (pDOPA) was deposited on the surface of the cGO via self-oxidization polymerization, with the goal of further enhancing the structural stability of the cGO and limiting the direct contact between the electrolyte and silicon nanoparticles. This step was followed by heat treatment to reduce the GO, where the pDOPA layer was also carbonized to create nitrogen-doped carbon (cpDOPA). This not only enhanced the structural stability of the material but also formed an electrically conductive matrix with efficient lithium-ion transport. This significantly retarded the capacity fading from 0.20%/cycle to 0.12%/cycle compared to the uncoated sample with an improved capacity of 1379 mAh/g at 1 A/g.

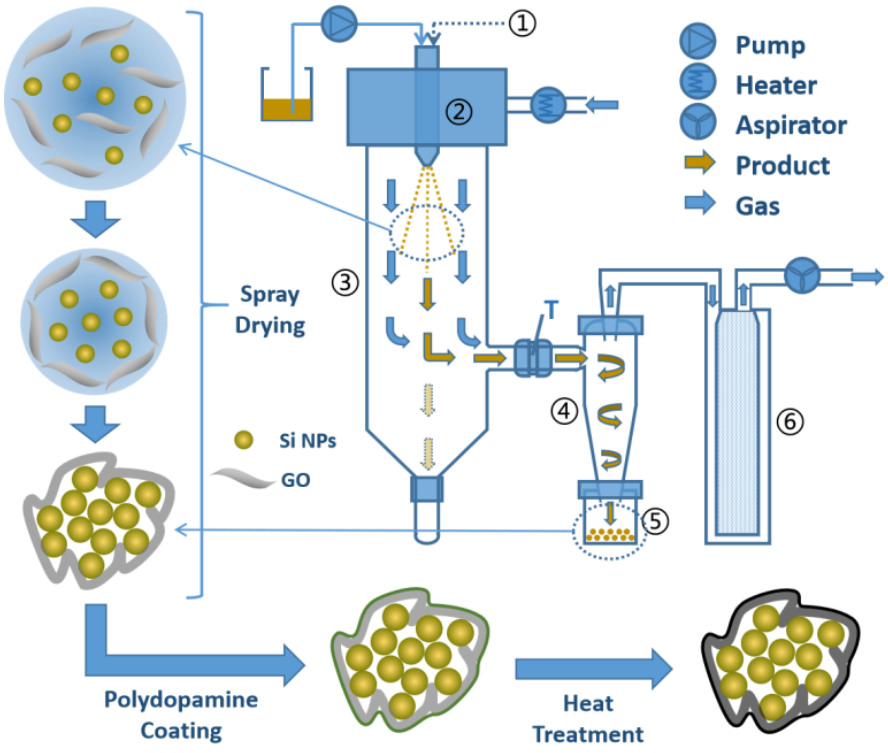

Figure 3.1 Schematic illustration of the synthesis process of cpDOPA-crGO-Si and diagram of the BUCHI-290 mini spray dryer used. (①N_2 flow in ②Spray nozzle ③Drying chamber ④Cyclone ⑤Product vessel ⑥Filter)

3.1 Experimental Methods

3.1.1 Synthesis of Graphite Oxide

GO was synthesized from natural flake graphite (Alfa Aesar) by Tour's modified Hummer's method,[102] 3 g of graphite and 18 g of $KMnO_4$ were added into a continuously stirred acid mixture composed of 360 ml of sulfuric acid (H_2SO_4) and 40 ml of phosphoric acid (H_3PO_4). The oxidation reaction was conducted at 50°C for 16 h. About 6 ml of hydrogen peroxide (H_2O_2) was added to the resulting mixture after cooling down to room temperature where the color changed from purple to golden yellow. The resultant suspension was then centrifuged for 30 min (3000 rpm, rotor diameter 15 cm). The supernatant was decanted and discarded, and the precipitant GO was dispersed in 30% HCl and centrifuged again using

the same settings. The above washing step was repeated twice using 10% HCl and four times using wash ethanol. In order to transfer GO from ethanol to deionized (DI) water, a dialysis bag with 12-14 kDa molecular weight cut off (MWCO) was used to exchange the GO dispersion's ethanol solvent with DI water. The DI water was frequently replaced with a fresh amount for 3 days and the resulting GO aqueous dispersion was stored for subsequent steps.

3.1.2 Preparation of Encapsulated Silicon

Both neat cGO and cGO-Si were produced via a BUCHI-290 mini spray dryer, as shown in Figure 1. An inlet temperature of 200°C (with an outlet temperature of ~ 80°C) and a feed pump rate of 20% of the machine's maximum (which converts to ~6 ml/min of water) were used. As a control, neat crumpled GO (i.e., not with Si) was produced at varying N_2 flow rates (246, 473 and 742 L/h) and GO concentrations (0.2, 0.5 and 1 mg/ml) to determine the ideal structure of carbon scaffold to encapsulate Si. Si nanoparticles (~50 nm, Strem Chemical Inc.) were then added into a GO aqueous dispersion based on two GO/Si mass ratios (1:0.3 and 1:0.6) and spray dried at different GO concentrations (0.5 and 1 mg/ml) at a fixed N_2 flow rate of 742 L/h. For subsequent electrochemical testing, the obtained cGO-Si was thermally reduced to crGO-Si to increase its electrical conductivity in a tube furnace (Carbolite). To maintain its crumpled structure during thermal treatment, cGO-Si was reduced at a low initial heating rate (1°C/min) under a flowing mixture of argon (95%) and hydrogen (5%) gases from room temperature to 400°C. It was held at 400°C isothermally for 2 h. It was then

heated at a faster rate (5°C/min) up to 800°C and held isothermally for 3 hours before allowing to cool down to room temperature.

3.1.3 Preparation of Carbonized Poly(dopamine) coated crGO-Si (cpDOPA-crGO-Si)

For a typical synthesis of cpDOPA-crGO-Si, 150 mg of cGO-Si were mixed with 150 mg of dopamine hydrochloride (DOPA·HCl) in 75 ml Tris-HCl buffer (10 mM, pH = 8.5) and stirred for 24 hours. This suspension was then divided into two 50 ml centrifuge tubes and centrifuged for 15 min (3000 rpm, rotor diameter 15 cm). The supernatant was discarded, and the precipitated pDOPA-cGO-Si was dispersed in DI water and centrifuged thrice again. The dried pDOPA-cGO-Si powder was collected using a LABCONCO freeze dryer. In order to carbonize pDOPA and reduce cGO, pDOPA-cGO-Si powder was heat treated in the same way as the other powders.

3.1.4 Materials Characterization

Scanning electron microscope (SEM) images were taken on a field emission scanning electron microscope (Zeiss LEO1550) with an acceleration voltage of 10 kV. The size distributions of crGO and crGO-Si prepared at varying conditions were obtained by counting at least 100 composite particles in SEM images for each sample. Thermogravimetric analysis (Q500, TA Instruments) was performed by heating the sample under air flow from room temperature to 650°C at a rate of 5°C/min. Transmission electron microscope (TEM) images were taken on an energy-filtered transmission electron microscope (Zeiss Libra 200MC) with

an acceleration voltage of 200 kV. A Bruker energy-dispersive X-ray spectrometer (EDX) system integrated into the TEM system was used for elemental mapping, and Fourier-transform infrared (FTIR) spectra were acquired using an FTIR spectrometer (PerkinElmerSpectrum TwoTM). Hydrodynamic radii were determined by dynamic light scattering (DLS, Zetasizer Nano-ZS90, Malvern). X-ray photoelectron spectroscopy (Thermal Scientific KAlpha XPS spectrometer, 150 eV) was carried out to analyze the surface elemental composition and chemical bonding. XRD was carried out using an XRG 3000 X-ray diffractometer (Cu Kα radiation). An FEI Titan 80-300 LB was used to obtain high-resolution TEM (HRTEM) images of cpDOPA-crGO-Si. The specific surface area of various samples was measured by Micrometritics Gemini VII surface area analyzer based on Brunauer–Emmett–Teller (BET) theory.

3.1.5 Electrochemical Testing

In order to investigate and compare the electrochemical performance of crGO-Si and cpDOPA-crGO-Si prepared at varying conditions, the working electrode was prepared by mixing active material, carbon black (carbon super P, MTI) and sodium alginate (Sigma Aldrich) in DI water with a mass ratio of 65:20:15 using a rotor/stator homogenizer. The resulting slurry was cast onto copper foil by a typical film casting doctor blade method, followed by drying at 80°C under vacuum overnight. All rate capability and cyclic stability results were obtained by assembling the fabricated working electrode (~ 1 mg/cm^2 of active material for all studies except for Figure 3.14b, where ~ 2.5 mg/cm^2 of active material was applied) with a lithium metal foil (Sigma Aldrich, 99.9% trace metal basis) in a coin-type

half-cell. A Whatman glass microfiber (Grade GF/A) was used as a separator, and 1 M $LiPF_6$ in a 1:1 v/v mixture of ethylene carbonate (EC) and dimethyl carbonate (DMC) containing 5 vol.% FEC purchased from Canrd China was used as electrolyte. All cells were assembled in an Ar-filled glove box (< 1 ppm O_2 and water) and cycled between 0.01 V and 1.5 V versus Li/Li^+ using a LANHE multi-channel battery tester (Wuhan LAND Electronics Co.). Electrochemical impedance spectroscopy (EIS) was carried out on a SP-300 potentiostat (BioLogic) in the range of 1 MHz to 100 mHz with an AC amplitude of 10 mV. Nyquist plots were recorded after the first full cycle (after one discharge and one charge at 0.1 A/g) or after 200 cycles at 1 A/g. The electrodes were charged (delithiated) to 1.5 V, disconnected from the battery tester and connected to the potentiostat where the OCV was around 1.2 V for each sample. EIS was then carried out at this DC voltage vs. lithium metal.

3.2 Results and Discussion

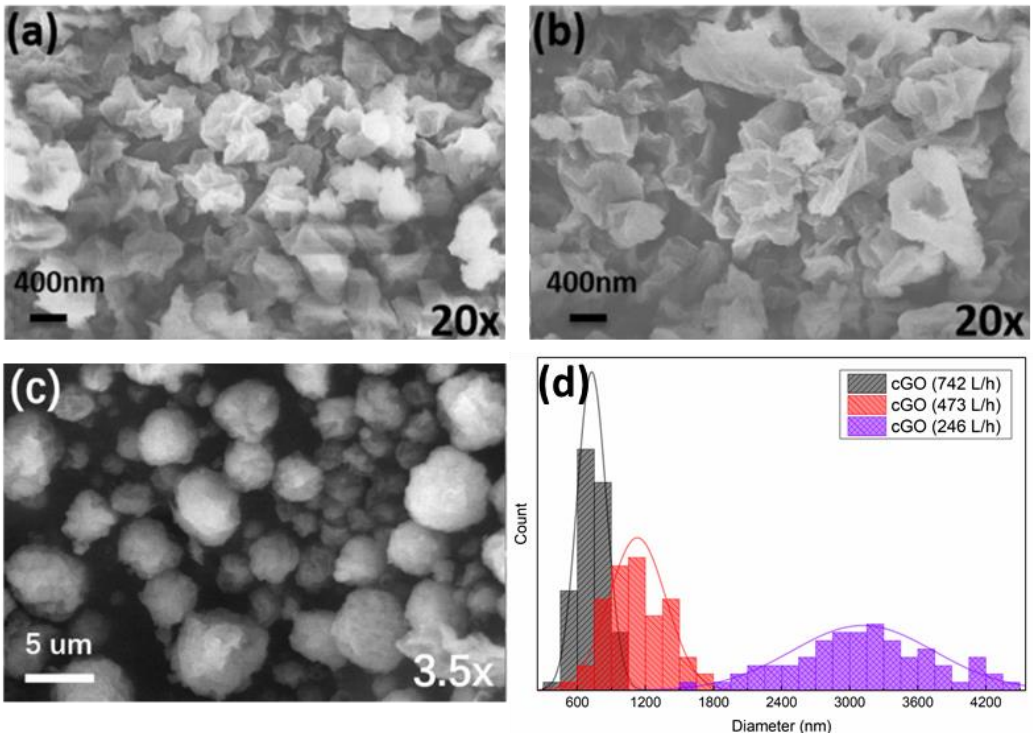

Figure 3.2 SEM images for cGO produced from same concentration (0.5 mg/ml) but at various N_2 flow rate: (a) 742 L/h, (b) 473 L/h, (c) 246 L/h and (d) corresponding size distributions.

In order to achieve the desired highly crumpled GO morphology, we optimized our spray drying conditions to achieve the best operating conditions for our system. This was first carried out with GO only (no silicon) with a concentration (C_f) of 0.5 mg/ml at varying N_2 flow rates (v_f) of 246 L/h, 473 L/h and 742 L/h through the two-fluid atomizer. The resulting powders were then investigated by SEM (**Figure 3.2a-c**). The size distribution for each sample is shown in **Figure 3.2d**. With increasing N_2 flow rate, the average cGO diameter dropped from approximately 3100 nm to 730 nm. The distribution also narrowed with increasing flow as observed by the standard deviation decreasing from approximately 630 nm to 130 nm. The SEM images (Figure S1) revealed the significant morphology changes for samples produced at three different flow rates. At high flow rates, the cGO structures are

more spherical in shape with sharp undulations suggesting a highly crumpled morphology. At lower flow rates the particles transition to a smoother and larger-sized, oblong morphology. The large size difference is attributed to the increasing droplet size expected at lower N_2 flow rates (same solution feed rate in each case). As shown schematically in Figure 1, high velocity N_2 flows through the two-fluid atomizer of the spray dryer and creates droplet sizes which are inversely proportional to the N_2 flow rate. Droplets in the size range of 5 – 30 μm are achievable according to the data provided by the manufacturer.[103] Thus, low N_2 flow rates result in an increase in the number of GO sheets in a single droplet for the same concentration. Since GO is known to accumulate at the interface during droplet evaporation, low flow rates lead to a thicker solid shell. This thicker shell likely prevents the further deformation and shrinkage of microdroplets. On the other hand, the smaller number of GO sheets per droplet at high flow rates leads to a thinner, more deformable shell which is more easily crumpled by the capillary forces generated during evaporative drying. Since Luo et al.[101, 103] demonstrated that the formation of wrinkles enhances the structural stability of crumpled GO, the maximum N_2 flow rate (742 L/h) was used to generate highly crumpled structures for all the samples discussed below.

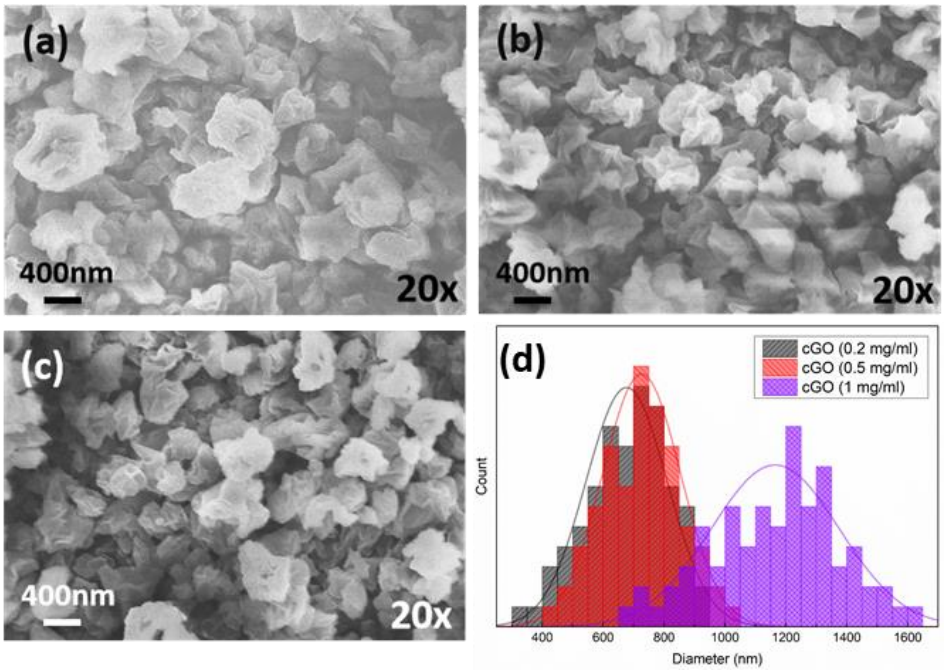

Figure 3.3 SEM images for cGO produced from (a) 1 mg/ml, (b) 0.5 mg/ml and (c) 0.2 mg/ml GO suspension at 742 L/h of N_2 flow rate and (d) corresponding size distributions.

Figure 3.3 shows the size distribution determined by SEM of cGO obtained by spray drying at varying concentrations of GO. While all particles exhibit the similar crumpled morphology, cGO balls are smaller on average with a narrower particle size distribution when decreasing the dispersion concentration from 1 mg/ml (1165 ± 210 nm) to 0.5 mg/ml (726 ± 128 nm), which is attributed to the decreasing number of GO sheets in each microdroplet. However, there is an insignificant change when the concentration was reduced from 0.5 to 0.2 mg/ml. This may be a limit of the spray drying system as the cyclone collector can only efficiently capture particles down to ~1 μm. Since the average size of the resultant particles is close to the threshold, a significant amount of powder may pass to the filter just prior to the system's exhaust instead of being collected by the cyclone (Figure 1). This hypothesis is supported by the drop in the yield observed from > 70% at 0.5 mg/ml to < 40% at 0.2 mg/ml. Hence we chose to move forward with cGO prepared at the N_2 flow rate

of 742 L/h and the concentration of 0.5 mg/ml as the combination exhibiting a smaller particle size, a narrower size distribution and a relatively good yield with highly crumpled morphology which we expect would form a more efficient conductive network to electrically contact Si and minimize the effect of volume change in the electrodes.

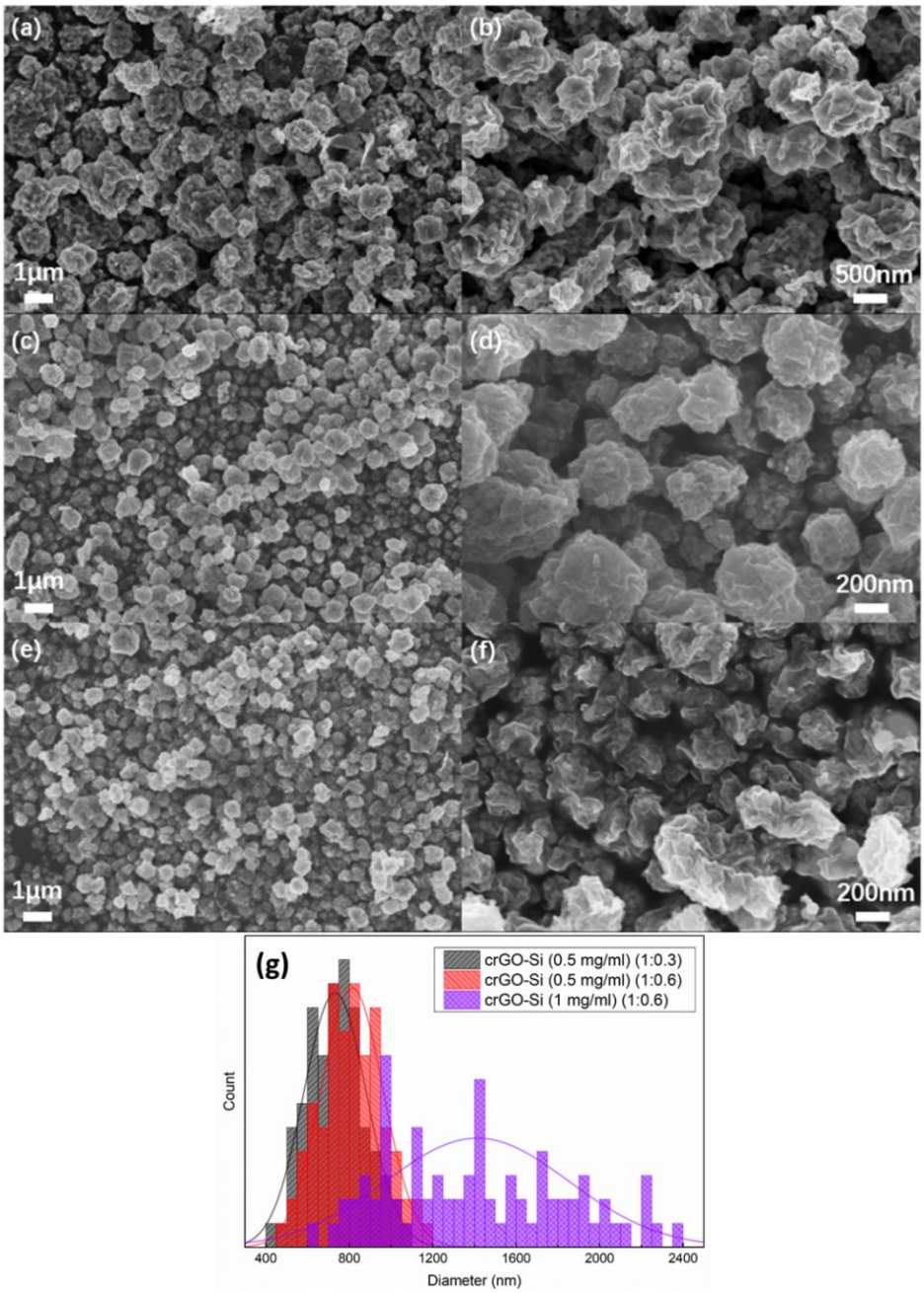

Figure 3.4 SEM images of (a,b) crGO-Si (1:0.6) (1 mg/ml), (c,d) crGO-Si (1:0.6) (0.5 mg/ml) and (e,f) crGO-Si (1:0.3) (0.5 mg/ml) prepared at 742 L/h of N_2 flow rate and (g) corresponding size distributions.

To incorporate silicon into the cGO, we added Si nanoparticles to the 0.5 mg/ml dispersions and tested two different GO to Si mass ratios (1:0.6 and 1:0.3). To investigate the impact of an increased particle size on the performance, we also prepared samples at a dispersion concentration of 1 mg/ml and a GO to Si mass ratio of 1:0.6. The size distributions of the Si-modified powders obtained are plotted in **Figure 3.4g**. Due to the increased solids loading in each droplet (i.e., additional Si), a slight shift to larger diameters compared to that of the unfilled cGO can be observed. All samples displayed a similar crumpled morphology as shown in **Figure 3.4a-f**. There are no silicon nanoparticles evident in the images even under high magnification suggesting that most, if not all, of the Si nanoparticles are trapped inside the crGO shells. The formation of this core-shell structure is attributed to the diffusivity difference between GO and Si nanoparticles, which is caused by their different hydrodynamic radii (**Figure 3.5b**). Convectionwithin the droplet during drying (droplet shrinkage) generates the flow of dispersed components to the droplet surface. The resulting concentration gradient causes diffusion in an attempt to redistribute the particles about the droplet volume. The competition between the characteristic time-scales associated with these two transport processes is typically quantified by the Peclet number (Pe):[104]

$$Pe = \frac{Convection}{Diffusion} = \frac{R_i^2}{D \cdot t_{dry}}$$

where R_i is the initial radius of microdroplets, D is the diffusivity of the dispersed component, and t_{dry} is the drying time. Since the Si nanoparticles are much smaller in hydrodynamic radius than GO sheets (~ 41 nm vs. ~ 660 nm on average), according to the Stokes-Einstein relations, they have a much higher diffusivity than that of GO sheets. Thus, Si nanoparticles

quickly diffuse to the core to maintain a uniform concentration during droplet shrinkage while the GO sheets accumulate at the air/water interface.[88, 105] The drying time of the droplet in this system is unknown. However, the droplet's residence time has been estimated to be ~1.5 s in a previous work that used the same spray drying system.[89] A drying time of ~ 0.1 - 10 ms has also been estimated[101] suggesting drying occurs nearer the inlet. The effect of N_2 flow rates and feed concentrations on the resulting morphology of crGO-Si is summarized in **Figure 3.5a**, samples prepared at high v_f and low C_f displayed a thin shell and small diameter core.

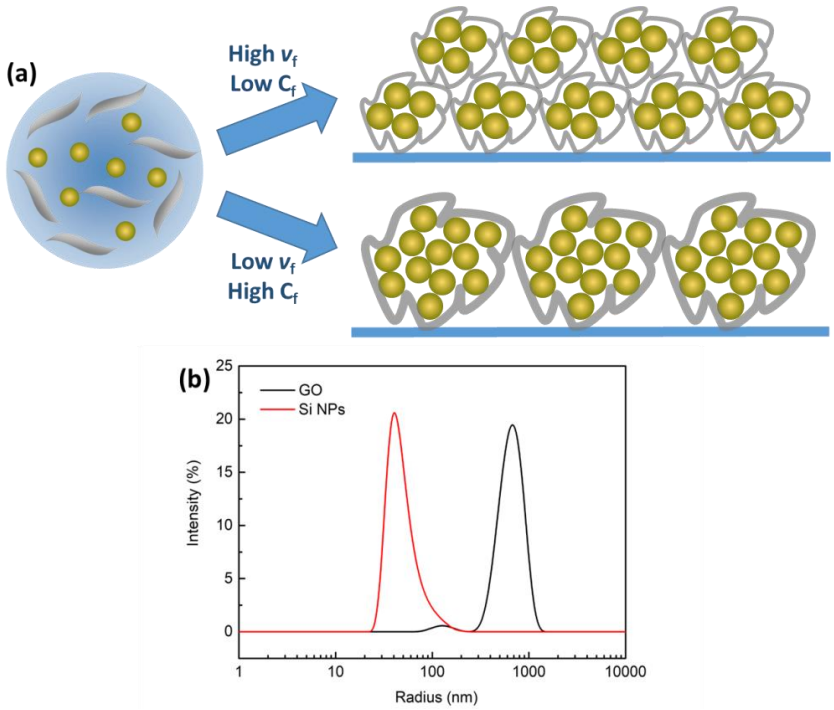

Figure 3.5 (a) Relationship between processing parameters and resulting morphology of crGO-Si, (b) hydrodynamic radius of GO sheets and Si nanoparticles before spray drying

To evaluate and compare the performance of these core-shell structures as anodes, crGO-Si electrodes with the three different ratios were cycled at varying current densities from 0.1 A/g to 4 A/g as shown in **Figure 3.6a**. In this work, all gravimetric capacities are

reported based on the total mass of Si and carbon shell (including rGO and cpDOPA). For the same GO/Si ratio (1:0.6), the sample prepared with a GO concentration of 0.5 mg/ml retained a higher capacity (38% of 1849 mAh/g at 0.1 A/g) at 4 A/g compared to that of

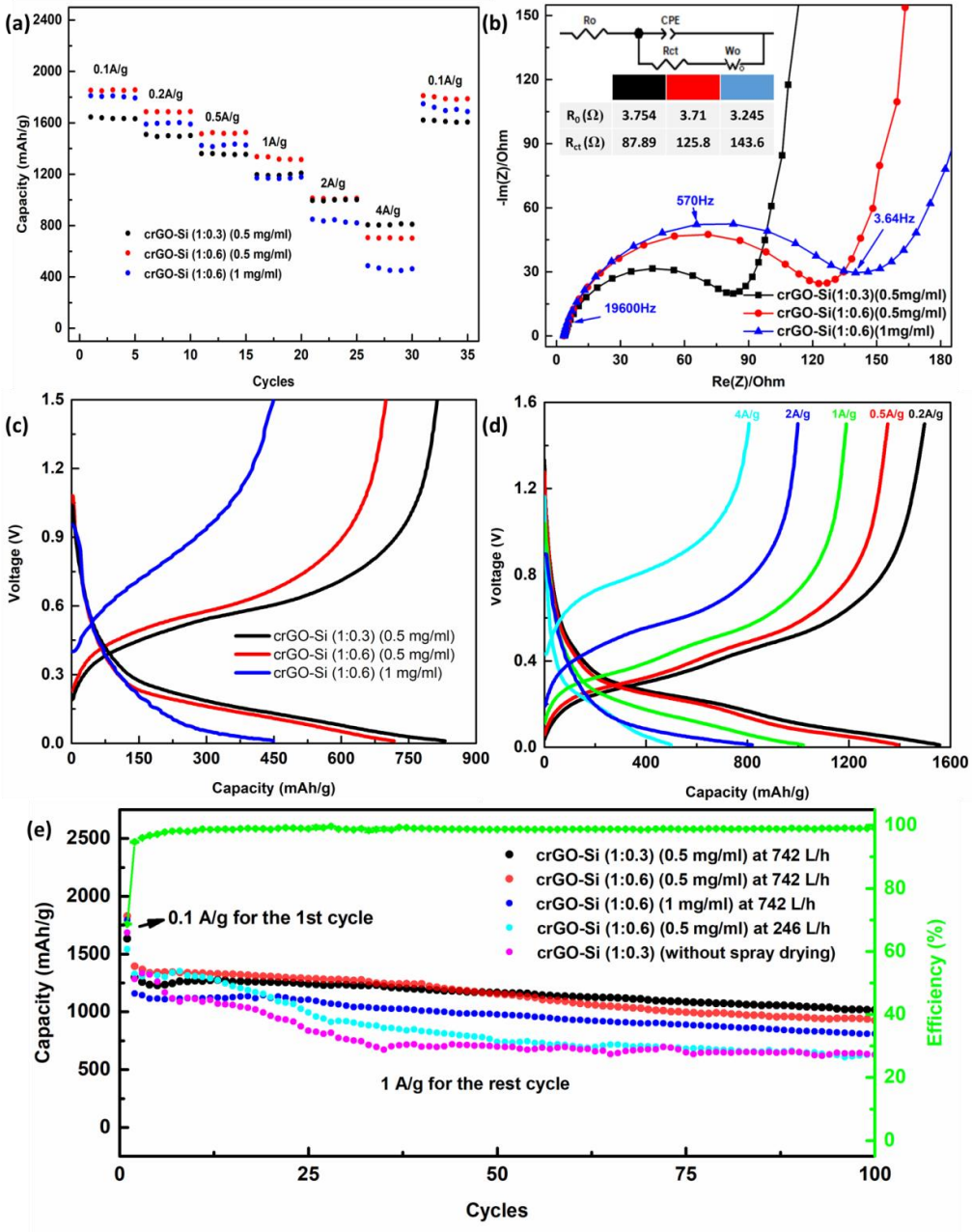

Figure 3.6 Electrochemical performance of various crGO-Si composites: (a) rate performance; (b) Nyquist plots after the 1st cycle at 1.2V vs. Li. The equivalent circuit used is shown in the inset; (c) charge/discharge curves at 4 A/g; (d) charge/discharge curves of crGO-Si (1:0.3) (0.5 mg/ml) at varying current densities; (e) long-term cycling performance.

sample prepared at 1 mg/ml (25% of 1793 mAh/g at 0.1 A/g) at the same current density. This result aligns with our expectation (**Figure 3.5a**) that crGO-Si prepared at low concentration results in smaller structures with less silicon in its core leads to a more efficient conductive network. For the same GO concentration (0.5 mg/ml), crGO-Si prepared at the GO/Si ratio of 1:0.3 displayed a higher capacity at 4 A/g (49% of 1631 mAh/g at 0.1 A/g) exceeding the capacity of crGO (1:0.6) (0.5 mg/ml) at 2 A/g even with a lower content of Si. Since rGO is more conductive compared to Si, this result could also be attributed to the higher overall conductivity due to the increased proportion of rGO in the electrode. The improvement in rate capability due to increased conductivity was also evident in the electrochemical impedance spectroscopy (EIS) results (**Figure 3.6b**). The semi-circle in the high frequency region is attributed to charge transfer resistance (R_{ct}) while the straight line in the low frequency region represents the Warburg diffusion process (Z_w).[106, 107] Furthermore, the intersection between the semi-circle and x-axis shows the internal resistance (R_s). All Nyquist plots were well-fitted using the equivalent circuit model shown in the inset of **Figure 3.6b**. The order of the electrode conductivity was determined to be: crGO-Si (1:0.3) (0.5 mg/ml) > crGO-Si (1:0.6) (0.5 mg/ml) > crGO-Si (1:0.6) (1 mg/ml). As shown in **Figure 3.6c-d**, the voltage profiles show the typical shape for lithiation and de-lithiation of silicon with plateaus at ~ 0.3 V - 0.01 V and ~ 0.2 V - 0.6 V, respectively.[55]

The long-term cycling performance of each sample is shown in **Figure 3.6e**. The low conductivity and larger number of Si nanoparticles in one crGO sack caused a dramatic drop in the capacity of crGO-Si (1:0.6) (1 mg/ml) from 1793 mAh/g at 0.1 A/g to ~1178 mAh/g at 1 A/g. Only 67% (795 mAh/g) of the initial capacity was retained after 100 cycles. The curves

for the other two samples, prepared at low concentration, show similar tendencies and retained a reasonable capacity at high current. Howeer, the crGO-Si (1:0.3) (0.5 mg/ml) displayed a much higher capacity of 1016 mAh/g (78% of the initial capacity) while crGO-Si (1:0.6) (0.5 mg/ml) only retained 68% (925 mAh/g) of the initial capacity after 100 cycles. With the protection of optimized crumpled rGO shell, crGO-Si (1:0.3) (0.5 mg/ml) displayed much better cyclic stability compared to that of rGO-Si (1:0.3) which was prepared without spray drying the mixture. Moreover, we also examined the cyclic stability of crGO-Si (1:0.3) (0.5 mg/ml) produced at low N_2 flow rate (246 L/h), whose capacity significantly dropped by 52.5% after 100 cycles. Hence, crGO-Si (1:0.3) (0.5 mg/ml) produced at high N_2 flow rate (742 L/h) exhibited the best cyclic stability given its higher rGO:Si ratio which buffers the volume fluctuation of Si most efficiently among these three samples while maintaining an effective conductive network. From here on, all samples prepared in the following works were based on a GO concentration of 0.5 mg/ml.

Huang et al.[98] directly spray dried and heat treated crGO/Si at 600°C via a modified spray drying system which displayed better cyclic stability (250 cycles vs. 200 cycles for ~ 80% capacity retention) and a higher initial coulombic efficiency (73%) compared to that of crGO (1:0.3) (0.5 mg/ml) (68.6%). We suspect that the reduction step in our procedure might affect the structural stability of cGO/Si due to the possible exfoliation of the GO exposing more Si nanoparticles directly to the electrolyte. Hence, we further reinforced the cGO shell by coating it with an external layer of polydopamine (pDOPA). Inspired by the adhesive nature of mussels for attachment to wet surfaces, pDOPA coating is a simple and versatile method for surface functionalization through spontaneous self-polymerization of DOPA

monomers in basic aqueous solutions.[108] The following heat treatment converts the pDOPA into a nitrogen-doped carbon layer on the surface of crGO which could improve both cyclic stability and charge transfer. To confirm the successful coating of pDOPA, FTIR was carried out on pure cGO and pDOPA-cGO as shown in **Figure 3.7a**. Two new peaks emerged in the spectra of pDOPA-cGO related to N-H bond and C-N bond at 1504 cm^{-1} and 1385 cm^{-1} respectively, suggesting the existence of nitrogen-containing groups that were introduced by

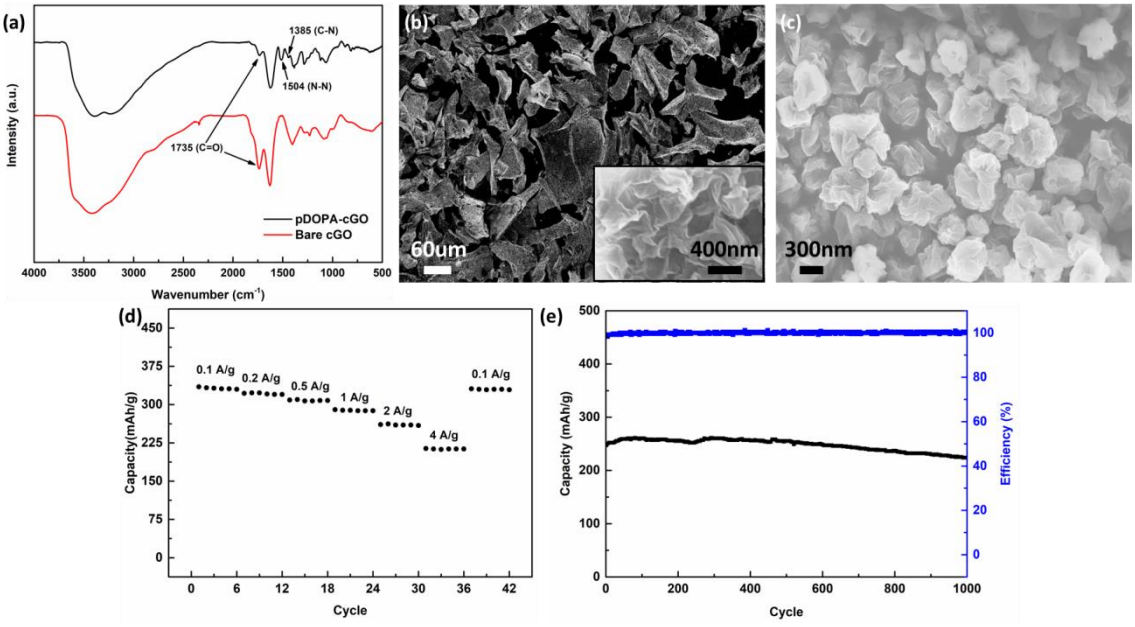

Figure 3.7 Characterization of pDOPA-coated cGO and crGO: (a) FTIR spectra of cGO and pDOPA-cGO; SEM images of cGO stirred in DI water for 24 hours without pDOPA (b) and with pDOPA (c); (d) rate performance and (e) cyclic stability of cpDOPA-crGO scaffold at 2 A/g.

the polydopamine layer. And GO was partially reduced during the polymerization of dopamine, as indicated by the decreased peak intensity at 1735 cm^{-1} (C=O) in the spectra of cGO.[109] Furthermore, pure cGO and pDOPA-cGO were stirred in DI water for 24 hours and then freeze dried for SEM analysis as shown in **Figure 3.7b** and **3.7c**, respectively. All pure cGO sacks are found to have a completely different morphology upon re-dispersion in water. They no longer appeared as crumpled balls but thick lamellae suggesting that the rGO

unfolded and aggregated in water resulting in the collapse of crumpled structure. On the other hand, the pDOPA-cGO sacks are able to maintain their original crumpled morphology. This suggests that the pDOPA effectively “glued” the structure together and prevented it from restructuring in water. The polymerization reaction involving pure dopamine only takes a few minutes as indicated by the rapid change in color from transparent to light brown, implying that this process is faster than the restructuring of cGO in water. Furthermore, pDOPA is also found to enhance the structural stability of cGO during heat treatment as shown in **Figure 3.8**. Without the pDOPA coating, the cGO exfoliated in the tube furnace due to the rapid expansion of gases generated upon thermal reduction of GO to rGO. The pDOPA coating rigidified the structure enabling the gases to escape without undergoing damaging expansion.

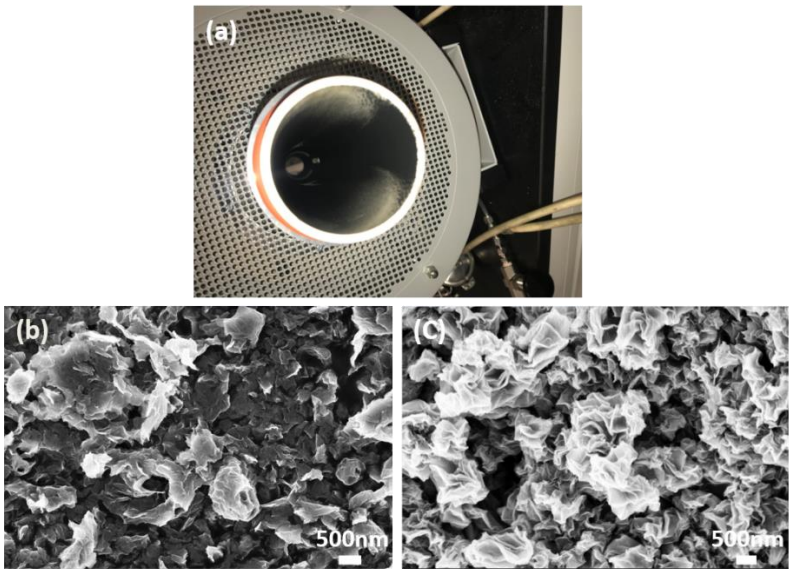

Figure 3.8 (a) Pure cGO exfoliated during reduction, SEM images for exfoliated cGO (b) and polydopamine coated crGO (c) after being heated to 800 ℃.

Cell performance of pDOPA-crGO without Si was first investigated to study the electrochemical stability of the carbonaceous material formed. Cells assembled using this

material were cycled at varying current densities ranging from 0.1 A/g to 4 A/g (**Figure 3.7d**), exhibiting a relatively small drop in capacity from 323 mAh/g to 216 mAh/g. Additionally, as shown in **Figure 3.7e**, cpDOPA-crGO displayed excellent cycling stability with an average coulombic efficiency of > 99.9% and only ~10% loss in capacity observed over 1000 cycles. According to these results, cpDOPA-crGO is a stable carbon scaffold which will be used to protect Si nanoparticles as discussed in the sections to follow.

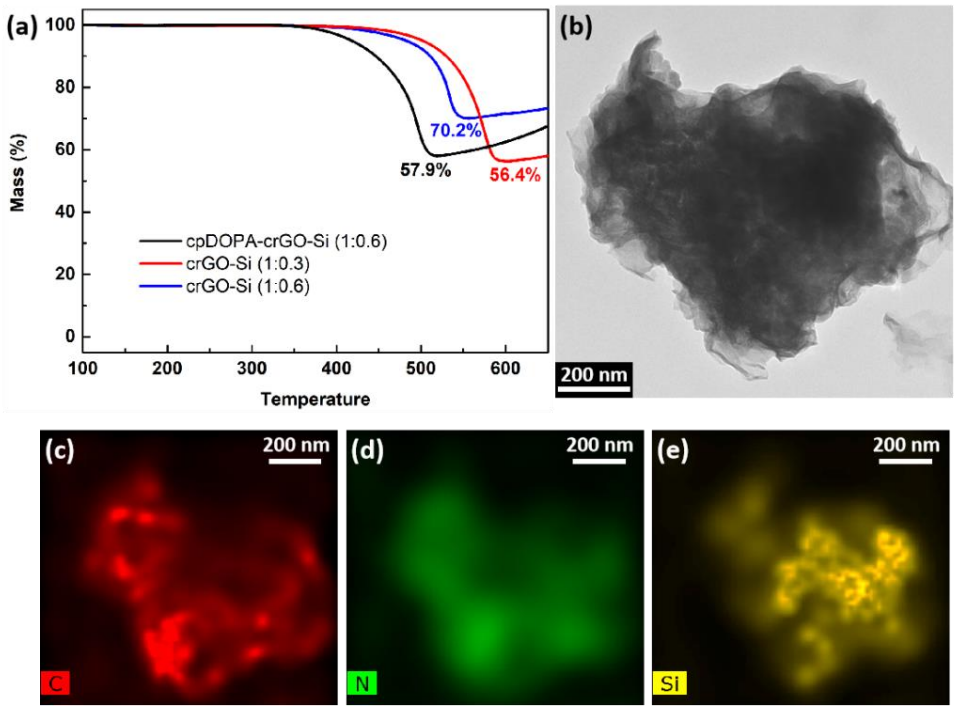

Figure 3.9 Characterization of crGO-Si composites with and without cpDOPA coating: (a) TGA curves of varying samples; (b) TEM image of a single cpDOPA-crGO-Si ball and elemental mapping images showing the distribution of carbon (c), nitrogen (d) and silicon (e).

After the addition of Si nanoparticles into cpDOPA-crGO based on a GO/Si ratio of 1:0.6, we first investigated the amount of cpDOPA coated on the surface of crGO-Si using TGA where samples were pyrolyzed under air flow to 650°C. As shown in **Figure 3.9a**, there is a significant mass loss at around 500°C which should be attributed to the decomposition of the carbonaceous materials. Some mass gain is observed at higher temperatures due to the

oxidation of Si nanoparticles. Since the addition of cpDOPA would not affect the mass ratio between crGO and Si, according to the carbon content detected in cpDOPA-crGO-Si (1:0.6) and crGO-Si (1:0.6), the content of cpDOPA is calculated to be around 17.5wt%. Here, it should be noted that the cpDOPA is coated on crGO-Si (1:0.6) rather than crGO-Si (1:0.3), which exhibited better electrochemical performance, in order to maintain its theoretical capacity by avoiding the use of too much carbon. By comparing cpDOPA-crGO-Si (1:0.6) and crGO-Si (1:0.3) containing similar carbon content, a fairer conclusion can be drawn about whether or not the extra cpDOPA sealing can help to improve the electrochemical performance of our materials. A representative TEM image of a cpDOPA-crGO-Si particle is shown in **Figure 3.9b**. Some parts near the outside of the crumpled structure are nearly transparent to the electron beam and are likely just folds of pDOPA-coated rGO. The inner structure is much darker in contrast likely due to the denser Si-containing core. According to the EDX mapping for carbon, nitrogen and silicon shown in **Figure 3.9c-e**, silicon is concentrated in the core and the texture of individual silicon nanoparticles approximately 50 nm in diameter can be seen. A strong carbon signal throughout the sample and a lower intensity nitrogen signal are detected and distributed uniformly across the crGO surface. HRTEM was carried out on the crumpled edge of a cpDOPA-crGO-Si (1:0.6) sample at varying magnifications as shown in **Figure 3.10**. The resulting images clearly suggest that silicon nanoparticles are covered by a layer of rGO combined with amorphous carbon (cpDOPA) with a thickness of ~5 nm. The lattice fringes (d = 0.31 nm) reflect the (111) crystal face of Si,

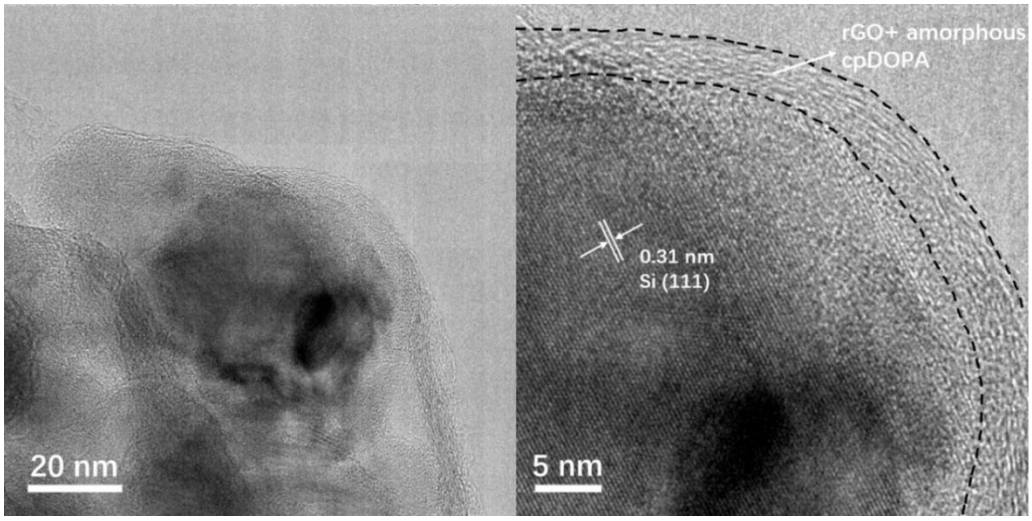

Figure 3.10 High-resolution TEM images of cpDOPA-crGO-Si (1:0.6) at low (a) and high (b) magnifications.

indicating that the Si nanoparticles inside are still highly crystalline. After spray drying, Si NPs were not be significantly oxidized as indicated by a negligible increase in oxygen content observed by EDX and no additional peaks appearing in the XRD profiles as shown in **Figure 3.11**.

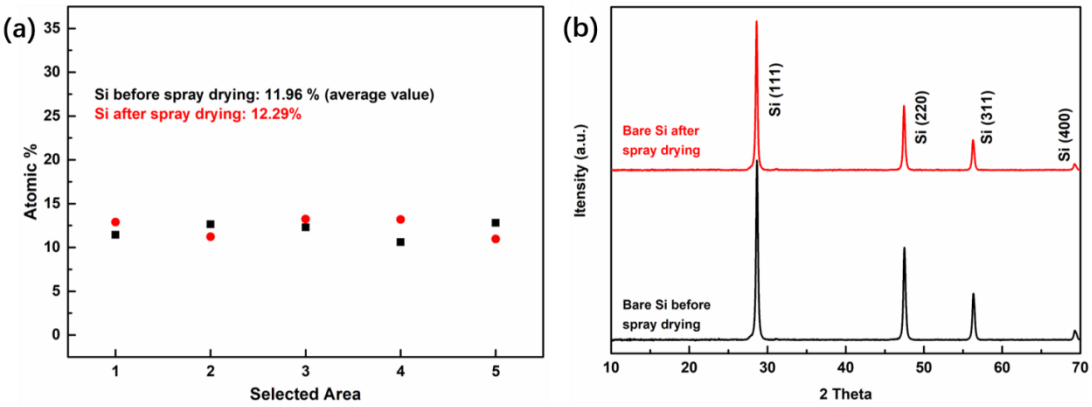

Figure 3.11 (a) SEM-EDX results for oxygen content from 5 randomly selected area (10μm x 10μm) and (b) XRD patterns for Si NPs before and after spray drying

XPS was carried out to characterize the surface elemental composition of bare silicon, crGO-Si (1:0.3) and cpDOPA-crGO-Si (1:0.6). As depicted in **Figure 3.12a**, the presence of a N 1s peak in the spectrum of cpDOPA-crGO-Si (1:0.6) suggests the successful introduction

ofcpDOPA. Approximately 1.21% N is doped into the carbon shell. Moreover, according to the surface elemental analysis, the silicon content decreased from 47.5% to 7.68% while the carbon content increased from 27.14% to 73.49% after spray drying and heat treatment together with GO sheets. This reduction in the silicon signal, due to the short penetration depth of the XPS system, demonstrates that rGO effectively covers the surface of the Si nanoparticles. After the coating of cpDOPA, the Si content dropped further to 2.13% while the carbon content reached 82.38%. To obtain chemical bonding information, we carried out a more detailed analysis for the C 1s peak and N 1s of cpDOPA-crGO-Si (1:0.6). For the C 1s spectrum (**Figure 3.12b**), the main peak was well-fitted and deconvoluted into three peaks which are attributed to O-C=O (288.9 eV), C-N (285.7 eV) and C-C (284.8 eV).[110, 111] The small area of O-C=O illustrates that most oxygen containing groups were removed during heat treatment, and the presence of C-N suggests the doping of nitrogen due to the coating of cpDOPA. To determine the type of doped nitrogen in this material, we also did peak fitting for the N 1s spectrum. As shown in **Figure 3.12c**, the three peaks are assigned to graphitic nitrogen (403.6 eV), pyrrolic nitrogen (400.4 eV) and pyridinic nitrogen (397.9 eV), respectively.[110, 111] XRD profiles are plotted in **Figure 3.12d**. The peaks at 28.4°, 47.3°, 56.1° and 69.1° were assigned to (111), (220), (311) and (400) lattice planes of crystalline silicon, respectively. A broad and nearly undiscernible peak around ~27° in the XRD pattern of crGO-Si indicates that the rGO shell indicates little to no restacking of the rGO.[112] However, this peak effectively disappears after the introduction of cpDOPA which, as expected, forms an amorphous carbon layer.

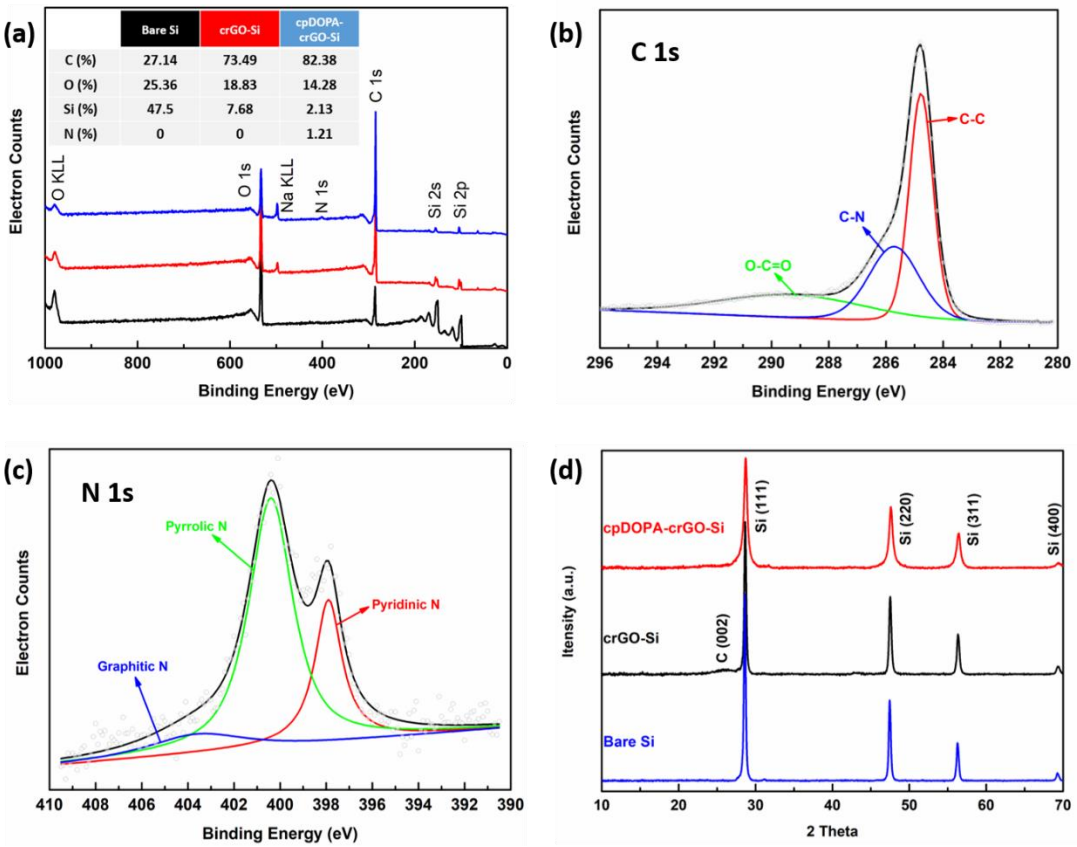

Figure 3.12 Characterization of crGO-Si, cpDOPA-crGO-Si and bare Si: (a) high-resolution XPS survey spectra of varying samples; high-resolution XPS narrow scan spectra of cpDOPA-crGO-Si for C 1s (b) and N 1s (c); (d) XRD patterns of varying samples.

Galvanostatic charge/discharge testing and EIS were carried out on cpDOPA-crGO-Si (1:0.6) to demonstrate the improvement in cell performance by adding the cpDOPA coating as compared to samples without the coating. As shown in **Figure 3.13a**, cpDOPA-crGO-Si (1:0.6) delivered 1672 mAh/g at 0.1 A/g which dropped to 975 mAh/g at 4 A/g retaining 58% of its capacity at the high rate of lithiation. In contrast, crGO-Si (1:0.3) retained only 49% of its initial capacity at 0.1 A/g after the current density was increased to 4 A/g. The improved rate capability suggests that the conductive network is further improved in the cpDOPA-coated sample, which is consistent with the results of EIS where cpDOPA-crGO-Si (1:0.6) exhibited the smallest R_{ct} (72 Ω) as indicated by the smallest semi-

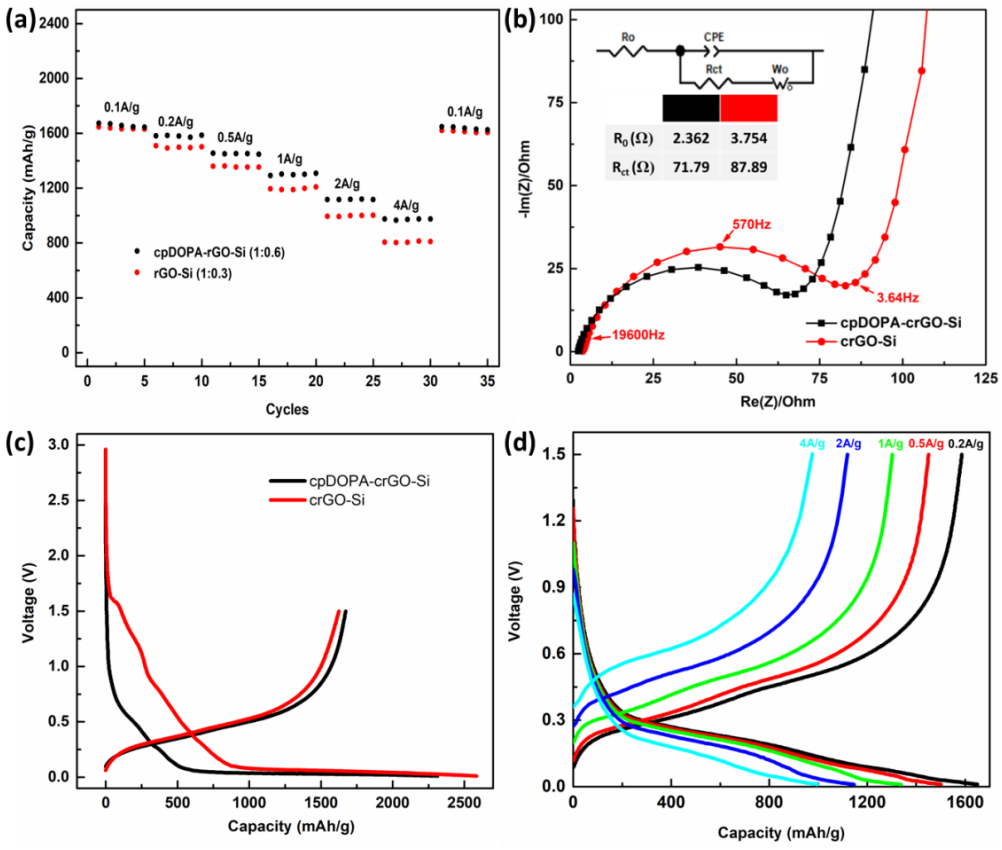

Figure 3.13 Electrochemical performance of crGO-Si composites with and without cpDOPA coating: (a) rate performance, (b) Nyquist plots after the 1st cycle and equivalent circuit (inset); (c) first charge/discharge curves at 0.1 A/g; (d) charge/discharge curves of cpDOPA-crGO-Si (1:0.6) at varying current densities.

-circle in the high frequency region of the Nyquist plot (**Figure 3.13b**). Although cpDOPA-crGO-Si (1:0.6) has a similar carbon content to that of crGO-Si (1:0.3), the nitrogen-doped carbon coating provided a more efficient pathway for lithium-ion transfer. The first charge/discharge curves of cpDOPA-crGO-Si (1:0.6) and crGO-Si (1:0.3) are plotted in Figure 7c, the sharp slope at ~ 1.5 V - 0.1 V in the first discharge curve indicates the formation of the SEI layer while the long platform at ~ 0.1 V - 0.01 V is attributed to the transformation from crystalline Si to an amorphous Li_xSi. And crGO-Si (1:0.3) exhibited more irreversible capacity to form an SEI layer, leading to a lower initial coulombic efficiency (68.6%) compared to 76.3% for the cpDOPA-crGO-Si (1:0.6). The improvement suggests that

the cpDOPA-crGO shell may better seal the Si from direct contact with the electrolyte than just the crGO alone. For reference, pure Si exhibited an even poorer initial coulombic efficiency of 57.2%. The improvement in initial coulombic efficiency may also be explained by the significant drop in surface area estimated by gas adsorption of 48.4 m^2/g to 9.2 m^2/g before and after the cpDOPA coating procedure, respectively. After the first discharge, the silicon anode only converts between amorphous Li_xSi and amorphous silicon corresponding to the typical potential plateaus at ~ 0.3 V - 0.01 V during discharging and ~ 0.2 V - 0.6 V during charging as shown in **Figure 3.13c** and **3.13d**.[53] With increasing current density, the polarization of Si led to an apparent increase in the delithiation potential and reduction the of lithiation potential.

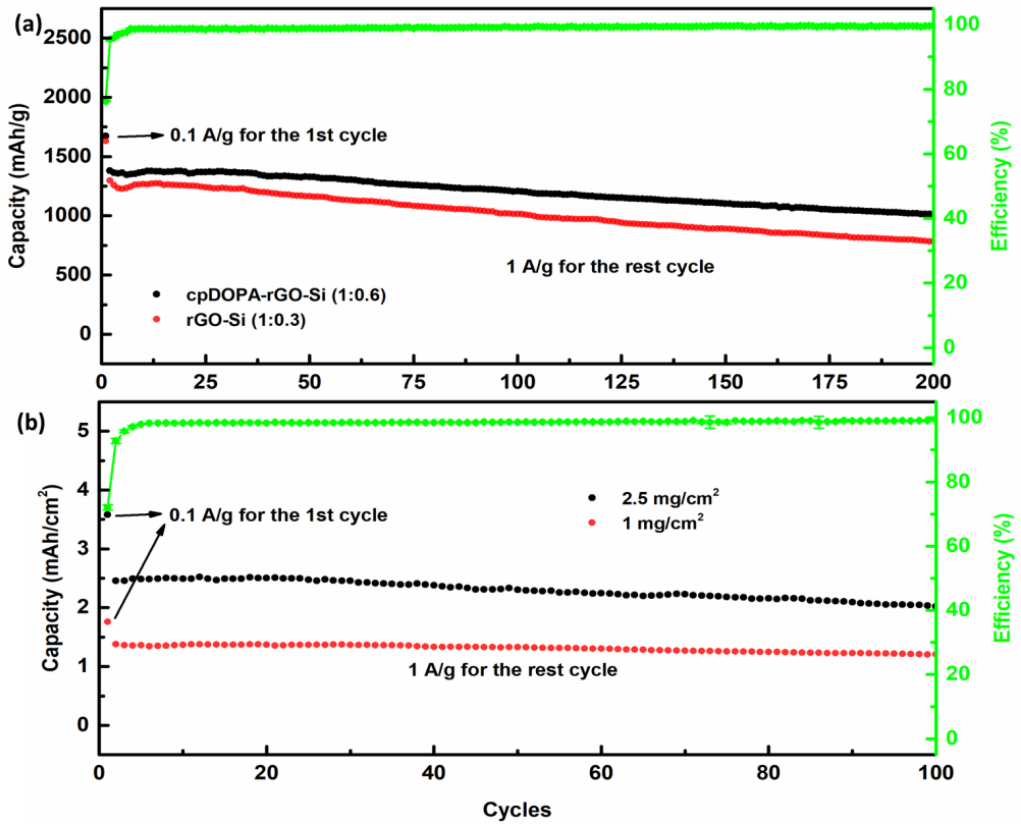

Figure 3.14 Cyclic stability of cpDOPA-crGO-Si with varying loadings: (a) Comparison of cycle life between crGO-Si and cpDOPA-crGO-Si; (b) cycling stability of cpDOPA-crGO-Si with an increased mass loading.

The long-term cyclic stability of cpDOPA-crGO-Si (1:0.6) was investigated by galvanostatic charge/discharge and compared to uncoated crGO-Si (1:0.3) as shown in **Figure 3.14a**. cpDOPA-crGO-Si (1:0.6) displayed an outstanding cyclic stability, which only dropped from 1379 mAh/g to 1206 mAh/g after 100 cycles and 1038 mAh/g after 200 cycles with corresponding capacity retentions of 87.5% and 75%, respectively. Uncoated crGO-Si (1:0.3) only achieved a capacity of 783 mAh/g after 200 cycles, exhibiting a capacity decay rate of 0.20%/cycle which is significantly worse than the cpDOPA coated sample where a decay rate of 0.12%/cycle is observed. The SEM images of cpDOPA-crGO- Si (1:0.6) after 200 cycles are shown as in **Figure 3.15a** and **b**, which indicates no obvious cracking or delamination and

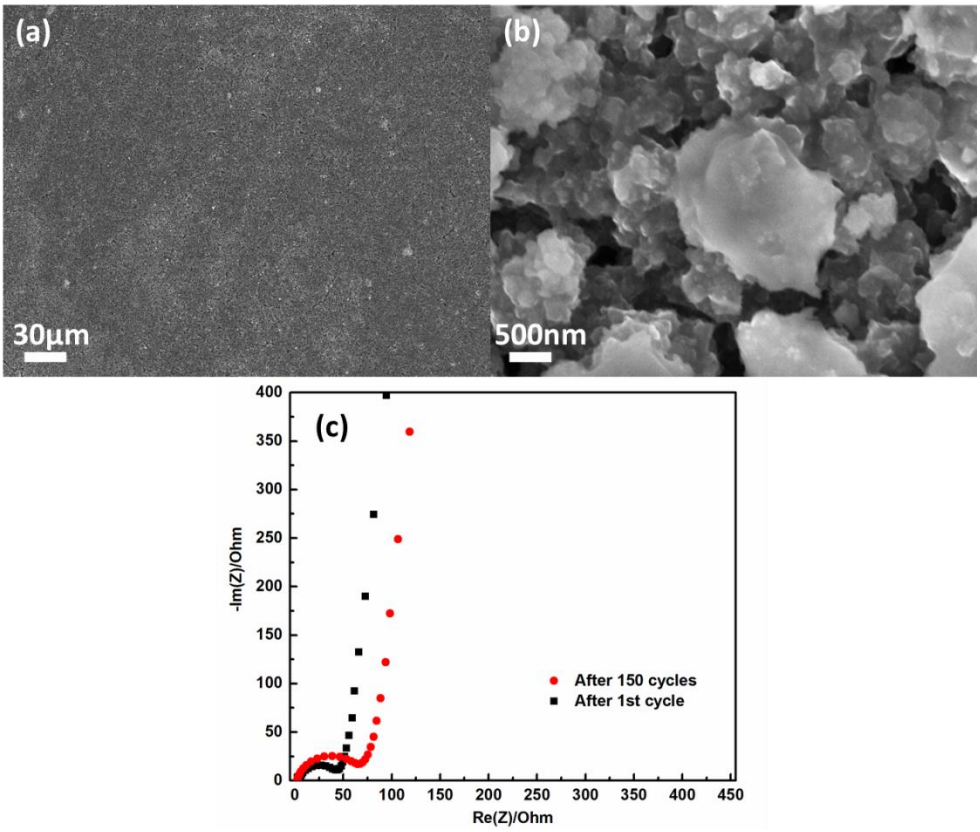

Figure 3.15 SEM image for cpDOPA-crGO-Si after 200 cycles at low magnification (a) and high magnification (b), (c) Nyquist plots for cpDOPA-crGO-Si (1:0.6) after the 1st cycle and the 200th cycle

that the original crumpled structure of the crGO appears largely maintained. The Nyquist plot of cpDOPA-crGO- Si (1:0.6) after 200 cycles was also measured and plotted in **Figure 3.15c**, which still exhibited a similar shape, comprised of a semi-circle at high frequency region and a straight line at low frequencies compared to the plot obtained after the 1st cycle. The small increase in the semi-circle diameter indicates that this cpDOPA coated crGO-Si can maintain a relatively intact electrochemical structure even after long-term cycling. Based on the capacity of pure cpDOPA-crGO shell (323 mAh/g at 0.1 A/g and 216 mAh/g at 4 A/g as shown in **Figure 3.7d**) and TGA analysis (containing ~42.1 wt% of carbon as shown in **Figure 3.9a**), we calculated the contribution of carbon in cpDOPA-crGO-Si (1:0.6) which suggests that only 8.1% and 9.3% of capacity should be attributed to the carbon shell at 0.1 A/g and 4 A/g, respectively. Based on the above calculations, the silicon alone displayed capacities of ~2654 mAh/g at 0.1 A/g and ~1527 mAh/g at 4 A/g, which is around 73.9% and 42.5% respectively of its theoretical capacity (3590 mAh/g) at room temperature.[113] To meet the high energy densities required for practical application of this battery technology, we also checked the cycling stability of cpDOPA-crGO-Si (1:0.6) with increased active material loading (2.5 mg/cm^2). Even with a 2.5× increase in mass loading, this material still showed a promising cycle life as shown in **Figure 3.14b**. The areal capacity of cpDOPA-crGO-Si (1:0.6) only dropped from 2.46 mAh/cm^2 to 2.05 mAh/cm^2 after 100 cycles, and this capacity is very closed to the value of commercial graphite anodes.[114] Hence, we can conclude that the coating of cpDOPA significantly improved the structural stability of crGO-Si composite. Compared to other Si/C anodes prepared based on the same spray drying technique (**Table 3.2**), cpDOPA-crGO-Si displayed

competitive capacity and improved cycling stability with a simple and efficient production process. Although Yan et al.[112] very recently conducted a similar polydopamine coating method, our material exhibited better cycle life and used much less electrolyte additives (5% FEC vs. 10% FEC & 2% vinylene carbonate (VC)), which is attributed to the optimization of spray drying parameters.

Table 3.1 The 1st coulombic efficiency of varying samples

	cpDOPA-crGO-Si (1:0.6)	crGO-Si(1:0.3)	crGO-Si(1:0.6)	Pure Si
1st Coulombic efficiency	76.3%	68.6%	64.2%	57.2%

Table 3.2 Summary of recent works about Si/C anode using spray drying technique

Material	Initial capacity during cycling (mAh/g)	No. of cycles (retention)	Journal [ref.]	Note
C – Si/cGr	~1250 mAh/g at 0.5C	100 (63%)	Curr Appl Phys, 2019[117]	
Si/C-3	1397 mAh/g at 0.2 A/g	300 (37%)	Electrochim. Acta, 2019[118]	
MSC250	1555 mAh/g at 0.5C	500 (87%)	Electrochim. Acta, 2019[124]	10% FEC
PSi/C	1357.43 mAh/g At 0.1 A/g	100 (69%)	ACS Appl. Mater. Interfaces, 2018[121]	
PSNGM	1340 at 0.1 A/g	150 (87%)	Electrochim. Acta, 2016[98]	

Si@C@CNT-PG	820 mAh/g at 0.2C	100 (84%)	J. Alloys Compd. 2019[114]	5% FEC
Si/C@NGs	483.3 at 0.1 A/g	100 (88%)	Chem. Eng. J. 2017[125]	
Si/CNT/C	1989 at 1 A/g	100 (70%)	J. Power Sources, 2018[175]	
Si@G@PDA-C	1200 at 1 A/g	150 (84.8%)	ACS Appl. Mater. Interfaces, 2019[136	10% FEC and 2% VC
Si@crumpled GO	1132 at 1 A/g	250 (83%)	J. Phys. Chem. Lett., 2012[97]	
Si/C/rGO	947 at 0.1 A/g	70 (98%)	J. Electroanal. Chem., 2017[119]	
Si@po-C	1366 at 4 A/g	150 (91%)	Nano Lett., 2013[146]	5% FEC, HF-etching
Si@C@rGO	1599 at 0.1 A/g	100 (94.9%)	J. Alloys Compd., 2017[122]	
Si@FL-GB	1499 at 0.5 A/g	100 (70.9%)	Nanoscale, 2020[178]	5% FEC
cpDOPA-crGP-Si	**1379 mAh/g at 1 A/g**	**200 (75%)**	**This work**	**5% FEC**

3.3 Conclusions

In summary, the effect of feed concentration, nitrogen flow rate and GO/Si ratio on the resulting physical morphology, size distribution and battery performance of crGO-Si was evaluated. It is confirmed that a highly crumpled structure with a small and uniform size

distribution is produced at high N_2 flow rate of approximately 742 L/h and a diluted GO dispersion concentration of 0.5 mg/ml with a low GO/Si ratio (1:0.3), which resulted in an electrode with the highest structural stability and most efficient conductive network to buffer the volume change of Si. When cycled at a current density of 1 A/g in the range of 0.01 V to 1.5 V, crGO-Si (1:0.3) (0.5 mg/ml) delivered an improved cycle life with a capacity loss rate of 0.20% per cycle over 200 cycles. A layer of nitrogen-doped carbon (cpDOPA) was then coated on the surface of crGO-Si (1:0.6) (0.5 mg/ml) to further enhance the sealing and stability of the Si-C core-shell structure. Based on a carbon content (57.9%) which is similar to that of crGO-Si (1:0.3), cpDOPA-crGO-Si (1:0.6) displayed much better rate capability and cyclic stability. It can still maintain a high capacity of 1007 mAh/g after 200 cycles at 1 A/g, the reinforced material displayed significantly enhanced cycle stability displaying a lower decay rate of 0.12% per cycle. Meanwhile, the optimized initial coulombic efficiency (76.3%) also demonstrated that the addition of cpDOPA coating effectively decreased direct contact of Si by the electrolyte.

4 Controlling Void Space in Crumpled Graphene-Encapsulated Silicon Anodes using Sacrificial Polystyrene Nanoparticles

This chapter is based on a manuscript submitted to ChemSusChem (just accepted), see **Statement of Contributions** for details.

As we discussed in **Chapter 3**, additional sealing of the crumpled graphene shell can lead to improved structural stability. However, we noticed that there was litte void space in the core of the crumpled rGO to buffer volume expansion. Herein, we discuss an approach to control void space in the Si NP core of the crumpled rGO shell using a one-step encapsulation approach. As shown in **Figure 4.1**, polystyrene nanoparticles (PS NPs) of similar size to the Si NPs are spray dried together to obtain a PS/Si composite encapsulated with crumpled GO. Thermal decomposition of the PS and reduction of the GO lead to a composite with void fraction and porosity which is tunable by the PS to Si ratio. The impact of introducing void space in this way on the electrochemical performance of the composite structure was used to determine the optimal PS/Si ratio of 1:1 which displays both the best rate capability and cyclic stability. These electrodes exhibited a high capacity of 1183 mAh/(g_{Si+rGO}) after 200 cycles at 1 A/g with a promising capacity retention of 80.6%. Due to the improved conductive network, 71.9% of initial capacity (1638 mAh/(g_{Si+rGO}) at 0.1 A/g) was retained when current density was increased from 0.1 A/g to 4 A/g.

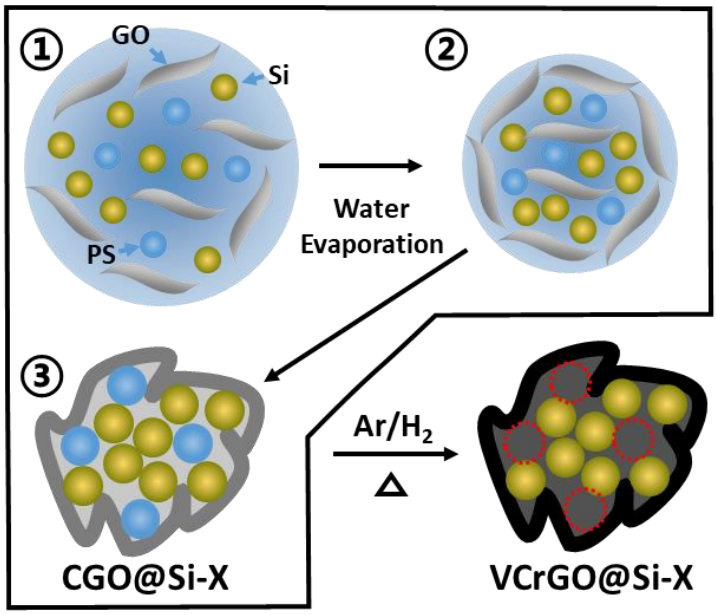

Figure 4.1 Schematic illustration of the synthesis process of voided CrGO encapsulated Si NPs (VCrGO@Si-X, where X is ratio of PS/Si), where the spray drying process (in the box) can be divided into diffusion/convection segregation process (① to ②) and the capillary collapse process (② to ③).

4.1 Experimental Section

4.1.1 Synthesis of Graphite Oxide

Graphene oxide (GO) was synthesized by Tour's modified Hummer's method from graphite flakes (Alfa Aesar, natural, -10 mesh, 99.9% (metals basis)).[102] 360 ml of 98% sulfuric acid (H_2SO_4) and 40 ml of 97% phosphoric acid (H_3PO_4) were continuously stirred in a 3-neck round bottom flask followed by the slow addition of 3g of graphite flakes and 18g of potassium permanganate ($KMnO_4$). The oxidation reaction was conducted in an oil bath at 50°C for 16 h, followed by the addition of 6 ml of hydrogen peroxide to reduce unreacted manganese species when the suspension cooled to room temperature. The resultant suspension was then washed in 10% HCl and then ethanol for three times and four times, respectively via centrifugation (3000 rpm, rotor diameter 15 cm). Finally, a dialysis bag with

12-14 kDa molecular weight cut off (MWCO) was used to transfer GO from ethanol to deionized (DI) water for subsequent steps.

4.1.2 Synthesis of Polystyrene Nanospheres

Polystyrene nanoparticles (PS NPs) were synthesized by emulsion polymerization following the procedure of Zhang et al..[115] In a typical experiment, 72 mg of sodium bicarbonate ($NaHCO_3$, as buffer agent) and 9 mg of sodium dodecyl benzene sulfonate (SDBS, as emulsifier) were dissolved in 33 ml water/ethanol (10:1 in volume) in a single neck round bottom flask. 3 ml of styrene monomer was slowly injected into the mixture which was then agitated by an ultrasonic probe forming a stable white emulsion. The emulsion was then degassed by nitrogen bubbling to remove oxygen under continuous stirring for 30 mins at room temperature. After the reaction system was slowly heated to 80°C, and 30 mg of potassium persulfate (KPS) (20 mg/ml in water) was slowly injected to initiate the polymerization for 7 hours under nitrogen flow protection. The resulting emulsion was broken by adding 2 g of sodium chloride (NaCl), and then washed by DI water and ethanol for four times and three times, respectively via centrifugation (3000 rpm, rotor diameter 15 cm) and re-dispersion of the pellet containing the PS.

4.1.3 Preparation of Electrode Materials

500 mg of GO and 300 mg Si NPs (~50-100 nm, Strem) were dispersed in 1 L of water/ethanol (4:1 by volume). PS NPs were added with four different mass ratios (0:1, 0.5:1, 1:1 and 2:1 of PS:Si) under continuous stirring. The uniformly mixed suspension was

ultrasonicated in a water bath for 30 mins, followed by spray drying using a BUCHI-290 Mini Spray Dryer with input temperature of 200°C, aspirate rate of 100%, and nitrogen flow rate of 742 L/h. The resulting dry powder was placed in an alumina combustion boat and heated under a flowing mixture of argon (95%) and hydrogen (5%) gases from room temperature to 450°C for 2 hours with a ramping rate of 1°C/min, and then heated at 800°C for 3 hours after ramping to this temperature at 5°C/min. The resulting voided crumpled reduced graphene oxide encapsulated Si NPs with varying PS/Si mass ratios are denoted as VCrGO@Si-0, VCrGO@Si-0.5, VCrGO@Si-1 and VCrGO@Si-2 based on the amount of PS from low to high. As a control group, VCrGO was prepared using the same procedure but only mixing GO sheets with PS NPs as the initial feeding dispersion for spray drying, where the mass ratio of GO/PS is same with that of VCrGO@Si-1. The sample before heat treatment is denoted as CGO@Si-X, where X=0, 0.5, 1 and 2. When necessary, to attain high quality SEM images and eliminate charging of the non-conductive CGO@Si material, partial reduction under 250°C for 2 hours with a ramping rate of 1°C/min in Ar/H_2 was carried out.

4.1.4 Materials Characterization

Scanning electron microscope (SEM) images were taken on a field emission scanning electron microscope (Zeiss LEO1550) with an acceleration voltage of 10 kV. Thermogravimetric analysis (TGA, Q500- TA Instruments) was performed by heating the sample under air or nitrogen flow from room temperature to 650°C at a rate of 5°C/min. Transmission electron microscope (TEM) images were taken on an energy-filtered transmission electron microscope (Zeiss Libra 200MC) with an acceleration voltage of 200 kV.

The size distributions of polystyrene nanospheres were obtained by counting at least 200 particles in TEM images. A CMOS detector for electron energy loss spectroscopy (EELS) integrated into the TEM was used for elemental mapping. Hydrodynamic radii were determined by dynamic light scattering (DLS, Zetasizer Nano-ZS90, Malvern). The density of PS and Si NPs was calculated based on the volume measured by a gas pycnometer (AccuPyc II, micromeritics) using helium gas. X-ray photoelectron spectroscopy (Thermal Scientific K-Alpha XPS spectrometer, 150 eV) was carried out to analyze surface elemental composition and chemical bonds. X-ray diffraction (XRD) was carried out using an XRG 3000 X-ray diffractometer (Cu Kα radiation). FEI Titan 80-300 LB was used to obtain the high-resolution TEM (HRTEM) image of VCrGO@Si-1. The pore size distributions of various samples were measured by a dynamic vapor sorption instrument (DVS, Surface Measurement Systems) and the corresponding specific surface area was calculated based on Brunauer–Emmett–Teller (BET) theory.

4.1.5 Electrochemical Characterization

Electrodes were cast by mixing active material (Si + rGO), carbon black (MTI Corp., TIMCAL Graphite and Carbon Super P® Conductive Carbon Black) and sodium alginate (Sigma Aldrich) in DI water with a mass ratio of 65:20:15 using a rotor/stator homogenizer. The resulting slurry was cast onto copper foil by a typical film casting doctor blade method and then was dried at 80°C under vacuum overnight. The mass loading of active material (Si + rGO) was adjusted to around 1 mg/cm^2 for all electrochemical measurements except for Figure 4.13a (where the mass loading was increased to 2.4 mg/cm^2). Coin-type half cells

were assembled with lithium metal foil (Sigma Aldrich, 99.9% trace metal basis) in an Ar-filled glove box (< 1 ppm O_2 and water). A Whatman glass microfiber (Grade GF/A) was used as a separator, and 1 M $LiPF_6$ in a 1:1 v/v mixture of ethylene carbonate (EC) and dimethyl carbonate (DMC) containing 5 vol.% FEC purchased from Canrd China was used as electrolyte. For the coin-type full cell fabrication, VCrGO@Si-1 was first lithiated to 0.01 V at 0.1 A/g in a half cell and then immediately coupled with $LiFePO_4$ cathode (LFP) using the same fabrication procedure. The LFP cathode (~ 12 mg/cm^2 in terms of the weight of LFP) was prepared by mixing commercial LFP powder (Gelon Chemical), polyvinylidene difluoride (PVDF, Kynar® HSV 900 Arkema) and carbon black with a mass ratio of 8:1:1 in N-methyl-2-pyrrolidone (NMP) and then cast as the electrode using the same procedure as for the anode materials. To match with the LFP cathode (~1.62 mAh/cm^2 at 1.14 mA/cm^2 (0.5C) in half cells) at the N/P ratio of ~1.1, the active material mass loading (Si + rGO) of VCrGO@Si-1 is determined to be ~1.5 mg/cm^2 (~1.79 mAh/cm^2 at 1.14 mA/cm^2 in half cells). All cells were cycled in the voltage range of 0.01 V - 1.5 V for half cells and 2 V – 3.9 V for full cells using a LANHE multi-channel battery tester (Wuhan LAND Electronics Co.). Electrochemical impedance spectroscopy (EIS) was carried out on a SP-300 potentiostat (BioLogic) in the range of 1 MHz to 100 mHz with an AC amplitude of 10 mV. Nyquist plots were recorded after the first full cycle (after one discharge and one charge at 0.1 A/g) or after 200 cycles at 1 A/g. The electrodes were charged (delithiated) to 1.5 V, disconnected from the battery tester and connected to the potentiostat where the OCV was around 1.2 V for each sample. EIS was then carried out at this DC voltage vs. lithium metal.

4.2 Results and Discussion

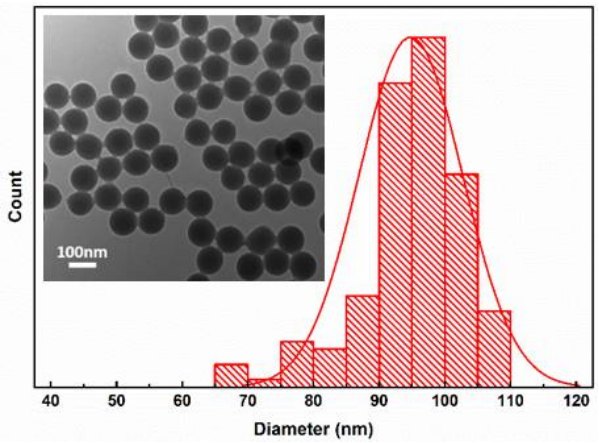

Figure 4.2 size distribution of PS nanospheres by counting 200 particles in TEM images (inset).

As shown in **Figure 4.2**, the average diameter of PS NPs prepared is approximately 95 ± 8 nm, which is comparable to the size of commercial Si NPs (~100 nm). The hydrodynamic diameter of PS NPs, Si NPs and GO sheets was also estimated by dynamic light scattering (DLS in **Figure 4.3a**) which indicated average diameters of ~101 nm, ~89 nm and ~1022 nm, respectively, in the same liquid system (ethanol/water mixture with a volume ratio of 1:4). The similar sizes of the PS NPs and Si NPs suggest that the two particles will have a similar diffusivity, which is significantly higher than that of the GO sheets. This is important in designing the core-shell structure where it is known that larger GO sheets will mostly accumulate at the droplet interface during drying while the smaller NPs are able to redistribute while the aerosol dries and forms the core.[89, 98, 101] Moreover, The convection induced during the drying process may also pin the GO at the interface where it acts to lower the surface energy.[101] This process is summarized in **Figure 4.1**.

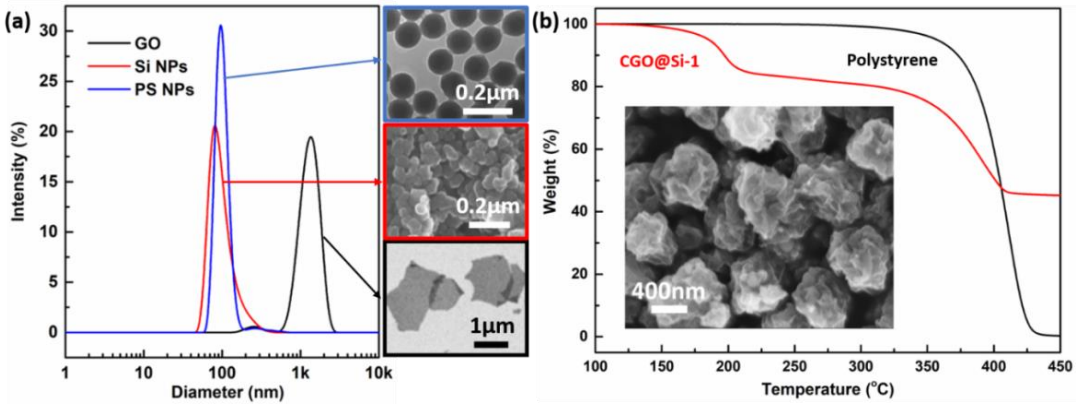

Figure 4.3 (a) Distribution of hydrodynamic diameter as estimated by DLS for GO, Si NPs and PS NPs. Corresponding TEM image for PS and SEM images of Si and GO are shown as inset. (b) TGA profiles for pure PS and CGO@Si-1 conducted under N_2 flow and SEM image (inset) of CGO@Si-1 which was partially reduced at 250 ℃ to render the sample conductive for easier imaging.

A scanning electron microscope (SEM) image of the VCrGO@Si-1 before removing PS template (CGO@Si-1) is shown in **Figure 4.3b** inset. All composite particles display a similar crumpled structure to what has previously been reported for neat and cargo-filled GO.[98] The lack of any obvious PS or Si on the outside of the crumpled GO, indicates that most of the NPs were successfully encapsulated within the CGO framework. Thermogravimetric analysis (TGA) was carried out on both the PS NPs and CGO@Si-1 under nitrogen flow as shown in **Figure 4.3b** in order to mimic the thermal reduction procedure under inert conditions (where the corresponding derivative curves are shown in **Figure 4.4a**). The PS NPs slowly degrade starting around 300°C and are completely decomposed beyond ~430°C. For CGO@Si-1 samples, an earlier mass loss is observed between 150°C and 225°C which is attributed to the thermal reduction of GO with a more significant mass loss observed at higher temperatures corresponding to the PS decomposition. As a control group, TGA was

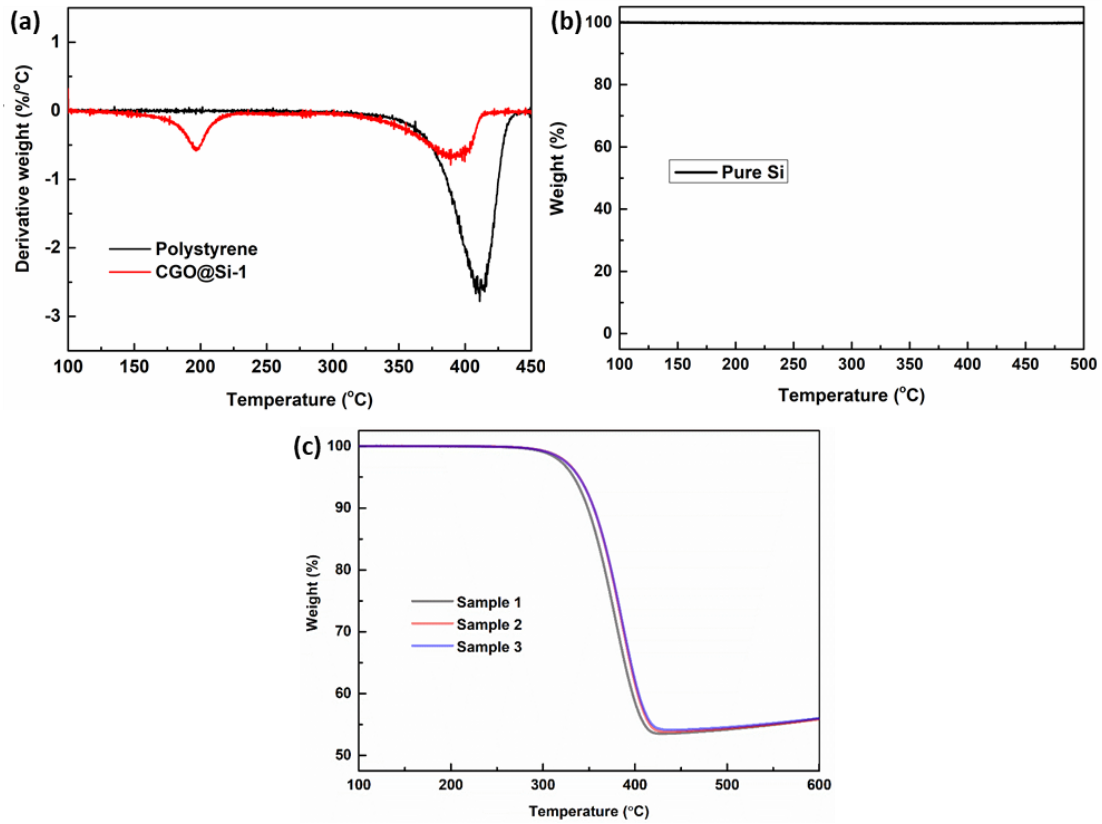

Figure 4.4 (a) TGA derivative curves of polystyrene and CGO@Si-1, TGA curves of (b) pure Si and (c) PS/Si spray dried from 3 batches of feeding solution containing PS NPs and Si NPs with a designed mass ratio of 1:1 under N_2 protection.

carried out on pure Si NPs under similar conditions (**Figure 4.4b**). There was no significant mass loss under nitrogen protection. Pure PS/Si mixtures made by spray drying (without GO) with a mass ratio of 1:1 from three separate batches were also analyzed by TGA and found to contain 53.0 ± 0.3wt% (error estimated as the standard deviation) of silicon as shown in **Figure 4.4c**. The slight deviation from the designed 1:1 mass ratio is attributed to experimental error and the slight oxidation of Si NPs beyond 400°C which is apparent in the TGA curves (Figure S2d) as a mass increase between 400 °C and 600 °C.

Transmission electron microscope (TEM) images for the high temperature annealed VCrGO@Si material are provided in **Figure 4.5a** for varying initial PS/Si ratios. Under TEM,

rGO is relatively transparent due to its atomically-thin nature and low atomic number. Thus, regions with brighter contrast indicate empty space where the electron-beam is not blocked by the dense silicon particles. It is clear from **Figure 4.5a**, that there is a transition from a dense core to one that becomes more transparent to the electron beam as the proportion of void space is increased. The inner structure of VCrGO@Si-1 was better revealed using high-resolution TEM (HRTEM) imaging. Images for a single composite ball at varying magnifications are shown in **Figure 4.5b**. Relatively low magnification images reveal spatially separated Si NPs. At higher magnification, it becomes clear that crystalline Si NPs (d=0.31 nm as indicated by white arrows, which belongs to Si (111)) are completely encapsulated by a layer of carbon which is attributed to multilayered crumpled rGO sheets with a thickness of around 15 nm in the region labeled by white dashed lines. The spatial distribution is better revealed by the electron energy loss spectroscopy (EELS) mapping as shown in **Figure 4.5c**. As expected, the carbon signal is generated from the entire structure while a faint signature of oxygen and a stronger signal for silicon reveal the inner structure of silicon within the core, suggesting that void space is successfully created. Si NPs do not appear to aggregate significantly within the VCrGO capsule after the PS template is removed.

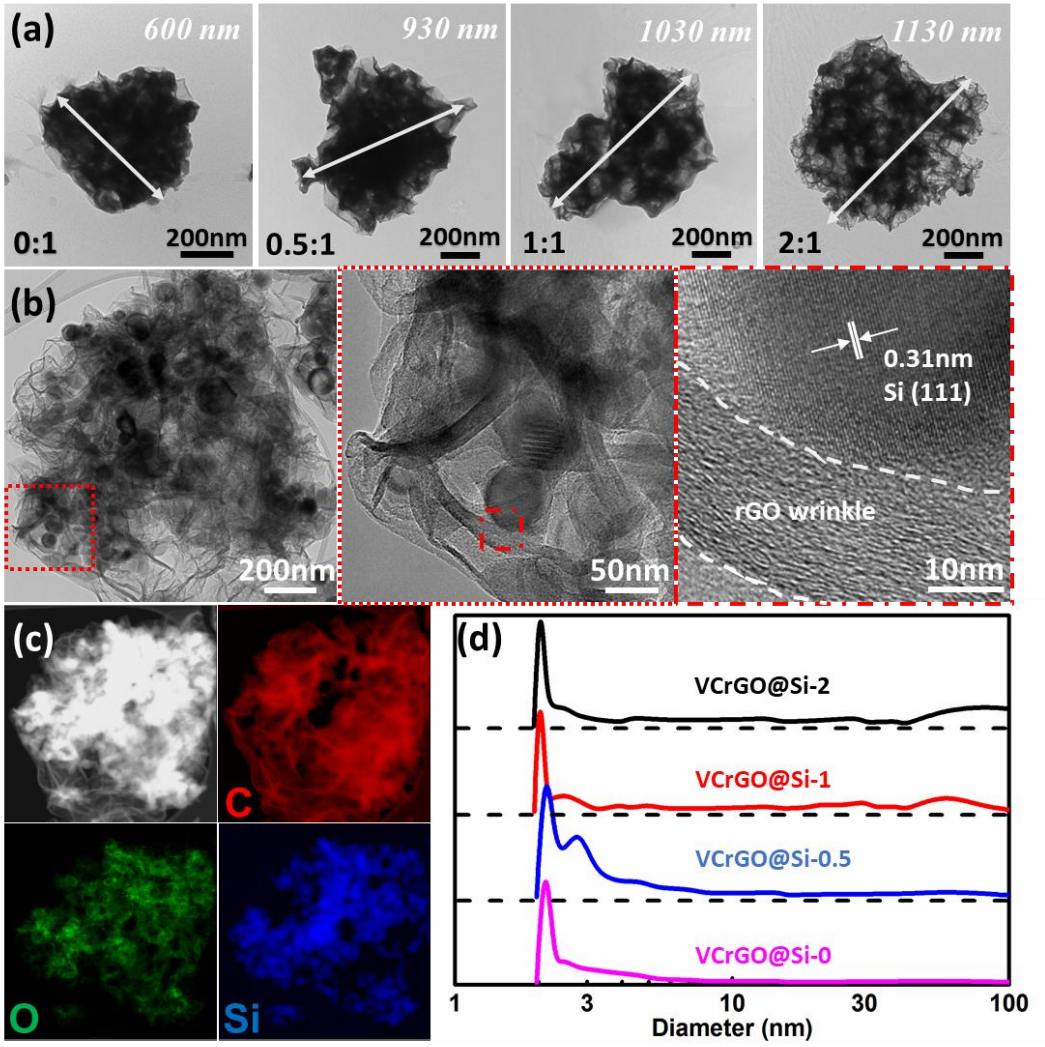

Figure 4.5 (a) TEM images of VCrGO@Si prepared using varying mass ratio of PS/Si, (b) HRTEM images of VCrGO@Si-1 at varying magnifications, (c) EELS elemental mapping of VCrGO@Si-1 for carbon, oxygen and silicon respectively and (d) pore size distributions of VCrGO@Si prepared using varying mass ratio of PS/Si.

The pore size distributions of VCrGO@Si with varying PS/Si ratios were determined by dynamic vapor sorption (DVS) using cyclohexane as the organic adsorbent and plotted in **Figure 4.5d**. Without the addition of PS, VCrGO@Si only exhibited one sharp peak at ~2 nm with a broad shoulder extending to ~5 nm, which includes the voids created by partially restacked rGO in the shell and voids between inter-particle and particle-rGO contacts. The small pore size suggests that Si NPs are compressed tightly and wrapped by rGO due to the

strong capillary forces known to be generated during the rapid drying of the aerosol.[90, 98] After the addition of PS with a mass ratio of 0.5:1 PS to Si, a shoulder, now at ~3 nm is significantly larger. This may be attributed to the thermal decomposition and evaporation of PS during the heat treatment. The vapor generated likely led to some expansion between the Si NPs themselves or Si NPs and inner rGO framework. Additionally, a broad hump can be observed in the range of ~40-90 nm which is attributed to the void space created by the removal of the PS NPs. With the increased amount of sacrificial PS, more void space was introduced inside which resulted in the emergence of higher intensity peaks in this region which gradually broadened and shifted towards larger sizes. The SSA was estimated based on BET theory, which was found to be 41.9 m^2/g, 35.9 m^2/g, 34.7 m^2/g and 36.8 m^2/g for VCrGO@Si-0, VCrGO@Si-0.5, VCrGO@Si-1 and VCrGO@Si-2, respectively. Since the removal of PS was conducted at a very slow heating rate (1°C/min) and long isothermal time (2 hours) at 450°C, the decomposition rate of PS is likely low and should not significantly impact the structure of the CrGO framework resulting in only minute changes in SSA. In contrast, the specific pore volume increased with the addition of PS NPs: 0.04 cm^3/g, 0.11 cm^3/g, 0.25 cm^3/g and 0.36 cm^3/g for VCrGO@Si-0, VCrGO@Si-0.5, VCrGO@Si-1 and VCrGO@Si-2, respectively. It must be noted that the emergence of macropores (diameter > 50 nm) and pores with complex shapes might cause the measured results to be less than the actual pore volume, especially when using larger content of PS NPs. To approximate the void space introduced, the density of the as-prepared polystyrene nanospheres was determined by pycnometer using helium gas to be ~1.06 g/cm^3. This is around half of the density of Si nanoparticles (~2.27 g/cm^3). Based on the PS/Si mass ratio designed for VCrGO@Si-0,

VCrGO@Si-0.5, VCrGO@Si-1 and VCrGO@Si-2, the theoretical void space created by burning off the polystyrene template to buffer the volume expansion of silicon is estimated to be 0%, 107.1% (~100%), 214.2% (~200%) and 428.3% (~400%), respectively.

X-ray photoelectron spectroscopy (XPS) was carried out to analyze the surface elemental composition for pure CGO@Si-1, CrGO@Si-1 and pure PS NPs as shown in **Figure 4.6a**. Both

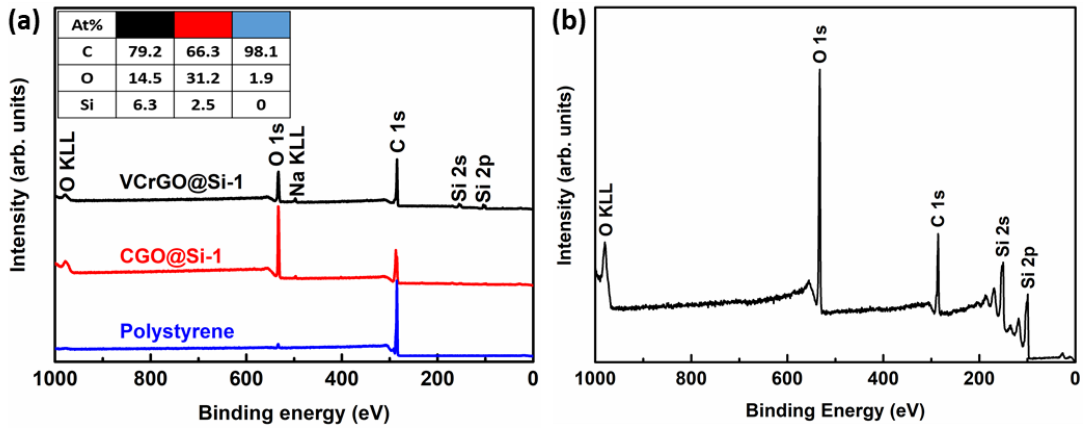

Figure 4.6 XPS survey of (a) varying samples and (b) pure silicon nanoparticles.

the carbon 1s peak (at ~284 eV) and oxygen 1s peak (at ~532 eV) are present at the surface of all samples. Only two low intensity peaks belonging to Si 2s (at ~149 eV) and Si 2p (at ~99 eV) arise from the inside of the structure despite their composition being 28.9at% and 37.1at% in the bulk in both CGO@Si-1 and VCrGO@Si-1. This is due to the low penetration depth (~10 nm) intrinsic to XPS which limits analysis to the surface of the crumpled structure. PS is theoretically composed of aromatic and aliphatic carbon as well as hydrogen,[116] the 1.9 at% of oxygen presented in the measurement should be attributed to the impurities introduced during the sample preparation. CGO@Si-1 only contains 2.5 at% of silicon which is much lower than that at the surface of pure silicon (47.5 at% as shown in **Figure 4.6b**) and its C/O (~2.13) is consistent with well-oxidized GO (~2.15) which was produced by the same

method as shown in our previous work.[117] These results provide further evidence that most PS and Si NPs are successfully encapsulated and since the XPS signal is dominated by the signature of the crumpled GO shell. The Si content increased to 6.3 at% after the reduction of GO and removal of PS. To better understand the surface chemical composition, the C 1s narrow scan spectra was examined for pure PS, CGO@Si-1, and the annealed VCrGO@Si-1.

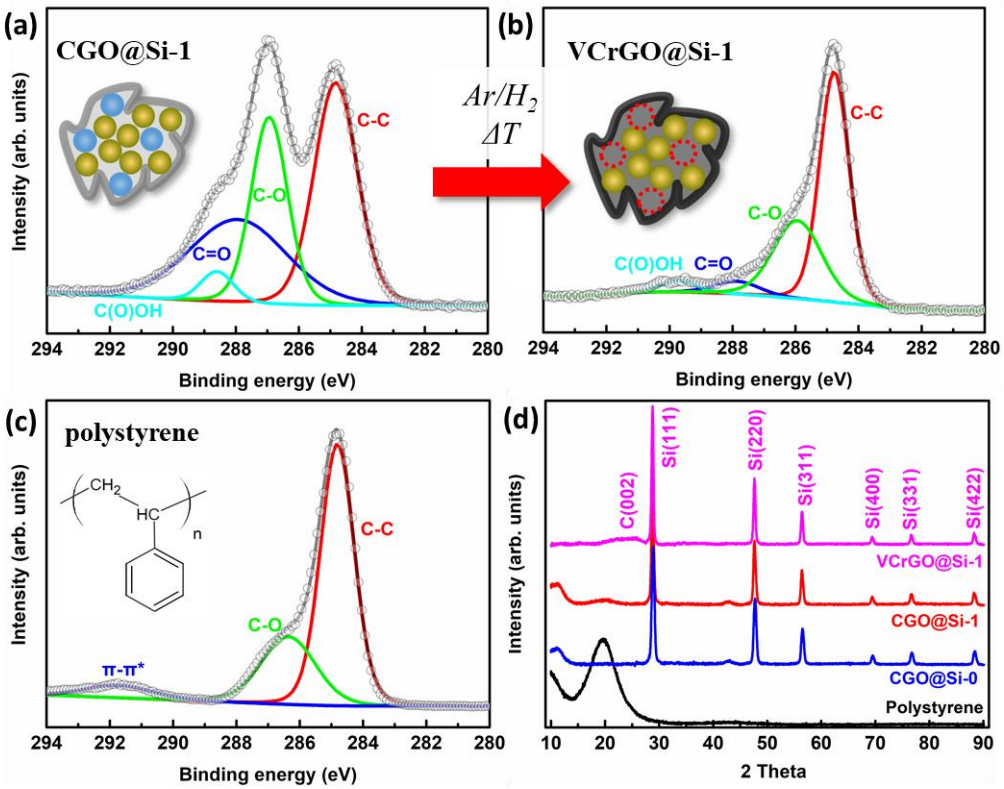

Figure 4.7 high-resolution XPS narrow scan spectra of CGO@Si-1 (a), VCrGO@Si-1 (b) and pure PS (c) for their C 1s peaks, (d) XRD patterns of varying samples.

The C 1s spectra of CGO@Si-1 (**Figure 4.7a**) and the annealed VCrGO@Si-1 (**Figure 4.7b**) can be deconvoluted into four peaks at around 284.8 eV, 286.9 eV, 287.9 eV, and 288.8 eV, which belong to C-C bonds, C-O bonds, C=O bonds, and C(O)OH bonds, respectively.[118] After thermal reduction, the amount of all oxygen-containing functional groups decreased, particularly the C=O and C-O bond. As this is a surface-sensitive technique, this is indicative

of graphene oxide (GO) transformation into reduced graphene oxide (rGO). As depicted in **Figure 4.7c**, the C 1s peak of pure PS can be deconvoluted into 3 peaks. The main peak at 284.8 eV includes the aliphatic and aromatic carbon bond while the small shoulder at 286.36 eV indicates C-O-C or C-OH groups coming from surface impurities. The satellite peak at 292 eV is attributed to a shake-up structure originating from $\pi \rightarrow \pi^*$ excitations in the aromatic ring structures.[116, 119] X-ray diffraction (XRD) profiles for pure PS, CGO@Si-0, CGO@Si-1 and CrGO@Si-1 are plotted in **Figure 4.7d**, the sharp and intense peaks presented at 28.4°, 47.3°, 56.1° and 69.1° in all XRD patterns except for pure PS were assigned to (111), (220), (311) and (400) lattice planes of crystalline silicon.[120] The large and broad peak at 2θ ~15°-23° in the XRD pattern of pure PS indicates its amorphous structure. This peak emerged in the XRD pattern of CGO@Si-1 suggesting the successful introduction of PS NPs within the spray dried crumpled structure. After being thermally annealed from CGO@Si-1 to VCrGO@Si-1, this broad peak disappeared while a broad and nearly indiscernible peak emerged at around 2θ ~20°-27° attributed to the characteristic (002) carbon peak indicating that PS NPs were removed and the rGO shell is nearly X-ray amorphous.

The electrochemical performance of each of the materials containing different amounts of void space were then tested as the active material for battery electrodes using half-cells cycled against lithium metal. The rate performance was tested by progressively increasing charging rates between 0.1-4 A/g (~C/20-2C). As shown in **Figure 4.8a**, VCrGO@Si-1 displayed the best performance, achieving 1638 mAh/(g_{Si+rGO}) at 0.1 A/g and retaining 1179 mAh/(g_{Si+rGO}) at 4 A/g with a capacity retention of 71.9%. For the VCrGO@Si-0 sample (no PS template), the capacity at 1 A/g was similar but dropped considerably at 4 A/g while

VCrGO@Si-0.5 can still maintain 63.2% of capacity, suggesting that the PS addition had a significant and beneficial impact on the high rate performance. However, for the sample with 400% void space (VCrGO@Si-2), the rate performance was not as good at 4 A/g, delivering only 61.7% of the capacity achieved at 0.1 A/g. This indicates that excess void space may reduce the number of effective electrical and/or ionic (for Li^+ ions) contacts between the Si particles and the shell. The Nyquist plots are presented in **Figure 4.8b** for all four samples. They exhibit a semi-circle in the high frequency region and a straight line in the low frequency region, which are attributed to charge transfer resistance (R_{ct}) and Warburg diffusion process (Z_w), respectively. The slope of all straight lines at the low frequency region is obviously larger than 45° suggesting a deviation from ideal semi-infinite diffusion condition, which might be attributed to the short solid-state diffusion lengths in

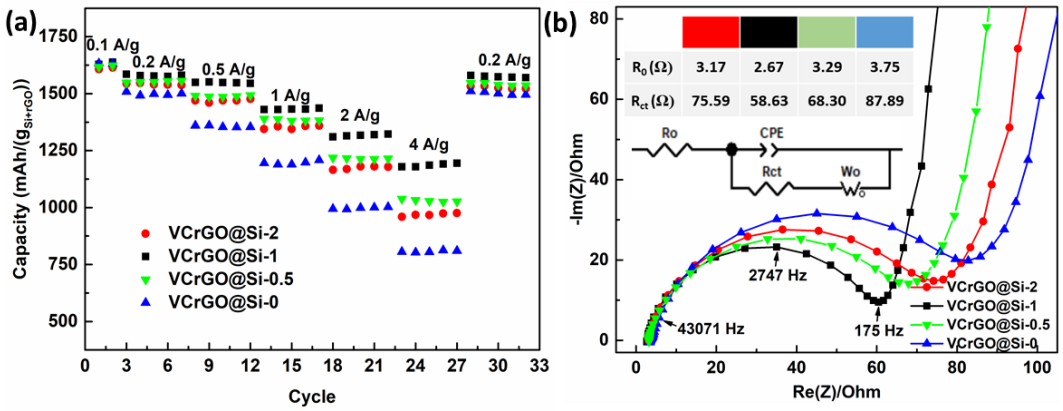

Figure 4.8 (a) Electrode capacity at various current desities, (b) Impedance Nyquist plots of varying samples after 1st cycle and equivalent circuit (inset)

small Si NPs and additional capacitive behavior caused by the complex porous structure of the VCrGO framework.[121, 122] The smallest semicircle in the curve of VCrGO@Si-1 indicates it has the lowest charge transfer resistance (58.6 Ω), leading to lower internal resistance when

compared to VCrGO@Si-0 (87.9 Ω). The improvement in both rate capability and charge transfer resistance may be attributed to an improved radial distribution of GO within the microdroplet driven by the addition of PS during the spray drying as shown in **Figure 4.9**. As discussed earlier, as water evaporates from the aerosol droplet in the step1 (① to ② in **Figure 4.1**), the GO sheets may become trapped at the air-water interface while NPs attempt to maintain a uniform concentration. The initial size of the microdroplet should remain constant under the same spray drying parameters as the droplet size is controlled by the flow rate of carrier gas in the two fluid nozzle as well as the liquid viscosity and surface tension – which do not change significantly upon addition of the PS NPs.The presence of

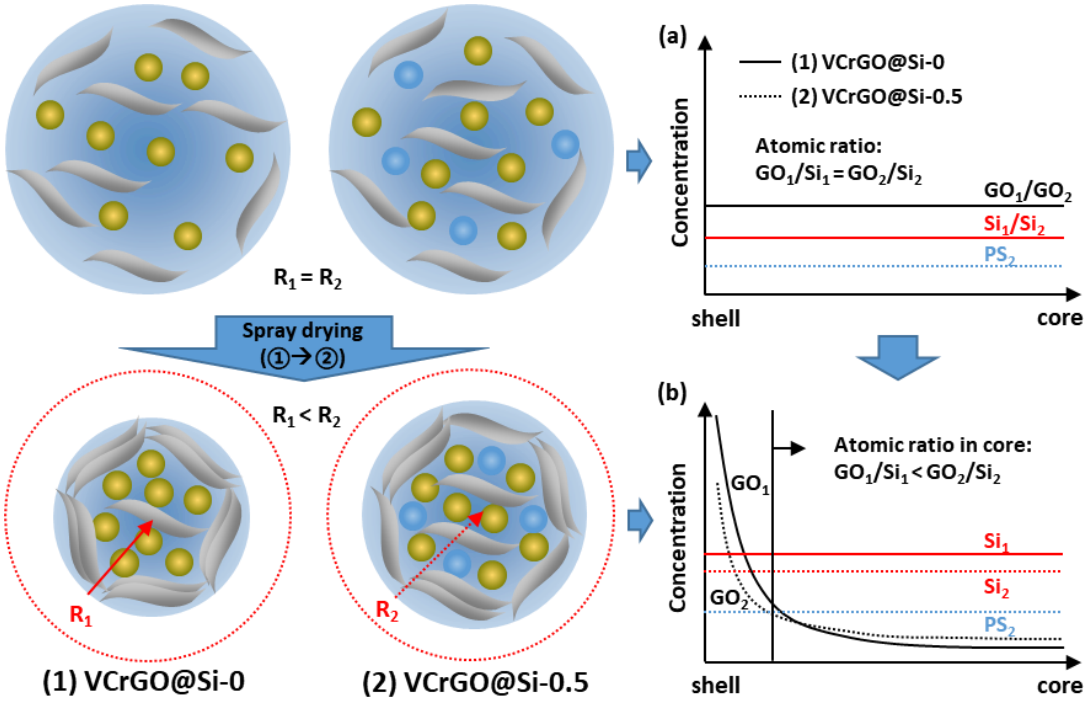

Figure 4.9 Schematic illustration of improved conductive network: radial spray drying components concentration distributions of VCrGO@Si-0 (1) and VCrGO@Si-1 (2) at stage① (a) and stage② (b).

more material within the core (the additional PS NPs) could prevent some of the GO from reaching the interface, causing some material to be trapped in the core. The hypothesized

radial distributions of each component for VCrGO@Si-0 and VCrGO@Si-0.5 before and after step1 are shown in **Figure 4.9a** and **4.9b** respectively, suggesting VCrGO@Si-0.5 theoretically has a larger GO/Si ratio in the core region compared to the sample without PS. As silicon is a poorer electronic and lithium ion conductor, after heat treatment, contacting the rGO instead of another Si NP would improve the overall conductivity. We also surmise that the void space, introduced via PS removal, is able to effectively buffer the volume expansion of silicon and maintain a good conductive network during charge/discharge. On the other hand, excess void space made the charge and/or ion transfer route too long, resulting in a larger R_{ct} (75.6 Ω) of VCrGO@Si-2. The similar effect of void space on electrochemical performance was observed by Guo et al. for a conformal carbon coated silicon anode, where excess void space led to poorer electrode performance.[123] The voltage profiles in terms of specific capacity of VCrGO@Si-1 are plotted in **Figure 4.10a**, showing a typical shape for lithiation (discharge) and de-lithiation (charge) process of silicon at 0.2 A/g with the plateaus at ~ 0.3 V - 0.01 V and ~ 0.2 V - 0.6 V, respectively.[55] With the increasing current density from 0.2 A/g to 4 A/g, the polarization of Si led to an apparent increase in the de-lithiation potential and reduction of the lithiation potential.

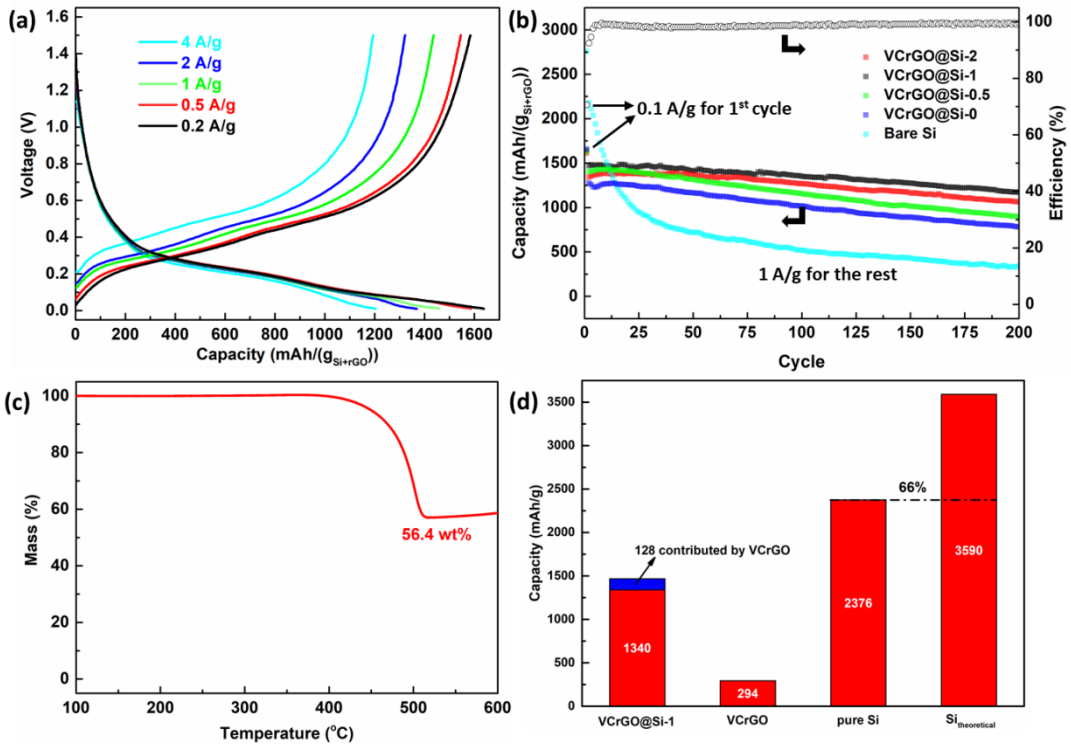

Figure 4.10 (a) Charge/discharge curves for VCrGO@Si-1 at varying current densities, (b) cyclic stability of varying samples, (c) TGA under air low of VcrGO@Si-1 and (d) analysis of the capacity contribution of VCrGO@Si-1.

The cycle-life of all samples was investigated by applying a 0.1 A/g current for the 1st cycle and a 1 A/g current for the following 200 cycles, which were plotted in **Figure 4.10b**. VCrGO@Si-1 displayed the best cyclic stability, which only dropped from 1468 mAh/(g $_{Si+rGO}$) to 1183 mAh/(g $_{Si+rGO}$) with a capacity retention of 80.6% compared to that of VCrGO@Si -0 (61.3%) and VCrGO@Si -2 (79.5%). VCrGO@Si-1 also displayed an improved columbic efficiency (70.6%) of the 1st cycle which is much higher than that of pure silicon (57.2%), suggesting that the crumpled rGO shell with mesopores can partially prevent Si NPs from directly being exposed to electrolyte. In addition, the cycle life of VCrGO@Si-0.5 is also plotted for comparison, which only displayed a minor improvement in capacity retention (64.2%) after 200 cycles. Based on the above experimental facts, we conclude that

VCrGO@Si with a mass ratio of PS/Si at 1:1 possesses the most appropriate void space to buffer the volume expansion of Si during cycling. According to the TGA result (**Figure 4.10c**), the content of rGO in VCrGO@Si-1 is around 43.6 wt%. As shown in **Figure 4.10d**, since pure VCrGO can provide a capacity of ~294 mAh/(g_{rGO}) at 1 A/g, the capacity per gram of VCrGO@Si-1 contributed from Si core is around 1340 mAh at 1 A/g (the real specific capacity of Si core is ~2376 mAh/(g_{Si})). In theory, the pure silicon anode can display a theoretical capacity of 3590 mAh/g with a volume expansion of ~300% at room temperature.[56, 124] Considering only ~66% of theoretical capacity is displayed, the average real volume expansion can be assumed as ~198%. As we discussed before, VCrGO@Si with a mass ratio of PS/Si at 1:1 can theoretically create a void space to buffer ~200% volume expansion. This designed theoretical value of VCrGO@Si-1 is just above the estimated volume expansion of the Si core at 1 A/g, which explains the reason why VCrGO@Si-1 displayed the best electrochemical performance. As shown in **Figure 4.11a**, the density of VCrGO@Si should decrease with the increasing amount of sacrificial PS template. The density is estimated to 1.5 g/cm^3, 1.28 g/cm^3, 1.13 g/cm^3 and 0.91 g/cm^3 for VCrGO@Si-0, VCrGO@Si-0.5, VCrGO@Si-1 and VCrGO@Si-2, respectively. To compare these four samples in a fairer way, their capacities were also converted into a volumetric capacity as shown in **Figure 4.11b**. Even with a lower electrode density, VCrGO@Si-1 still displayed the best volumetric capacity of 1337 mAh/cm^3 at 1 A/g after 200 cycles, which is around 75.33% of the theoretical volumetric capacity for this composite (1774 mAh/cm^3) estimated by excluding the volume of extra void space (i.e. using the density of VCrGO@Si-0).

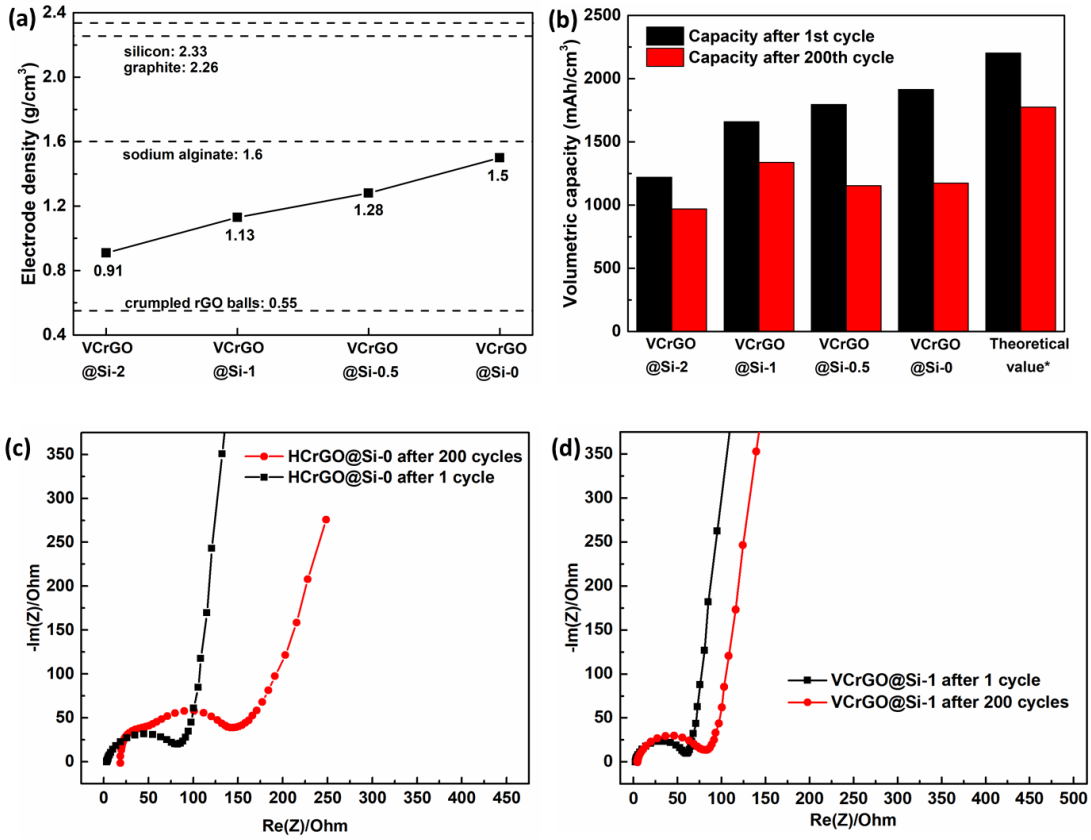

Figure 4.11 (a) Electrode densities of varying samples, (b) volumetric capacities of varying samples before and after cycling, Nyquist plots of VCrGO@Si-0(c) and VCrGO@Si-1(d) after 1st cycle and 200 cycles.

The EIS results were recorded for VCrGO@Si-1 after the 1st cycle and the 200th cycle and plotted in **Figure 4.11c**. The Nyquist plots maintain a similar shape and only a small expansion is observed for the semi-circle in the high frequency region, while obvious growth in both ohmic resistance (R_o) and R_{ct} can be observed for VCrGO@Si-0 (**Figure 4.11d**), suggesting the void space reserved crumpled rGO shell can help silicon based anodes maintain a good electrochemical structure after long--term cycling. For VCrGO@Si-0, after 200 cycles, the emergence of an additional semicircle at lower frequencies may indicate resistance through a thicker SEI that has developed as a result of cycling due to the absence of enough void space in this sample.[125] In addition, SEM images of VCrGO@Si-1 before and after cycling were taken as shown in **Figure 4.12**, no significant cracks were observed and

still the crumpled core-shell structure was maintained, suggesting most of the volume expansion of Si is buffered in the rGO shell. To better confirm the improvement of Si anodes

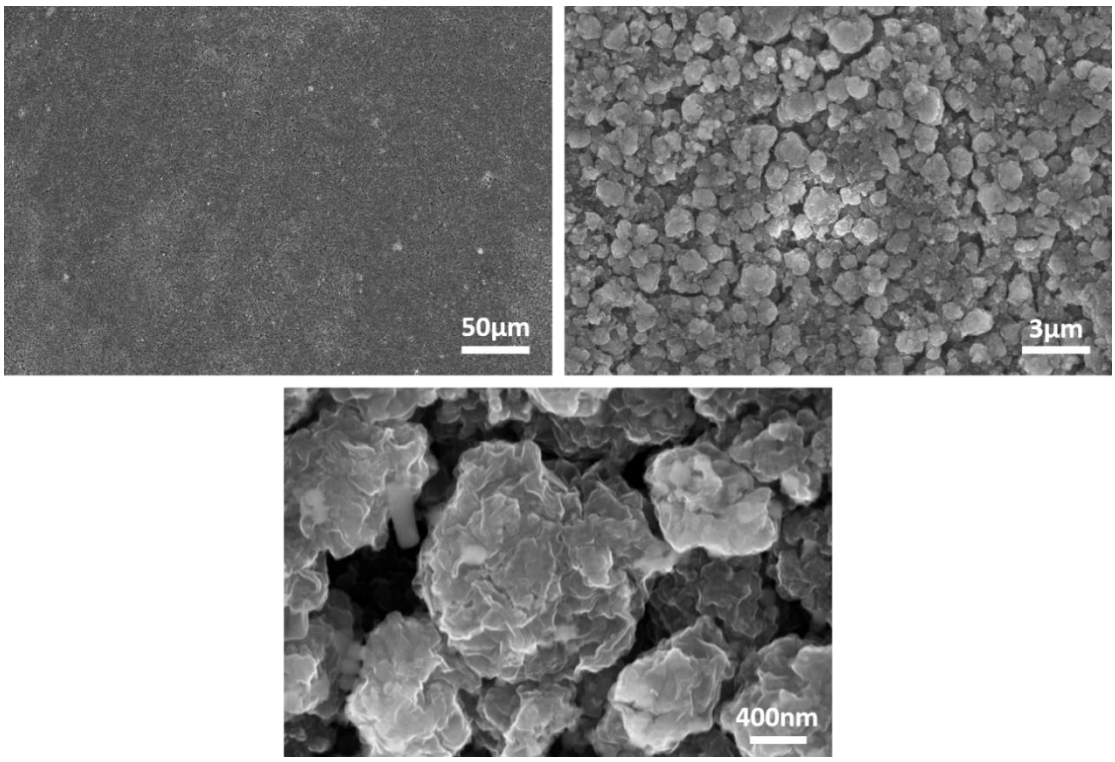

Figure 4.12 SEM images of VCrGO@Si-1 after 200 cycles at varying magnifications

using our VCrGO protective layer, we increase the mass loading of active materials (Si + rGO) from 1 mg/cm^2 to 2.4 mg/cm^2. With such a high loading, VCrGO@Si-1 displays an initially high areal capacity of 2.26 mAh/cm^2 which maintains > 80% of capacity after 145 cycles as shown in **Figure 4.13a**. To compare with other works in literature based on similar methods of creating void space to buffer volume expansion of Si/C anodes, their main electrochemical performance has been summarized in **Figure 4.13b**. Our material exhibits competitive cycle life and areal mass loading with a relatively simple preparation method among all these works. For electrodes meeting the following conditions: (1) capacity retention ≥ 90% after 100 cycles and (2) mass loading ≥ 1 mg/cm^2, their capacity at varying current densities are

recorded in **Figure 4.13c**, suggesting our material also displayed an outstanding rate capability compared to other similar works.

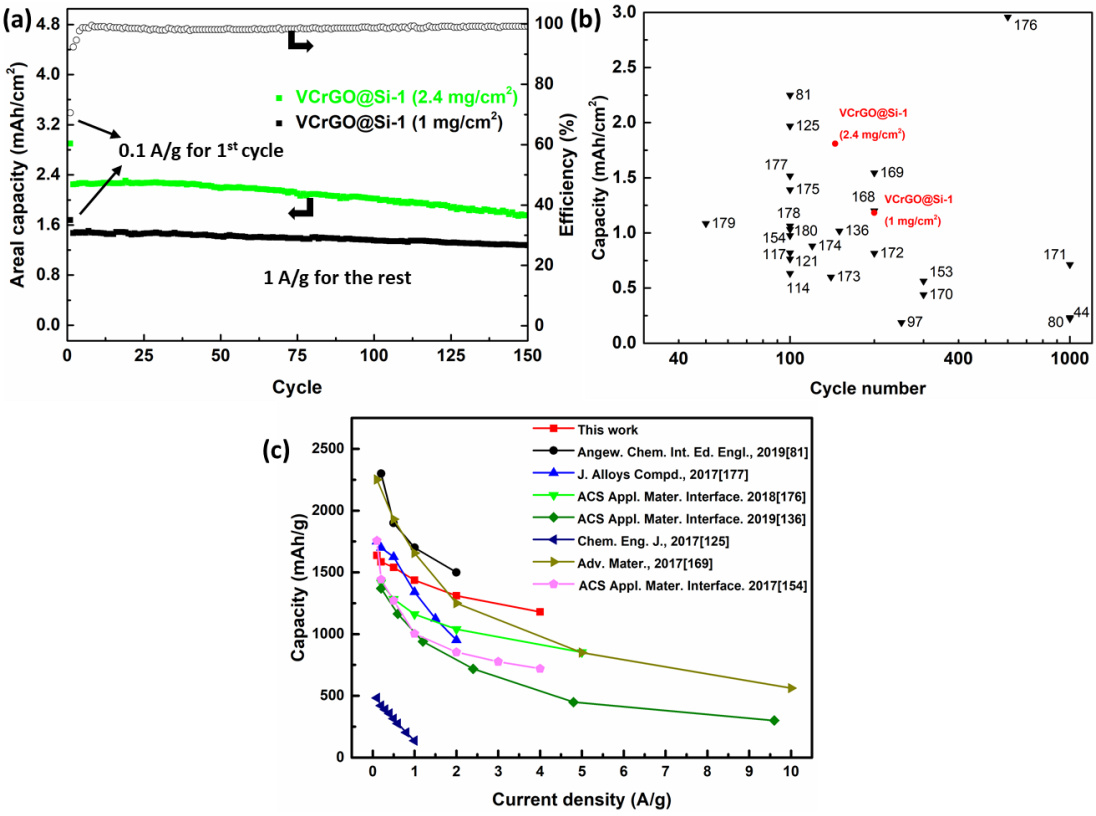

Figure 4.13 (a) Cyclic stability of VCrGO@Si-1 at increased mass loading, (b) capacity retention of recent works about Si/C based composites with artificially or naturally reserved void space[44, 80, 81, 98, 112, 123, 126-143] and (c) comparison of rate capability for varying Si/C based anodes with void space.

To evaluate the feasibility of our material being used in a full-cell lithium-ion battery, VCrGO@Si-1 was coupled with a LiFePO4 cathode (LFP) with the capacity ratio between negative electrode and positive electrode (N/P) of ~1.1. The voltage profiles at different cycling stages are illustrated in **Figure 4.14a**, the VCrGO@Si-1//LFP full cell exhibited a slightly slanting discharge plateau in the range of ~ 3.35 V – 2.85 V (which is consistent with the voltage difference between the charge plateaus of VCrGO@Si-1 and the discharge plateau of LFP in half cells) with minimal polarization after 100 cycles. As shown in **Figure**

4.14b, this full cell maintains 91.4% of its initial capacity (~109 mAh/(g LFP)) after 100 cycles at 0.5C (~0.76 A/g in terms of the mass of VCrGO@Si-1) despite the LFP cathode not providing a significant excess of Li+ ions as is the case when lithium foil is used in half cells.

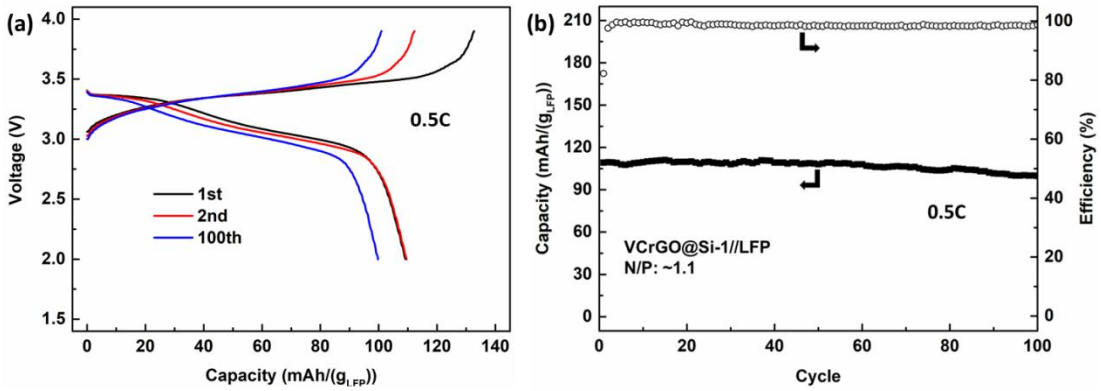

Figure 4.14 Characterization of full cell using VCrGO@Si-1 as anode and LFP as cathode: (a) voltage profiles and (b) cyclic stability performance at 0.5C for 100 cycles.

4.3 Conclusions

In summary, polystyrene nanospheres were synthesized by a simple emulsion polymerization with a diameter of 85 ± 8 nm and used as sacrificial material which can be thermally removed at 450°C in inert gas atmosphere. Then, PS NPs were spray dried together with Si NPs and GO sheets, followed by the reduction of GO and the removal of PS in tube furnace. The mass ratio of PS/Si is set as 0:1, 0.5:1, 1:1 and 2:1 for comparison, aiming to buffer the volume expansion of 0%, 100%, 200% and 400% respectively. According to various electrochemical tests, VCrGO with a PS/Si ratio of 1:1 was determined as the optimal composition exhibiting outstanding electrochemical performance in terms of minimizing internal resistance, increasing tolerance to high rate cycling, and maintaining long-term cyclic stability when compared to bare Si or encapsulated Si (with no PS).

VCrGO@Si-1 retained around 80.6% of the initial capacity after 200 cycles while VCrGO@Si-0 only retained 61.3%. At a higher active material loading of 2.4 mg/cm^2, VCrGO@Si-1 displayed a high areal capacity of 2.26 mAh/cm^2 which only dropped by around 20% after 145 cycles. Based on the calculation for the capacity contributed by pure silicon (94.3%) at 1 A/g, the reserved void space of VCrGO@Si-1 can effectively buffer the volume change of Si NPs in the core, without introducing excess volume, improving overall performance. In addition, the simple preparation route using a one-step spray drying encapsulation following the heat treatment also provides the possibility to achieve large-scale commercial production.

5 Controlling Void Space in Crumpled Graphene Using Responsive Hydrogels for stable silicon anodes

This chapter is based on the manuscript which is ready for submission, please see **Statement of Contributions** for details.

In the previous work, polystyrene was used as a template to create void space. However, polystyrene itself connot contribute anything to battery performance. On the contrary, residues due to insufficient heat treatment could significantly cause the decay in electrochemical performance. Hence, in this chapter, we developed a novel method to prepare crumpled rGO encapsulated Si nanoparticles with reserved void space upon the swelling/shrinkage of carboxymethyl cellulose - poly (ethylene oxide) (CMC-PEO) hydrogel. The brief process, depicted in **Figure 5.1**, involves mixing and spray-drying CMC/PEO polymer chains, citric acid, GO sheets, and Si nanoparticles. Upon the distribution difference of varying components during the aerosol evaporation, a quasi-core-shell structure formed (**Figure 5.1b**) where the core is composed of Si NPs, CMC/PEO chains, citric acid, and a small quantity of GO sheets while the shell mainly contains partially restacked crumpled GO sheets. The resulting composite balls were heated at 80°C to initiate the cross-linking reaction between CMC and PEO where citric acid is used as the cross-linker. The hydrogel containing composite (denoted as GO/Gel/Si) was then immersed in water to make the inside hydrogel fully swell, resulting in increased overall volume, followed by chemical reduction to remove oxygen-containing functional groups from GO and lock its dimension. Finally, the rGO/Gel/Si was slowly dried from water along with the shrinkage of hydrogel, leading to the separation

of Si NPs from the crumpled rGO framework. The reserved void space makes this material displayed an outstanding cycle life, which only drops by ~18.3% of capacity from 1055 mAh/($g_{rGO+Gel+Si}$) at 1 A/g after 320 cycles.

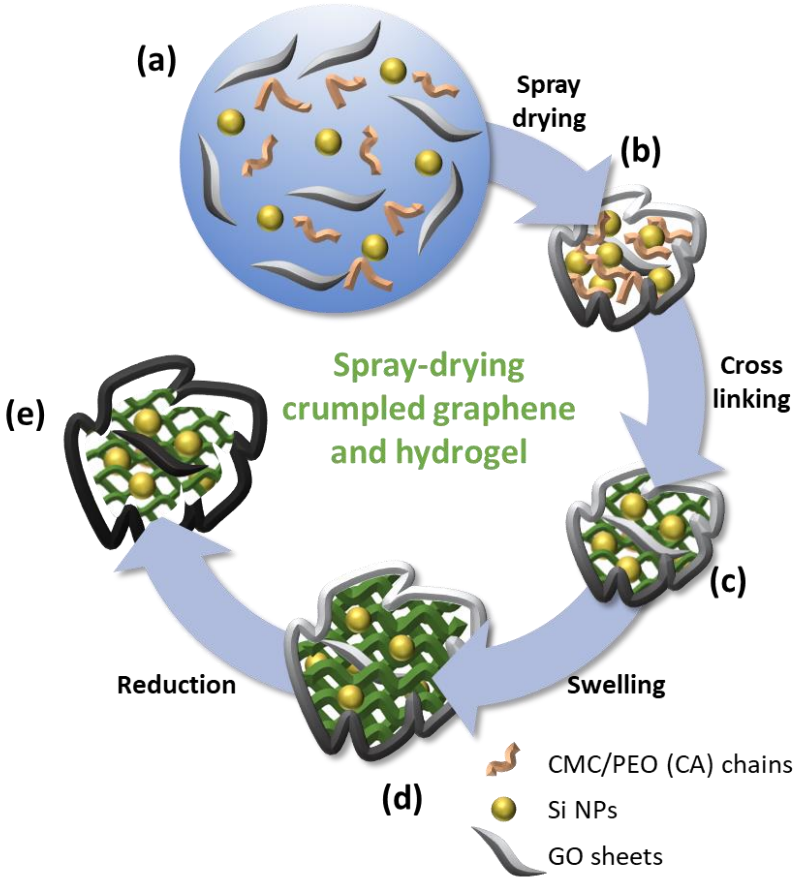

Figure 5.1 Schematic illustration of the synthesis process of rGO/Gel/Si, where the orange region in (b) represents non-cross-linked hydrogel and the green chains in (c-e) represents cross-linked hydrogel.

5.1 Experimental Methods

5.1.1 Synthesis of Graphite Oxide

GO was synthesized using Tour's modified Hummer`s method,[102] which exhibits a C/O is ~2.1 according to the XPS results in our previous work.[117] In a typical preparation process, 3 g of graphite flakes (Alfa Aesar) and 18 g of potassium permanganate ($KMnO_4$) were slowly

added into the acid mixture, which is composed of 360 ml of 98% sulfuric acid (H_2SO_4) and 40 ml of 97% phosphoric acid (H_3PO_4). The oxidation reaction was conducted at 50°C for 16 h under continuous stirring, the resulting thick purple slurry was poured into 400 g of ice when it was cooled down to room temperature. Around 6 ml of hydrogen peroxide (H_2O_2) was then slowly added until the color of the suspension completely turned to a golden or yellow colour. After washing with 10% hydrochloric acid (HCl) and ethanol for three times and four times respectively via centrifugation (3000 rpm, rotor diameter 15 cm), the GO suspension was transferred from ethanol to deionized water (DI water) using a dialysis bag with 12-14 kDa molecular weight cut off (MWCO).

5.1.2 Preparation of Pure CMC/PEO Hydrogel

Sodium CMC and PEO powder (Sigma Aldrich) with a mass ratio of 3:1 were dissolved in DI water with a concentration of 4% (w/v). Then, citric acid with concentrations of 10% and 20% (w/w) compared to CMC/PEO was added into the CMC/PEO homogenous solution and then stirred for 12 h. The resulting thick solution was poured into an aluminum dish (diameter: 6cm) and dried at 40°C for 6h. The dried CMC/PEO hydrogel was punched into discs and cross-linked at 80°C for 6h.

5.1.3 Preparation of Void Space Reserved rGO/Gel/Si

500 mg of GO and 200 mg of amorphous Si NPs (~ 50 - 100 nm, Strem) were mixed in 1000 ml of DI water during water bath ultrasonication. CMC/PEO (3:1 by mass) was dissolved in GO/Si dispersion with a concentration of 20% (w/w) compared to GO. Then,

citric acid with a concentration of 10wt% compared to CMC/PEO was added and stirred for 12 h. The uniformly mixed suspension was then spray dried using a BUCHI-290 Mini Spray Dryer with input temperature of 100°C, aspirator set to 100%, and a nitrogen flow rate of 742 L/h. The gel encapsulated within the dry powder was cross-linked by heating at 80°C for 6h and the powder was then immersed in DI water in a one-neck flask at a concentration of 3 mg/ml for 12 h. Chemical reduction to convert the GO to rGO was then conducted by placing the one-neck flask in an oil bath at 80°C for 12 h under continuous stirring. Hydrazine (35wt%) solution was added as a reducing agent (1µl for 3mg of reactant). The final product was dried in a vacuum oven at 40°C for 12 h and denoted as rGO/Gel/Si. Spray dried Gel/Si was prepared in the same way without the addition of GO. Non-spray dried rGO/Gel/Si was prepared using air drying at 40°C to substitute the spray drying process. rGO/Gel/Si (10%) was prepared in the same adding 10% (w/w) of CMC/PEO rather than 20%.

5.1.4 Material Characterization

Scanning electron microscope (SEM) images were taken on a field emission scanning electron microscope (Zeiss LEO1550) with an acceleration voltage of 10 kV. The size distributions of GO/Gel/Si and GO/Si crumpled balls were obtained by counting at least 200 particles in SEM images by ImageJ. Thermogravimetric analysis (Q500, TA Instruments) was performed by heating the sample under air flow from room temperature to 650°C at a rate of 5°C/min. Transmission electron microscope (TEM) images were taken on an energy-filtered transmission electron microscope (Zeiss Libra 200MC) with an acceleration voltage of 200 kV. X-ray photoelectron spectroscopy (Thermal Scientific KAlpha XPS

spectrometer, 150 eV) was carried to analyze the surface elemental composition and chemical bondings. A FEI Titan 80-300 LB was used to obtain high-resolution TEM (HRTEM) image of rGO/Gel/Si. A CMOS detector for electron energy loss spectroscopy (EELS) integrated into the TEM was used for elemental mapping. The depth profiling of rGO/Gel/Si was detected by an Auger Microprobe (MicroLab 350) with an argon ion gun.

5.1.5 Electrochemical Characterization

The working electrode was prepared by mixing the active material, carbon black (carbon super P, MTI), and sodium alginate (Sigma Aldrich) in DI water with a mass ratio of 65:20:15 using a rotor/stator homogenizer. The resulting slurry was cast onto copper foil by a typical film casting doctor blade method, followed by drying at 80°C under vacuum overnight. All rate capability and cyclic stability results were obtained by assembling the fabricated working electrode (~ 1 mg/cm^2 of active material for all studies except for Figure 6b, where ~ 2.5 mg/cm^2 of active material was applied) with a lithium metal foil (Sigma Aldrich, 99.9% trace metal basis) in a coin-type half-cell. A Whatman glass microfiber (Grade GF/A) was used as a separator, and 1 M $LiPF_6$ in a 1:1 v/v mixture of ethylene carbonate (EC) and dimethyl carbonate (DMC) containing 5 vol.% FEC purchased from Canrd China was used as electrolyte. All cells were assembled in an Ar-filled glove box (< 1 ppm O_2 and water) and cycled between 0.01 V and 1.5 V versus Li/Li^+ using a multi-channel battery tester (Wuhan LAND Electronics Co.). Electrochemical impedance spectroscopy (EIS) was carried out on an SP-300 potentiostat (BioLogic) in the range of 1 MHz to 100 mHz with an AC amplitude of 10 mV. Nyquist plots were recorded after the first full cycle (after one discharge and one charge

at 0.1 A/g). The electrodes were charged (delithiated) to 1.5 V, disconnected from the battery tester and connected to the potentiostat where the OCV was around 1.2 V for each sample. EIS was then carried out at this DC voltage vs. lithium metal.

5.2 Results and Discussion

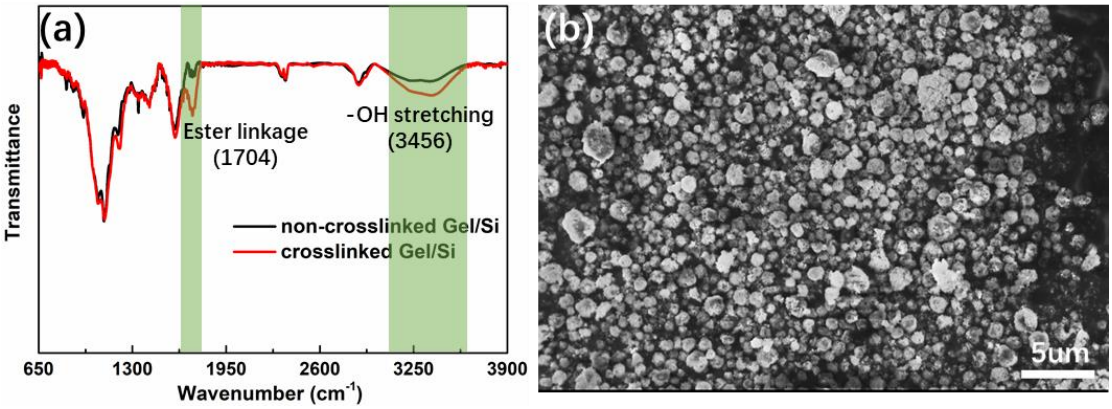

Figure 5.2 (a) FTIR patterns of Gel/Si before and after cross-linking, pure hydrogel, (b) SEM image of Gel/Si after spray drying.

To clearly reveal the bonding environment and confirm the success of cross-linking, FTIR was conducted on Gel/Si without GO before and after cross-linking as shown in **Figure 5.2a** (the corresponding SEM image is shown in **Figure 5.2b**). The peak at around 1704 cm^{-1} belongs to the ester linkage of cross-linking, whose intensity significantly increased after heated Gel/Si at 80°C for 12 h suggesting CMC/PEO polymers were successfully cross-linked by citric acid. Although the spray drying time for every single microdroplet was estimated in the range of ~0.1-10ms,[144] the inlet temperature of spray dryer must be set above 100°C which caused the Gel/Si to be partially cross-linked and results in an observable peak in the curve of the non-cross-linked sample. Furthermore, an increased peak intensity is observed at ~3456 cm^{-1} (–OH stretching) due to increased intramolecular and intermolecular hydrogen

bonding which has been shown to occur after the crosslinking reaction.[145] This can also be attributed to moisture trapped inside the cross-linked hydrogel network. **Figure 5.3b** and **e** show the snapshot images of cross-linked CMC/PEO with 10% of citric acid hydrogel before

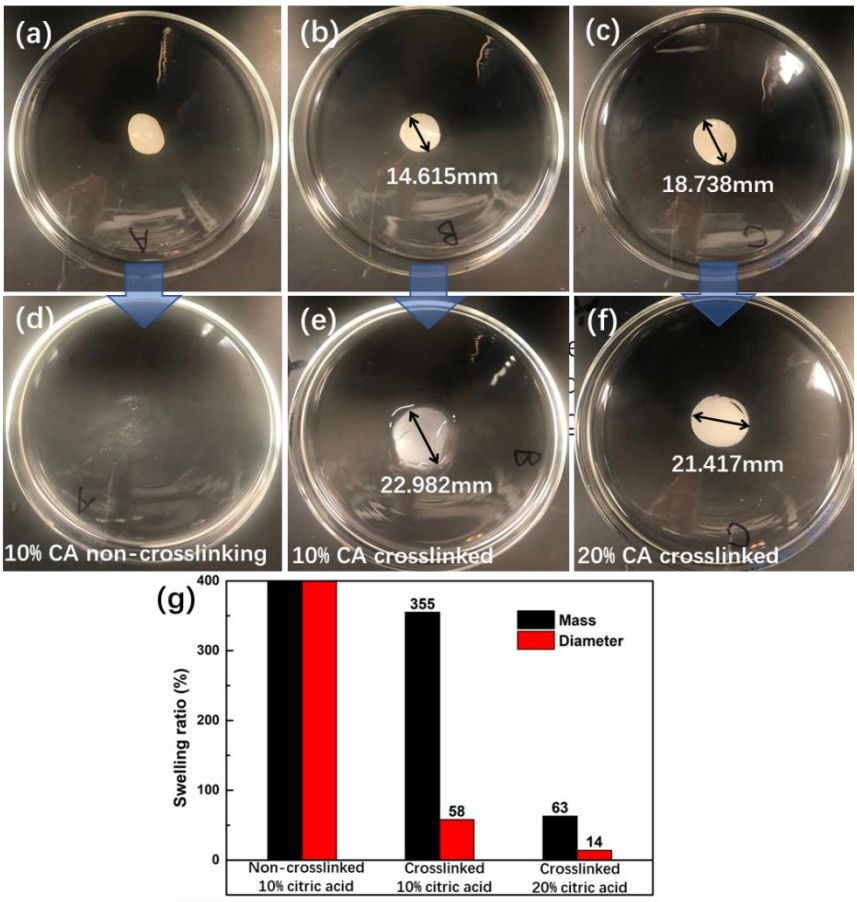

Figure 5.3 Images of CMC/PEO hydrogel prepared at varying conditions before (a-c) and after (d-f) immersed in water for 24h, (g) swelling ratios in diameter and weight of varying hydrogels.

and after immersed in water for 24 h. Immersion resulted in immediate CMC/PEO swelling with an equilibrium reached after 6 h. The gel was able to maintain its shape without dissolution during the full 24 h immersion. The diameter of the hydrogel pellet increased from 14.6 mm to 22.9 mm, displaying a swelling ratio of 58% in diameter and 355% in weight (as summarized in **Figure 5.3g**). When the concentration of citric acid was increased to 20%, the swelling ratios in diameter and weight dropped to 14% and 63%, respectively. Since each

citric acid molecule can bridge at most two polymer chains either between the same or different polymers, the increased amount of citric acid led to the formation of stronger bonding and a tighter crosslinked network which limited the swelling in water. For both of these two well cross-linked hydrogel pellets, the swelling behavior was determined to be reversible as the pellet shrunk to its original dimension after being dried and expanded again after it was re-immersed in water. Usually, the hydrogel pellet further shrinks after being dried under vacuum. This is accompanied by the emergence of cracks generated due to the large stress during volume shrinkage. In contrast, non-cross-linked CMC/PEO hydrogel swelled quickly in water and gradually lost its shape and formed a paste-like structure. Finally, this paste was nearly completely dissolved in water after 24 h (**Figure 5.3d**). Considering its large swelling ratio and outstanding structural stability, the cross-linked CMC/PEO hydrogel containing 10% of citric acid was selected for use in the following electrode preparation.

As shown in our previous chapter, Si NPs in suspension exhibited a much smaller hydrodynamic radius compared to that of GO (~ 41 nm vs. ~ 660 nm on average, which was estimated by dynamic light scattering), suggesting Si NPs have much larger diffusivity according to the Stokes-Einstein relation. The drastic difference between Si NPs and GO sheets in both dimensions and diffusivity is important in designing the quasi-core-shell structure as shown in **Figure 5.1b**. During spray drying, most GO sheets will accumulate at the air/water interface due to the shrinkage of water droplets.[86, 95] Since CMC, PEO, and citric acid can be easily dissolved in water, these hydrogel components are able to redistribute within the core to maintain the concentration balance along with a small

quantity of GO sheets and the majority of Si NPs. The SEM images of spray dried GO/Gel/Si are shown in **Figure 5.4**, all materials displayed a similar spherical shape with plastically

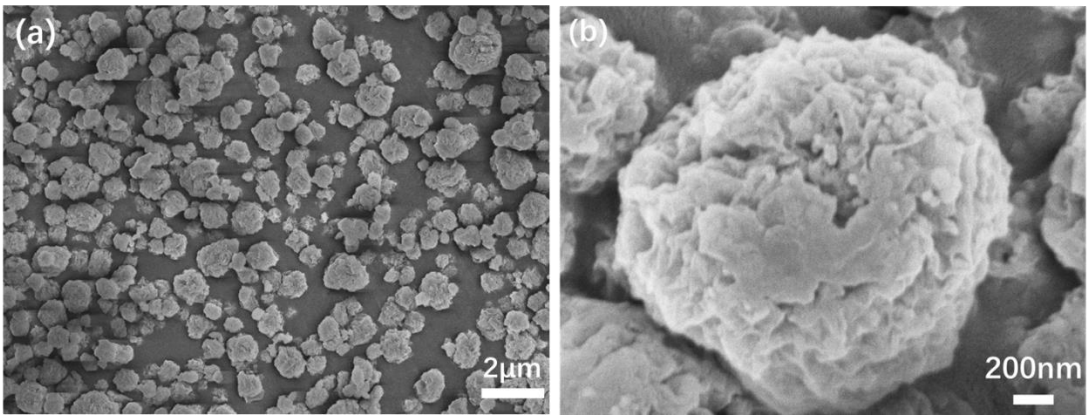

Figure 5.4 SEM images of spray dried GO/Gel/Si with gold coating at varying magnifications.

plastically deformed GO wrinkles distributing around the surface. Few Si NPs were observed in these images suggesting they, along with the gel, were successfully encapsulated within the crumpled GO. The size distributions for GO/Si and GO/Gel/Si are depicted in **Figure 5.5a** and **b**, respectively. After being immersed in water for 12h, the average diameter of GO/Gel/Si increased from 1006.1 nm to 1353.0 nm (swelling ratio in diameter: 34.5 %) while that of GO/Si only increased from 856.3 nm to 919.3 nm with a welling ratio of 7.4 %. The increased swelling ratio is attributed to the hydrogel becoming swollen upon exposure to water. FTIR was also used to confirm cross-linking occurred within the crumpled GO. As shown in **Figure 5.5c**, the newly emerged 1704 cm^{-1} peak in the curve of rGO/Gel/Si indicates that CMC/PEO polymers were successfully cross-linked by citric acid and introduced into the rGO framework. The enhanced peak at 1595 cm^{-1} is caused by more carboxylate anion (COO^-) coming from CMC and PEO. Similarly, the larger peak at 1590 cm^{-1}

which belongs to C-O stretching also suggests the successful introduction of cross-linked CMC/PEO hydrogel.[145]

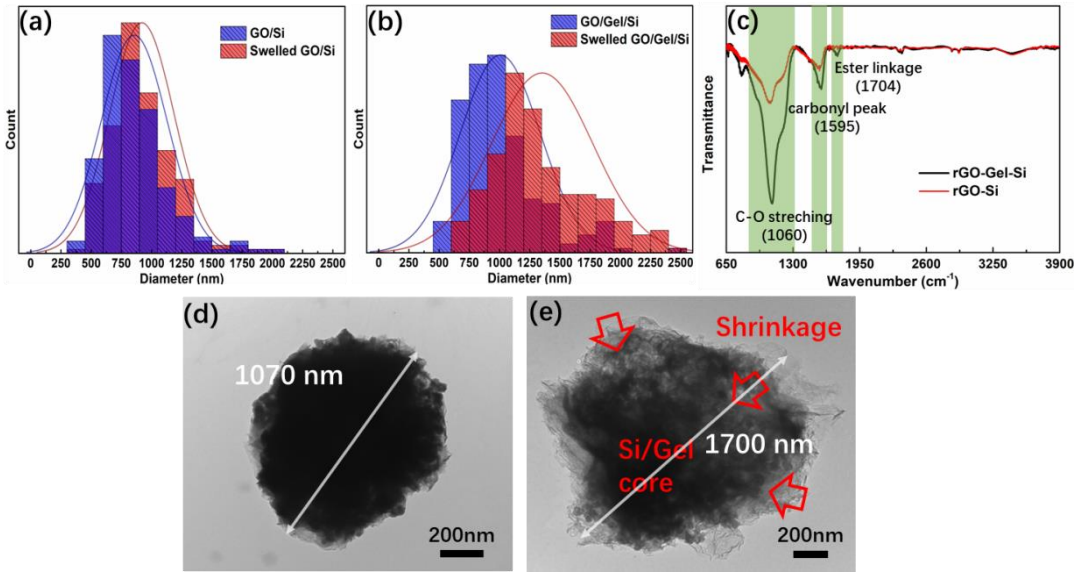

Figure 5.5 size distributions of GO/Si (a) and GO/Gel/Si (b) before and after immersed in water for 12h, (c) FTIR patterns of rGO/Si (after crosslinking and high temperature reduction) with and without hydrogel, TEM images of rGO/Si (d) and rGO/Gel/Si (e).

A TEM image of an rGO/Si particle without the addition of hydrogel is shown in **Figure 5.5d**, the uniformly dark contrast across most of the particles suggests a dense packing of the silicon which prevents transmission of the electron beam. Whereas the edge reveals the appearance of transparent sheet-like structures with wrinkles corresponding to the rGO wrapping around the Si aggregates. The TEM transparency of rGO stems from its low atomic number and thin structure consisting of single- to few-sheet graphene. After the addition of the hydrogel (**Figure 5.5e**) and being fully dried under vacuum, the particles become more transparent to the electron beam and more features of rGO are revealed around regions of darker contrast which likely belong to dense Si NPs and shrunken hydrogel. Moreover, these dark regions are concentrated at one side, illustrating that the shrinkage of

hydrogel leads to the partial separation of Si/rGO core from rGO shell. The inner structure was more clearly investigated by using HRTEM as shown in **Figure 5.6a-c** at varying magnifications. At low magnification (**Figure 5.6a**), the inner void space can be divided into two types: 1) interparticle void space and 2) the void space between rGO edge and Si/rGO aggregates. The former should be attributed to the breakage of the hydrogel, while the latter is caused by the separation/shrinkage of hydrogel from the rGO shell during drying. This is consistent with what we observed for the pure hydrogel, the expansion and shrinkage are usually accompanied by the emergence of cracks. At high magnification (**Figure 5.6c**), no obvious lattice fringes can be found in the region of Si NPs and the quasi-transparent part of rGO exhibits an amorphous feature. At the winkled region of rGO, some lattice fringes can be observed, suggesting some restacking of rGO sheets in the shell. These wrinkles and ridges formed by capillary consolidation during spray drying are known to stabilize the crumpled structure and lead to the compression and aggregation resistance of the crumpled balls.[92, 146] As shown in **Figure 5.6d-g**, elemental mapping was conducted for the same composite ball using EELS. By comparing **Figure 5.6d** with **e**, we see carbon uniformly distributed about the structure suggesting that a 3D crumpled rGO framework formed and wrapped all of the other components within. Na from the NaCMC was also detected (**Figure 5.6f**) and distributed uniformly about the structure suggesting the gel was able to completely fill the core space. The distribution of O and Si are localized within the shell (**Figure 5.6g and h**). In particular, the spatially separated distribution of silicon is apparent in **Figure 5.6h,** which is partially contained within the dried hydrogel network with the oxygen

signal emanating from the PEO, CMC, and the thin surface SiO_2 layer expected to cover the Si NPs.

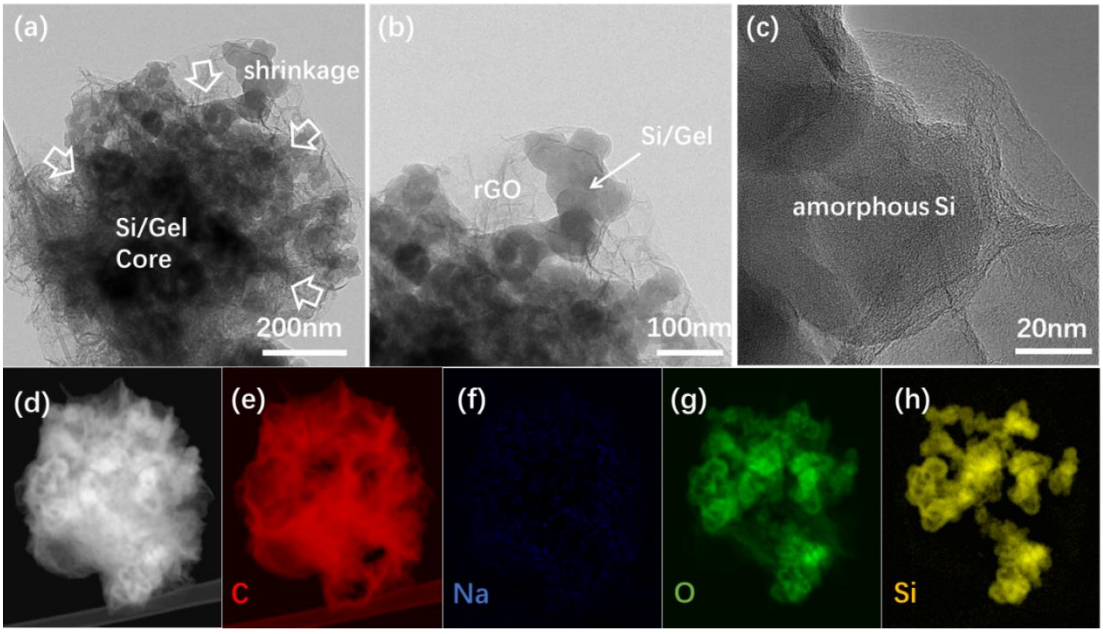

Figure 5.6 (a-c) HRTEM at varying magnifications, (d) survey image, (e-h) EELS elemental mapping for C, Na, O, and Si respectively.

XPS was carried out to analyze the surface chemical composition and bonding information for GO/Si, GO/gel/Si, and rGO/gel/Si as shown in **Figure 5.7a-d**. All samples displayed two sharp and intense peaks at ~284 eV and ~532 eV which belong to the carbon 1s and oxygen 1s peaks, respectively. Two peaks belonging to Si 2s (at ~149 eV) and Si 2p (at ~99 eV) arise from the inside of the structure is very small in rGO/Gel/Si and become negligible in GO/Si and GO/Gel/Si, suggesting that the removal of functional groups on the surface of GO might expose more signal from inside silicon. However, since the composite of silicon in the bulk of the rGO/Gel/Si is around 21.5 at% according to EDS results, it can be confirmed that most Si NPs are wrapped inside. The C/O ratio of the crosslinked GO/Gel/Si

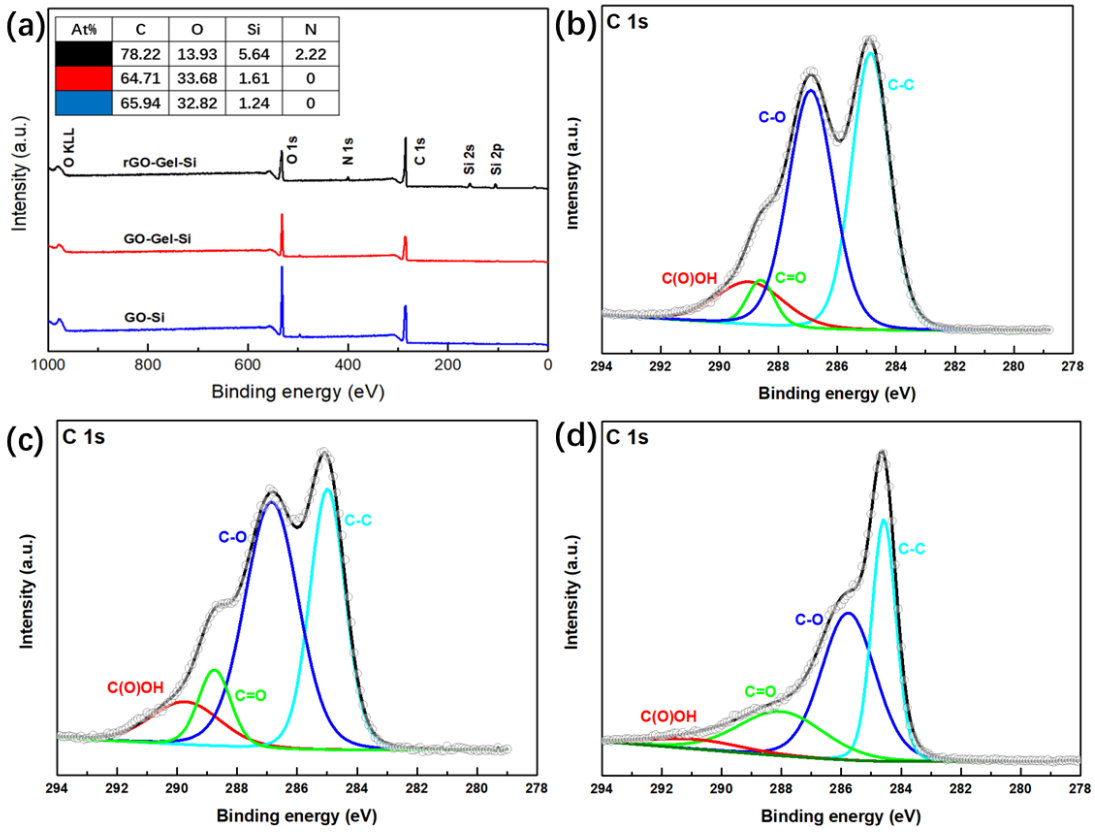

Figure 5.7 (a) high-resolution XPS survey spectra, high-resolution XPS narrow scan spectra of GO/Si (b), GO/Gel/Si (c) and rGO/Gel/Si (d)

(~1.92) is slightly smaller than the GO/Si (~2.01), indicating that some of the polymer constituents of the hydrogel might adsorb to the surface of GO during spray drying because the C/O ratios of all components are less than 2, and the cross-linking upon esterification caused further loss of oxygen. Moreover, the new nitrogen 1s peak emerged in rGO/Gel/Si at ~400 eV, which was doped by hydrazine reduction as described in the literature.[147] High resolution C 1s spectra given in **Figure 5.7b-d** for GO/Si and GO/Gel/Si materials can be deconvoluted into four peaks at around 284.8 eV, 286.9 eV, 287.9 eV, and 288.8 eV, which belong to C-C bonds, C-O bonds, C=O bonds, and C(O)OH bonds, respectively.[148] The slight increase in the peak area of C-O and C=O bonds indicates that residual hydrogel components are adsorbed to the surface of the crumpled rGO shell. Considering the strong interaction

between GO and hydrogel due to a large number of oxygen-containing functional groups (ex. –OH and –COOH), some hydrogel components might be adsorbed or entrapped at the surface or between the inter-layer of crumpled rGO shell during spray drying since they can be easily dissolved in water at the molecular level. After immersion in water and hydrazine reduction, the surface of rGO still contains a large amount of oxygen-containing bonds and the C/O ratio only increased from ~1.92 to ~5.6. This poor reduction efficiency can be attributed to the complex crumpled structure, leading to the decay of reduction efficiency of hydrazine in the deeper place away from the surface of the crumpled rGO framework. This can also be attributed to the volume expansion of the hydrogel before which could expose more polymers to the surface because that the swelling is trying to unfold the crumpled rGO host and escape from its limit. This hypothesis is consistent with our observations when we tried to increase the hydrogel concentration from 20% to 40%, the crumpled rGO unwrapped and Si NPs escaped the carbon host and settled down during the centrifugation washing as shown in **Figure 5.8**.

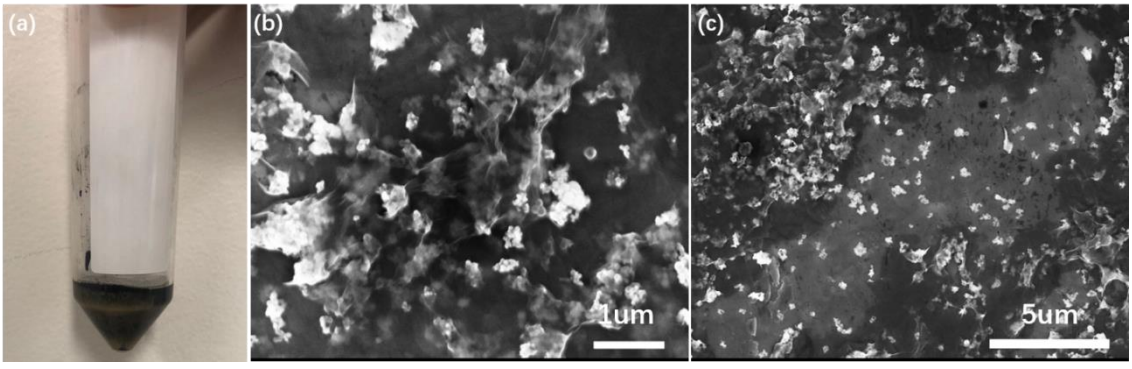

Figure 5.8 (a) Image of rGO/Gel/Si (40%), where Si came out after chemical reduction and settled down to the bottom during centrifugation washing, (b) and (c) SEM images of resulting material from (a) where crumpled rGO framework is broken.

To better characterize the radial elemental distribution within the crumpled rGO/Gel/Si composite, the elemental intensity ratio of C, O, and Si was detected by AES and plotted as the function of sputter time as shown in **Figure 5.9a**. Electrons were focused on a single crumpled composite ball. Both the C/O ratio and C/Si ratio increase until this detect area has been sputtered for 260 s, which confirmed our expectation that most rGO sheets will concentrate at the surface while other components stay inside after spray drying. Even after swelling and chemical reduction, rGO/Gel/Si still maintained such radial elemental distribution. TGA analysis was conducted on both the pure gel and rGO/Gel/Si as shown in **Figure 5.9b** to determine the mass fraction of silicon in this composite. Two significant mass drops are observed in the curve for the pure gel at ~220-300°C and ~400-450°C which are attributed to the thermal decomposition of the hydrogel. Similar behavior was detected for rGO/Gel/Si, but the loss at ~400-450°C is significantly larger because rGO was also burned off at this temperature range. Since the mass ratio of Si to hydrogel is 2:1, the mass fraction of silicon was calculated based on mass retentions in **Figure 5.9b** and determined as ~ 38.1 wt% Si while the hydrogel occupied around 19.1wt%. In the following electrochemical measurement, all specific capacities are reported based on the total mass of rGO, hydrogel and silicon.

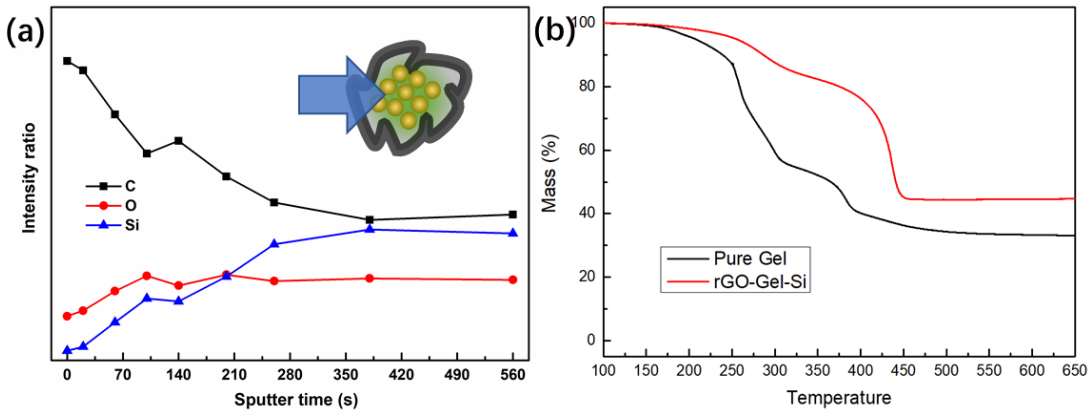

Figure 5.9 (a) AES depth profiling of rGO/Gel/Si, (b) TGA results for of pure CMC/PEO hydrogel and rGO/Gel/Si.

The rate capability of rGO/Gel/Si and rGO/Si was conducted at varying current densities (where 1 A/g is around 0.73C) in the range of 0.1 A/g to 4 A/g and plotted in **Figure 5.10a**. rGO/Gel/Si displayed much better capacity retention (64.1%) compared to that of rGO/Si (48.6%), which only dropped from 1333 mAh/($g_{rGO+Gel+Si}$) at 0.1 A/g to 854 mAh/($g_{rGO+Gel+Si}$) at 4 A/g. The Nyquist plots are presented in **Figure 5.10b** for these two samples. All curves exhibit a semi-circle in the high-frequency region and a straight line in the low-frequency region, which are attributed to charge transfer resistance (R_{ct}) and Warburg diffusion process (Z_w).[149]The slope of all straight lines at the low-frequency region is obviously larger than 45° suggesting the deviation from the ideal semi-infinite diffusion condition, which might be attributed to the additional capacitive behavior caused by the complex porous structure of the crumpled rGO framework.[121, 122] rGO/Gel/Si show a much smaller semi-circle compared to that rGO /Si, indicating a smaller R_{ct} which is consistent with the conclusion drawn in rate capability. That the addition of hydrogel markedly optimized the conductive network of rGO/Si can be explained from three points: 1) the reserved void space provided enough space to buffer the rapid charge/discharge; 2) CMC/PEO, which are common binder

and solid electrolyte used in lithium-ion batteries, have a good ionic conductivity; 3) the small amount of rGO left in the core can be regarded as the conductive additives to improve the electric conductivity of hydrogel. The voltage profiles in terms of specific capacity of rGO/Gel/Si at varying current densities are plotted in **Figure 5.10c**, showing a typical shape for lithiation (discharge) and de-lithiation (charge) process of silicon at 0.2 A/g with the plateaus at ~ 0.3 V - 0.01 V and ~ 0.2 V - 0.6 V, respectively.[56, 150] With increasing current density from 0.2 A/g to 4 A/g, the polarization of Si led to an apparent increase in the de-lithiation potential and reduction of lithiation potential. The capacity contribution of all components from the active materials of rGO/Gel/Si is discussed in **Figure 5.10d**. The weight percentage of Gel, rGO, and Si can be estimated based on the TGA results (**Figure 5.9b**), which are 19.05wt%, 42.85wt%, and 38.1wt% respectively. Assuming the capacity contribution from pure Gel is 0 and hydrazine reduced pure rGO displayed a capacity of ~200 mAh/(g_{rGO}) at 1 A/g,[151] the capacity of 1 gram rGO/Gel/Si contributed by rGO is only 38.1 mAh and by Si is 1016.9 mAh. Hence, the inside Si nanoparticles displayed a true capacity of 2669.03 mAh/(g_{Si}) at 1 A/g, which is around ~74.34% of its theoretical capacity at room temperature.

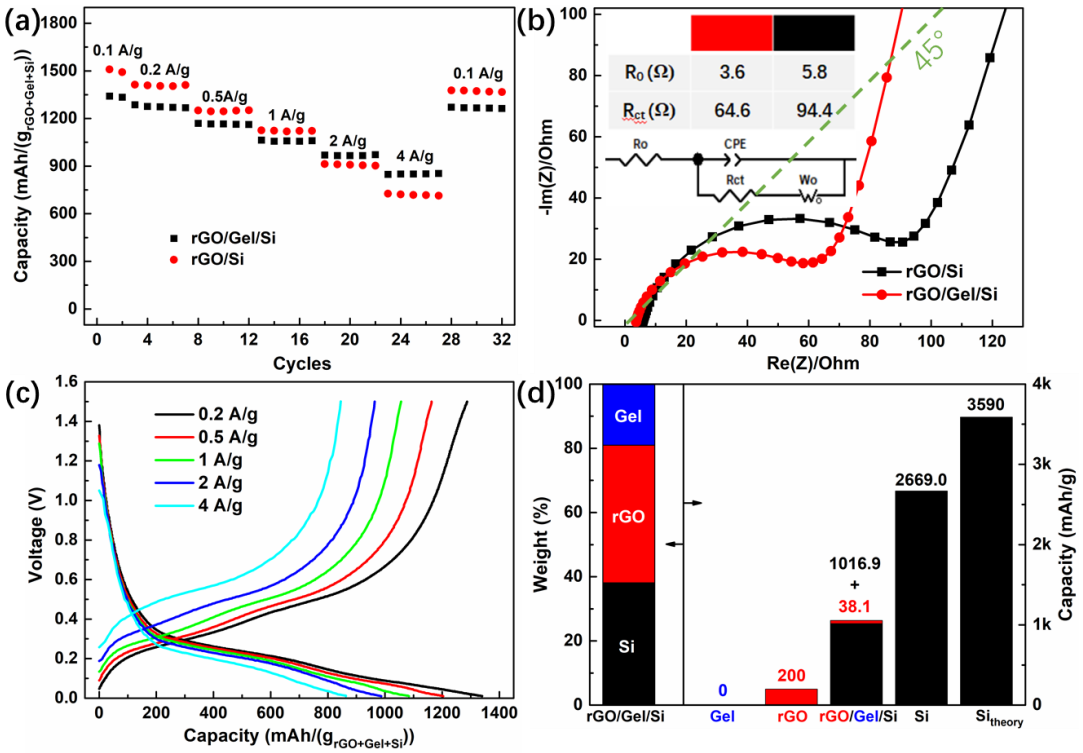

Figure 5.10 (a) rate capability and (b) Nyquist plots of rGO/Si and rGO/Gel/Si, (c) Voltage profiles of rGO/Gel/Si in terms of capacity at varying current densities, (d) discussion of the capacity contribution from varying components to rGO/Gel/Si.

The cyclic stability of varying samples was measured at 1 A/g for 320 cycles after a forming cycle at 0.1 A/g. As shown in **Figure 5.11a**, rGO/Gel/Si displayed the best cycle life, which only dropped from 1055 mAh/(g $_{rGO+Gel+Si}$) to 862 mAh/(g $_{rGO+Gel+Si}$) with a capacity retention of 81.7%. As control groups, the capacity rGO/Gel without spray drying and rGO/Si rapidly decayed to 530 mAh/(g $_{rGO+Gel+Si}$) (~52.6%) and 564 mAh/(g $_{rGO+Gel+Si}$) (~49.3%) after 320 cycles, indicating that the electrode displayed the best performance only when certain void space was reserved between crumpled rGO shell and Gel/Si core. To improve the overall capacity, we also tried to decrease the addition amount of CMC/PEO during sample preparation from 20% to 10%, the resulting material only retained ~62.5% of capacity with a small improvement in capacity but worse cycle life. As we discussed previously, increasing

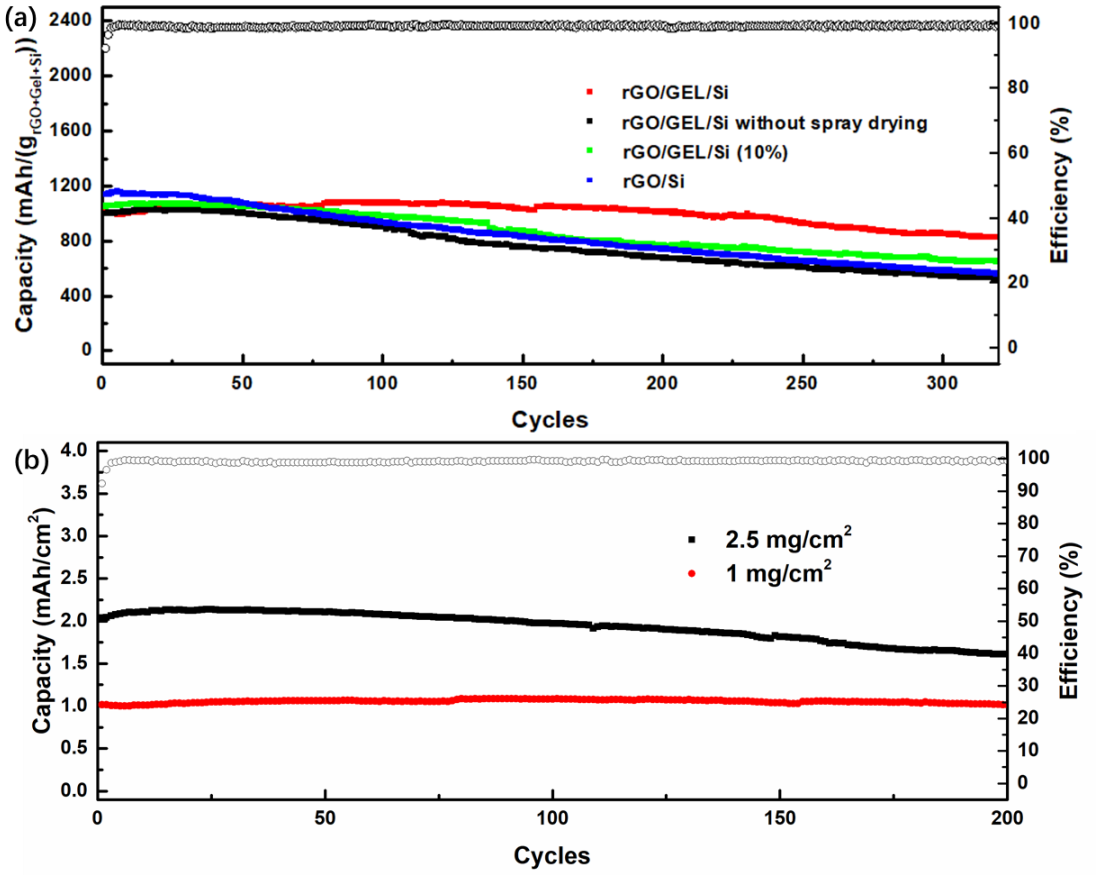

Figure 5.11 (a) cyclic stability of rGO/Si and rGO/Gel/Si prepared at varying conditions, (b) cyclic stability of rGO/Gel/Si at varying mass loadings of active materials.

the volume of hydrogel beyond 40% introduces stresses on the rGO framework leading to rGO unwrapping and exposure of Si NPs after hydrazine reduction. rGO/Gel/Si with 20% of CMC/PEO addition formed an optimized inner structure and exhibited the best electrochemical performance. Even after the mass loading of active materials (rGO+Gel+Si) was increased from 1 mg/cm^2 to 2.5 mg/cm^2, rGO/Gel/Si still can retain around 79% of the initial capacity (~ 2.1 mAh/cm^2) after 200 cycles as shown in **Figure 5.11b**. This is the first time that the void space between carbon shell and silicon core is achieved taking advantage of the swelling/shrinkage of hydrogel in wet/dry states, the resulting material displayed

competitive electrochemical performance as shown in **Figure 5.12** although the hydrogel fille cannot provide capacity to store lithium ions.

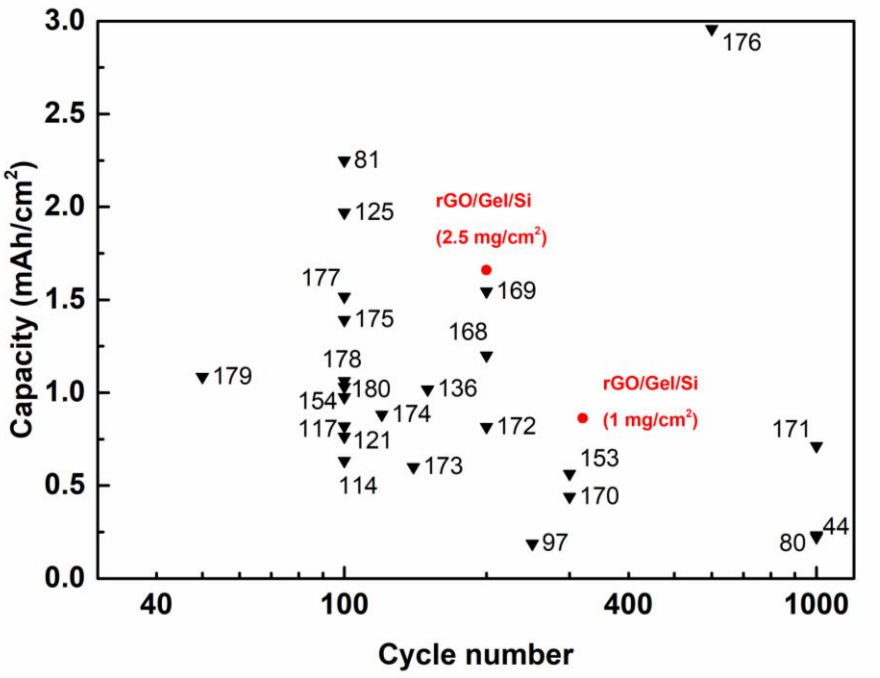

Figure 5.12 Capacity retention of recent works about Si/C based composites with artificially or naturally reserved void space[44, 80, 81, 98, 112, 123, 126-143]

5.3 Conclusions

In summary, we have developed a novel method to improve the electrochemical performance of Si/C based anodes. PEO and CMC polymer chains were successfully cross-linked and wrapped inside a crumpled rGO framework with Si NPs. This process takes advantage of the inate feature of the CMC/PEO hydrogel which swells in water and shrinks after drying, thereby expanding the volume of GO framework during water immersion. The void space between rGO shell and Gel/Si core is then introduced by drying in air, meanwhile, the GO was chemically reduced. The resulting void space was visually demonstrated by HRTEM and EELS elemental mapping. With the optimized structure, rGO/Gel/Si displayed a

significantly improved cyclic stability, which only dropped by 18.3% from 1055 mAh/($g_{rGO+Gel+Si}$) after 320 cycles at 320 cycles. Although the weight content of silicon is only 38.1wt%, around 96.4% of capacity is contributed by silicon with a real capacity of 2669.03 mAh/(g_{Si}).

6 Conclusion and Future Works

6.1 Conclusion

In this thesis, the battery performance of silicon was improved by crumpled graphene wrapping via three different methods as discussed in above chapters. In the end, the main progress of each work is briefly summarized below.

In **Chapter 3**, we first optimized the spray drying procedure to make the resulting composited achieve the best battery performance. It was determined that the CrGO/Si produced at N_2 flow rate of 742 L/h, GO concentration of 0.5 mg/ml and GO/Si mass ratio of 1:0.3 displayed the most crumpled morphology and the most uniform size distribution with small particle size. By fabricating with lithium metal as half-cells, this material displayed the best rate capability and cyclic stability. To further enhance the structural stability, a layer of polydopamine was deposited at the surface of GO and then carbonized to an N-doped carbon shell. This second carbon shell is coated at CrGO/Si (1:0.6) rather than CrGO/Si (1:0.3), aiming to maintain the carbon content at a similar level (~45%). The resulting cpDOPA/CrGO/Si exhibited a high capacity of 1007 mAh/g even after 200 cycles at 1 A/g, the reinforced material displayed significantly enhanced cycle stability displaying a lower decay rate of 0.12% per cycle. Meanwhile, the optimized initial coulombic efficiency (76.3%) also demonstrated that the addition of cpDOPA coating effectively decreased direct contact of Si by the electrolyte.

In **Chapter 4**, polystyrene nanoparticles, which has similar particle size with Si NPs (~100 nm), were synthesized by simple seeded emulsion polymerization. Since this polymer can be fully removed under nitrogen flow at around 450°C, it used as sacrificing materials to creat the void space in CrGO/Si composite. It was observed that the capacity retention of voided CrGO/Si gradually increased from 49.0% to 63.2% and finally reached 71.9% when the mass ratio of PS/Si was increased from 0 to 0.5 to 1. However, the retention decreased to 61.7% after the PS/Si ratio was increased to 2, suggesting that 1:1 is the optimal ratio to make a voided crumpled graphene with improved inside conductive network, meanwhile, the medium volume of void avoid making the transport/diffusion pathway of ions/electros too long. The optimized voided composite also displayed a high capacity of 1468 mAh/g at 1 A/g and only dropped by 19.4% after 200 cycles.

In **Chapter 5**, we have developed a novel method to improve the electrochemical performance of Si/C based anodes. PEO and CMC polymer chains were successfully cross-linked and wrapped inside a crumpled rGO framework with Si NPs. Depending on the feature of hydrogel which will swell in water and shrink after drying, the volume of GO framework was expanded during water immersion. And then the void space between the rGO shell and Gel/Si core was created by drying in the air. Meanwhile, the GO was chemically reduced by hydrazine. The resulting void space was visually demonstrated by HRTEM and EELS elemental mapping. With the optimized structure, CrGO/Gel/Si displayed a significantly improved cyclic stability, which only dropped by 18.3% from 1055 mAh/g after 320 cycles at 320 cycles. Although the weight content of silicon is only 38.1wt%, around 96.4% of capacity is contributed by silicon with a real capacity of 2669.03 mAh/g.

Comparing all of these three materials produced in this thesis, the voided CrGO/Si upon removal of polystyrene displayed the best rate capability because of the optimized inside conductive network. The hydrogel containing CrGO/Si exhibited outstanding cyclic stability since Gel can work as the glue, enhancing the structural stability, as well as the template to create void space inside crumpled graphene framework.

6.2 Future Works

In **Chapter 3**, although the second carbonized polydopamine layer can significantly improve the electrochemical performance of CrGO/Si and effectively limit the direct contact of Si to electrolyte, the inside Si NPs are still severely aggregated together. The double enhanced carbon shell (cpDOPA+rGO) can only tolerate the volume expansion of silicon, but cannot release the large stress generated at the interface of C/Si. Hence, applying the cpDOPA sealing on a voided CrGO/Si may be a good idea to further improve the performance.

Since polystyrene, which was used as sacrificial materials in **Chapter 4**, is a very poor electric conductor and cannot provide capacity, its residue may cause severe performance decay if it is not fully removed during heat treatment. In fact, this was observed if the inert gas flow-rate was not sufficient in the tube furnace during thermal reduction/decomposition. Enough inert gas flow has to be provided to ensure all decomposed PS vapor can be effectively blown away. To avoid this problem, some carbon precursors with similar dimensions and significant volume shrinkage after carbonization can be used to substitute the role of polystyrene in this work.

Although the hydrogel containing work (**Chapter 5**) displayed the best cyclic stability among all three materials in this thesis, its capacity is relatively low compared to other two works due to the introduction of hydrogel, which cannot provide contributions to overall capacity. Meanwhile, without enough amount, the shrinkage of hydrogel cannot provide enough void and strength to lead to a stable cycle performance. Hence, there might be two routes to further improved performance: 1) optimizing the conductivity of hydrogel by doping or other modification methods, and 2) changing the type of polymers which can form a hydrogel with larger volume change between wet state and dry state.

Reference

1. Rhodes, C. J., The 2015 Paris climate change conference: COP21. *Sci. Prog.* **2016,** *99* (1), 97-104.
2. Siegenthaler, U.; Oeschger, H., Biospheric CO2 emissions during the past 200 years reconstructed by deconvolution of ice core data. *Tellus B: Chemical and Physical Meteorology* **1987,** *39* (1-2), 140-154.
3. Edenhofer, O.; Pichs-Madruga, R.; Sokona, Y.; Farahani, E.; Kadner, S.; Seyboth, K.; Adler, A.; Baum, I.; Brunner, S.; Eickemeier, P., Contribution of Working Group III to the Fifth Assessment Report of the Intergovernmental Panel on Climate Change. *Climate change* **2014**, 1-11.
4. Johansson, T. B.; Kelly, H.; Reddy, A. K.; Williams, R. H., Renewable energy: sources for fuels and electricity. **1993**.
5. Hadjipaschalis, I.; Poullikkas, A.; Efthimiou, V., Overview of current and future energy storage technologies for electric power applications. *Renewable and sustainable energy reviews* **2009,** *13* (6-7), 1513-1522.
6. Baker, J., New technology and possible advances in energy storage. *Energy Policy* **2008,** *36* (12), 4368-4373.
7. Wang, Y.; Liu, B.; Li, Q.; Cartmell, S.; Ferrara, S.; Deng, Z. D.; Xiao, J., Lithium and lithium ion batteries for applications in microelectronic devices: A review. *J. Power Sources* **2015,** *286*, 330-345.
8. Liang, Y.; Zhao, C. Z.; Yuan, H.; Chen, Y.; Zhang, W.; Huang, J. Q.; Yu, D.; Liu, Y.; Titirici, M. M.; Chueh, Y. L., A review of rechargeable batteries for portable electronic devices. *InfoMat* **2019,** *1* (1), 6-32.
9. Hannan, M.; Hoque, M. M.; Mohamed, A.; Ayob, A., Review of energy storage systems for electric vehicle applications: Issues and challenges. *Renewable and Sustainable Energy Reviews* **2017,** *69*, 771-789.
10. Cabana, J.; Monconduit, L.; Larcher, D.; Palacin, M. R., Beyond intercalation‐based Li‐ion batteries: the state of the art and challenges of electrode materials reacting through conversion reactions. *Adv. Mater.* **2010,** *22* (35), E170-E192.
11. Tran, T.; Feikert, J.; Song, X.; Kinoshita, K., Commercial carbonaceous materials as lithium intercalation anodes. *J. Electrochem. Soc.* **1995,** *142* (10), 3297.
12. Guerard, D.; Herold, A., Intercalation of lithium into graphite and other carbons. *Carbon* **1975,** *13* (4), 337-345.
13. Su, X.; Wu, Q.; Li, J.; Xiao, X.; Lott, A.; Lu, W.; Sheldon, B. W.; Wu, J., Silicon‐based nanomaterials for lithium‐ion batteries: a review. *Advanced Energy Materials* **2014,** *4* (1), 1300882.
14. Ma, D.; Cao, Z.; Hu, A., Si-based anode materials for Li-ion batteries: a mini review. *Nano-Micro Letters* **2014,** *6* (4), 347-358.
15. Etacheri, V.; Marom, R.; Elazari, R.; Salitra, G.; Aurbach, D., Challenges in the development of advanced Li-ion batteries: a review. *Energy & Environmental Science* **2011,** *4* (9), 3243-3262.

16. Wang, L.; Ding, C.; Zhang, L.; Xu, H.; Zhang, D.; Cheng, T.; Chen, C., A novel carbon–silicon composite nanofiber prepared via electrospinning as anode material for high energy-density lithium ion batteries. *J. Power Sources* **2010,** *195* (15), 5052-5056.
17. Si, Q.; Hanai, K.; Imanishi, N.; Kubo, M.; Hirano, A.; Takeda, Y.; Yamamoto, O., Highly reversible carbon–nano-silicon composite anodes for lithium rechargeable batteries. *J. Power Sources* **2009,** *189* (1), 761-765.
18. Okubo, M.; Hosono, E.; Kim, J.; Enomoto, M.; Kojima, N.; Kudo, T.; Zhou, H.; Honma, I., Nanosize effect on high-rate Li-ion intercalation in LiCoO2 electrode. *J. Am. Chem. Soc.* **2007,** *129* (23), 7444-7452.
19. Nishida, Y.; Nakane, K.; Satoh, T., Synthesis and properties of gallium-doped LiNiO2 as the cathode material for lithium secondary batteries. *J. Power Sources* **1997,** *68* (2), 561-564.
20. Armstrong, A. R.; Bruce, P. G., Synthesis of layered LiMnO 2 as an electrode for rechargeable lithium batteries. *Nature* **1996,** *381* (6582), 499-500.
21. Wu, Y.; Rahm, E.; Holze, R., Carbon anode materials for lithium ion batteries. *J. Power Sources* **2003,** *114* (2), 228-236.
22. Dey, A., Electrochemical alloying of lithium in organic electrolytes. *J. Electrochem. Soc.* **1971,** *118* (10), 1547.
23. Wang, G.; Wang, B.; Wang, X.; Park, J.; Dou, S.; Ahn, H.; Kim, K., Sn/graphene nanocomposite with 3D architecture for enhanced reversible lithium storage in lithium ion batteries. *J. Mater. Chem.* **2009,** *19* (44), 8378-8384.
24. Chan, C. K.; Zhang, X. F.; Cui, Y., High capacity Li ion battery anodes using Ge nanowires. *Nano Lett.* **2008,** *8* (1), 307-309.
25. Nam, D. H.; Hong, K. S.; Lim, S. J.; Kim, M. J.; Kwon, H. S., High‐performance Sb/Sb2O3 anode materials using a polypyrrole nanowire network for Na‐ion batteries. *small* **2015,** *11* (24), 2885-2892.
26. Arora, P.; Zhang, Z., Battery separators. *Chem. Rev.* **2004,** *104* (10), 4419-4462.
27. Venugopal, G.; Moore, J.; Howard, J.; Pendalwar, S., Characterization of microporous separators for lithium-ion batteries. *J. Power Sources* **1999,** *77* (1), 34-41.
28. Younesi, R.; Veith, G. M.; Johansson, P.; Edström, K.; Vegge, T., Lithium salts for advanced lithium batteries: Li–metal, Li–O 2, and Li–S. *Energy & Environmental Science* **2015,** *8* (7), 1905-1922.
29. Wakihara, M.; Yamamoto, O., *Lithium ion batteries: fundamentals and performance*. John Wiley & Sons: 2008.
30. Chen, S.; Niu, C.; Lee, H.; Li, Q.; Yu, L.; Xu, W.; Zhang, J.-G.; Dufek, E. J.; Whittingham, M. S.; Meng, S., Critical parameters for evaluating coin cells and pouch cells of rechargeable Li-metal batteries. *Joule* **2019,** *3* (4), 1094-1105.
31. Park, J.-K., *Principles and applications of lithium secondary batteries*. John Wiley & Sons: 2012.
32. Goodenough, J. B.; Park, K.-S., The Li-ion rechargeable battery: a perspective. *J. Am. Chem. Soc.* **2013,** *135* (4), 1167-1176.
33. Naguib, M.; Halim, J.; Lu, J.; Cook, K. M.; Hultman, L.; Gogotsi, Y.; Barsoum, M. W., New two-dimensional niobium and vanadium carbides as promising materials for Li-ion batteries. *J. Am. Chem. Soc.* **2013,** *135* (43), 15966-15969.

34. Ren, C. E.; Zhao, M. Q.; Makaryan, T.; Halim, J.; Boota, M.; Kota, S.; Anasori, B.; Barsoum, M. W.; Gogotsi, Y., Porous two‐dimensional transition metal carbide (MXene) flakes for high‐performance Li‐ion storage. *ChemElectroChem* **2016,** *3* (5), 689-693.
35. Park, K.-S.; Benayad, A.; Kang, D.-J.; Doo, S.-G., Nitridation-driven conductive Li4Ti5O12 for lithium ion batteries. *J. Am. Chem. Soc.* **2008,** *130* (45), 14930-14931.
36. Ma, Z.; Gao, X.; She, Z.; Pope, M. A.; Li, Y., Ultrasmall TiOx Nanoparticles Rich in Oxygen Vacancies Synthesized through a Simple Strategy for Ultrahigh‐Rate Lithium‐Ion Batteries. *ChemElectroChem* **2020,** *7* (19), 4124-4130.
37. Ng, S.; Wang, J.; Guo, Z.; Chen, J.; Wang, G.; Liu, H., Single wall carbon nanotube paper as anode for lithium-ion battery. *Electrochim. Acta* **2005,** *51* (1), 23-28.
38. Landi, B. J.; Ganter, M. J.; Cress, C. D.; DiLeo, R. A.; Raffaelle, R. P., Carbon nanotubes for lithium ion batteries. *Energy & Environmental Science* **2009,** *2* (6), 638-654.
39. Liu, H.; Wang, G.; Liu, J.; Qiao, S.; Ahn, H., Highly ordered mesoporous NiO anode material for lithium ion batteries with an excellent electrochemical performance. *J. Mater. Chem.* **2011,** *21* (9), 3046-3052.
40. Huang, G.; Xu, S.; Lu, S.; Li, L.; Sun, H., Micro-/nanostructured Co3O4 anode with enhanced rate capability for lithium-ion batteries. *ACS applied materials & interfaces* **2014,** *6* (10), 7236-7243.
41. Reddy, M.; Yu, T.; Sow, C.-H.; Shen, Z. X.; Lim, C. T.; Subba Rao, G.; Chowdari, B., α‐Fe2O3 nanoflakes as an anode material for Li‐ion batteries. *Adv. Funct. Mater.* **2007,** *17* (15), 2792-2799.
42. Lai, H.; Li, J.; Chen, Z.; Huang, Z., Carbon nanohorns as a high-performance carrier for MnO2 anode in lithium-ion batteries. *ACS applied materials & interfaces* **2012,** *4* (5), 2325-2328.
43. Parker, J. F.; Chervin, C. N.; Pala, I. R.; Machler, M.; Burz, M. F.; Long, J. W.; Rolison, D. R., Rechargeable nickel–3D zinc batteries: An energy-dense, safer alternative to lithium-ion. *Science* **2017,** *356* (6336), 415-418.
44. Liu, N.; Lu, Z.; Zhao, J.; McDowell, M. T.; Lee, H.-W.; Zhao, W.; Cui, Y., A pomegranate-inspired nanoscale design for large-volume-change lithium battery anodes. *Nature nanotechnology* **2014,** *9* (3), 187-192.
45. Feckl, J. M.; Fominykh, K.; Döblinger, M.; Fattakhova‐Rohlfing, D.; Bein, T., Nanoscale porous framework of lithium titanate for ultrafast lithium insertion. *Angew. Chem.* **2012,** *124* (30), 7577-7581.
46. Liang, Z.; Hui-Lin, P.; Yong-Sheng, H.; Hong, L.; Li-Quan, C., Spinel lithium titanate (Li4Ti5O12) as novel anode material for room-temperature sodium-ion battery. *Chinese Physics B* **2012,** *21* (2), 028201.
47. Li, B.; Zheng, J.; Zhang, H.; Jin, L.; Yang, D.; Lv, H.; Shen, C.; Shellikeri, A.; Zheng, Y.; Gong, R., Electrode materials, electrolytes, and challenges in nonaqueous lithium‐ion capacitors. *Adv. Mater.* **2018,** *30* (17), 1705670.
48. Guo, B.; Yu, X.; Sun, X.-G.; Chi, M.; Qiao, Z.-A.; Liu, J.; Hu, Y.-S.; Yang, X.-Q.; Goodenough, J. B.; Dai, S., A long-life lithium-ion battery with a highly porous TiNb 2 O 7 anode for large-scale electrical energy storage. *Energy & Environmental Science* **2014,** *7* (7), 2220-2226.

49. Ise, K.; Morimoto, S.; Harada, Y.; Takami, N., Large lithium storage in highly crystalline TiNb2O7 nanoparticles synthesized by a hydrothermal method as anodes for lithium-ion batteries. *Solid State Ionics* **2018,** *320*, 7-15.
50. Goriparti, S.; Miele, E.; De Angelis, F.; Di Fabrizio, E.; Zaccaria, R. P.; Capiglia, C., Review on recent progress of nanostructured anode materials for Li-ion batteries. *J. Power Sources* **2014,** *257*, 421-443.
51. Exley, C., Silicon in life: a bioinorganic solution to bioorganic essentiality. *J. Inorg. Biochem.* **1998,** *69* (3), 139-144.
52. Braga, M. H.; Dębski, A.; Gąsior, W., Li–Si phase diagram: Enthalpy of mixing, thermodynamic stability, and coherent assessment. *J. Alloys Compd.* **2014,** *616*, 581-593.
53. Wu, H.; Cui, Y., Designing nanostructured Si anodes for high energy lithium ion batteries. *Nano today* **2012,** *7* (5), 414-429.
54. Obrovac, M.; Christensen, L., Structural changes in silicon anodes during lithium insertion/extraction. *Electrochemical and Solid State Letters* **2004,** *7* (5), A93.
55. Li, J.; Dahn, J., An in situ X-ray diffraction study of the reaction of Li with crystalline Si. *J. Electrochem. Soc.* **2007,** *154* (3), A156.
56. Obrovac, M.; Krause, L., Reversible cycling of crystalline silicon powder. *J. Electrochem. Soc.* **2006,** *154* (2), A103.
57. McDowell, M. T.; Lee, S. W.; Harris, J. T.; Korgel, B. A.; Wang, C.; Nix, W. D.; Cui, Y., In situ TEM of two-phase lithiation of amorphous silicon nanospheres. *Nano Lett.* **2013,** *13* (2), 758-764.
58. Yang, H.; Huang, S.; Huang, X.; Fan, F.; Liang, W.; Liu, X. H.; Chen, L.-Q.; Huang, J. Y.; Li, J.; Zhu, T., Orientation-dependent interfacial mobility governs the anisotropic swelling in lithiated silicon nanowires. *Nano Lett.* **2012,** *12* (4), 1953-1958.
59. Lee, S. W.; McDowell, M. T.; Choi, J. W.; Cui, Y., Anomalous shape changes of silicon nanopillars by electrochemical lithiation. *Nano Lett.* **2011,** *11* (7), 3034-3039.
60. Golmon, S.; Maute, K.; Lee, S.-H.; Dunn, M. L., Stress generation in silicon particles during lithium insertion. *Appl. Phys. Lett.* **2010,** *97* (3), 033111.
61. Chon, M. J.; Sethuraman, V. A.; McCormick, A.; Srinivasan, V.; Guduru, P. R., Real-time measurement of stress and damage evolution during initial lithiation of crystalline silicon. *Phys. Rev. Lett.* **2011,** *107* (4), 045503.
62. Sun, Y.; Liu, N.; Cui, Y., Promises and challenges of nanomaterials for lithium-based rechargeable batteries. *Nature Energy* **2016,** *1* (7), 1-12.
63. Liu, X. H.; Zhong, L.; Huang, S.; Mao, S. X.; Zhu, T.; Huang, J. Y., Size-dependent fracture of silicon nanoparticles during lithiation. *ACS nano* **2012,** *6* (2), 1522-1531.
64. Brace, W., An extension of the Griffith theory of fracture to rocks. *Journal of Geophysical Research* **1960,** *65* (10), 3477-3480.
65. Balbuena, P. B.; Wang, Y. X., *Lithium-ion batteries: solid-electrolyte interphase*. World Scientific: 2004.
66. Verma, P.; Maire, P.; Novák, P., A review of the features and analyses of the solid electrolyte interphase in Li-ion batteries. *Electrochim. Acta* **2010,** *55* (22), 6332-6341.
67. Aupperle, F.; von Aspern, N.; Berghus, D.; Weber, F.; Eshetu, G. G.; Winter, M.; Figgemeier, E., The Role of Electrolyte Additives on the Interfacial Chemistry and Thermal

Reactivity of Si-Anode-Based Li-Ion Battery. *ACS applied energy materials* **2019,** *2* (9), 6513-6527.

68. Song, T.; Xia, J.; Lee, J.-H.; Lee, D. H.; Kwon, M.-S.; Choi, J.-M.; Wu, J.; Doo, S. K.; Chang, H.; Park, W. I., Arrays of sealed silicon nanotubes as anodes for lithium ion batteries. *Nano Lett.* **2010,** *10* (5), 1710-1716.

69. Bang, B. M.; Lee, J. I.; Kim, H.; Cho, J.; Park, S., High‐performance macroporous bulk silicon anodes synthesized by template‐free chemical etching. *Advanced Energy Materials* **2012,** *2* (7), 878-883.

70. Ge, M.; Lu, Y.; Ercius, P.; Rong, J.; Fang, X.; Mecklenburg, M.; Zhou, C., Large-scale fabrication, 3D tomography, and lithium-ion battery application of porous silicon. *Nano Lett.* **2014,** *14* (1), 261-268.

71. Wen, Z.; Yang, J.; Wang, B.; Wang, K.; Liu, Y., High capacity silicon/carbon composite anode materials for lithium ion batteries. *Electrochem. Commun.* **2003,** *5* (2), 165-168.

72. Thakur, M.; Isaacson, M.; Sinsabaugh, S. L.; Wong, M. S.; Biswal, S. L., Gold-coated porous silicon films as anodes for lithium ion batteries. *J. Power Sources* **2012,** *205*, 426-432.

73. Yu, Y.; Gu, L.; Zhu, C.; Tsukimoto, S.; Van Aken, P. A.; Maier, J., Reversible storage of lithium in silver‐coated three‐dimensional macroporous silicon. *Adv. Mater.* **2010,** *22* (20), 2247-2250.

74. Dimov, N.; Kugino, S.; Yoshio, M., Carbon-coated silicon as anode material for lithium ion batteries: advantages and limitations. *Electrochim. Acta* **2003,** *48* (11), 1579-1587.

75. Zuo, X.; Zhu, J.; Müller-Buschbaum, P.; Cheng, Y.-J., Silicon based lithium-ion battery anodes: A chronicle perspective review. *Nano Energy* **2017,** *31*, 113-143.

76. Wang, C.; Wu, G.; Zhang, X.; Qi, Z.; Li, W., Lithium insertion in carbon‐silicon composite materials produced by mechanical milling. *J. Electrochem. Soc.* **1998,** *145* (8), 2751.

77. Du, F. H.; Li, B.; Fu, W.; Xiong, Y. J.; Wang, K. X.; Chen, J. S., Surface binding of polypyrrole on porous Silicon hollow nanospheres for Li‐ion battery anodes with high structure Stability. *Adv. Mater.* **2014,** *26* (35), 6145-6150.

78. Wilson, A.; Way, B.; Dahn, J.; Van Buuren, T., Nanodispersed silicon in pregraphitic carbons. *J. Appl. Phys.* **1995,** *77* (6), 2363-2369.

79. Kim, J. M.; Guccini, V.; Kim, D.; Oh, J.; Park, S.; Jeon, Y.; Hwang, T.; Salazar-Alvarez, G.; Piao, Y., A novel textile-like carbon wrapping for high-performance silicon anodes in lithium-ion batteries. *Journal of Materials Chemistry A* **2018,** *6* (26), 12475-12483.

80. Liu, N.; Wu, H.; McDowell, M. T.; Yao, Y.; Wang, C.; Cui, Y., A yolk-shell design for stabilized and scalable Li-ion battery alloy anodes. *Nano Lett.* **2012,** *12* (6), 3315-3321.

81. Zhang, L.; Wang, C.; Dou, Y.; Cheng, N.; Cui, D.; Du, Y.; Liu, P.; Al‐Mamun, M.; Zhang, S.; Zhao, H., A yolk‐shell structured silicon anode with superior conductivity and high tap density for full lithium‐ion batteries. *Angew. Chem. Int. Ed.* **2019,** *58* (26), 8824-8828.

82. Sun, L.; Su, T.; Xu, L.; Du, H.-B., Preparation of uniform Si nanoparticles for high-performance Li-ion battery anodes. *PCCP* **2016,** *18* (3), 1521-1525.

83. Wang, W.; Kumta, P. N., Nanostructured hybrid silicon/carbon nanotube heterostructures: reversible high-capacity lithium-ion anodes. *ACS nano* **2010,** *4* (4), 2233-2241.
84. Hertzberg, B.; Alexeev, A.; Yushin, G., Deformations in Si− Li anodes upon electrochemical alloying in nano-confined space. *J. Am. Chem. Soc.* **2010,** *132* (25), 8548-8549.
85. Osman, A.; Goehring, L.; Patti, A.; Stitt, H.; Shokri, N., Fundamental investigation of the drying of solid suspensions. *Industrial & Engineering Chemistry Research* **2017,** *56* (37), 10506-10513.
86. Lintingre, E.; Lequeux, F.; Talini, L.; Tsapis, N., Control of particle morphology in the spray drying of colloidal suspensions. *Soft Matter* **2016,** *12* (36), 7435-7444.
87. Nandiyanto, A. B. D.; Okuyama, K., Progress in developing spray-drying methods for the production of controlled morphology particles: From the nanometer to submicrometer size ranges. *Adv. Powder Technol.* **2011,** *22* (1), 1-19.
88. Vehring, R., Pharmaceutical particle engineering via spray drying. *Pharm. Res.* **2008,** *25* (5), 999-1022.
89. Parviz, D.; Metzler, S. D.; Das, S.; Irin, F.; Green, M. J., Tailored crumpling and unfolding of spray‐dried pristine graphene and graphene oxide sheets. *Small* **2015,** *11* (22), 2661-2668.
90. Luo, J.; Jang, H. D.; Sun, T.; Xiao, L.; He, Z.; Katsoulidis, A. P.; Kanatzidis, M. G.; Gibson, J. M.; Huang, J., Compression and aggregation-resistant particles of crumpled soft sheets. *ACS nano* **2011,** *5* (11), 8943-8949.
91. Novoselov, K. S.; Geim, A. K.; Morozov, S. V.; Jiang, D.; Zhang, Y.; Dubonos, S. V.; Grigorieva, I. V.; Firsov, A. A., Electric field effect in atomically thin carbon films. *science* **2004,** *306* (5696), 666-669.
92. Baimova, A.; Korznikova, E.; Dmitriev, S.; Liu, B.; Zhou, K., REVIEW ON CRUMPLED GRAPHENE: UNIQUE MECHANICAL PROPERTIES. *Reviews on Advanced Materials Science* **2014,** *39* (1).
93. El Rouby, W. M., Crumpled graphene: preparation and applications. *Rsc Advances* **2015,** *5* (82), 66767-66796.
94. Chiou, D.; Langrish, T.; Braham, R., The effect of temperature on the crystallinity of lactose powders produced by spray drying. *J. Food Eng.* **2008,** *86* (2), 288-293.
95. Kemp, I.; Hartwig, T.; Herdman, R.; Hamilton, P.; Bisten, A.; Bermingham, S., Spray drying with a two-fluid nozzle to produce fine particles: Atomization, scale-up, and modeling. *Drying Technol.* **2016,** *34* (10), 1243-1252.
96. Kim, T.; Jung, G.; Yoo, S.; Suh, K. S.; Ruoff, R. S., Activated graphene-based carbons as supercapacitor electrodes with macro-and mesopores. *ACS nano* **2013,** *7* (8), 6899-6905.
97. Zhou, G.-W.; Wang, J.; Gao, P.; Yang, X.; He, Y.-S.; Liao, X.-Z.; Yang, J.; Ma, Z.-F., Facile spray drying route for the three-dimensional graphene-encapsulated Fe2O3 nanoparticles for lithium ion battery anodes. *Industrial & Engineering Chemistry Research* **2013,** *52* (3), 1197-1204.
98. Luo, J.; Zhao, X.; Wu, J.; Jang, H. D.; Kung, H. H.; Huang, J., Crumpled graphene-encapsulated Si nanoparticles for lithium ion battery anodes. *The journal of physical chemistry letters* **2012,** *3* (13), 1824-1829.

99. Lin, J.; He, J.; Chen, Y.; Li, Q.; Yu, B.; Xu, C.; Zhang, W., Pomegranate-like silicon/nitrogen-doped graphene microspheres as superior-capacity anode for lithium-ion batteries. *Electrochim. Acta* **2016,** *215*, 667-673.
100. Chen, H.; Wang, S.; Liu, X.; Hou, X.; Chen, F.; Pan, H.; Qin, H.; Lam, K.-h.; Xia, Y.; Zhou, G., Double-coated Si-based composite composed with carbon layer and graphene sheets with void spaces for lithium-ion batteries. *Electrochim. Acta* **2018,** *288*, 134-143.
101. Chen, Y.; Guo, F.; Jachak, A.; Kim, S.-P.; Datta, D.; Liu, J.; Kulaots, I.; Vaslet, C.; Jang, H. D.; Huang, J., Aerosol synthesis of cargo-filled graphene nanosacks. *Nano Lett.* **2012,** *12* (4), 1996-2002.
102. Marcano, D. C.; Kosynkin, D. V.; Berlin, J. M.; Sinitskii, A.; Sun, Z.; Slesarev, A.; Alemany, L. B.; Lu, W.; Tour, J. M., Improved synthesis of graphene oxide. *ACS nano* **2010,** *4* (8), 4806-4814.
103. Hede, P. D.; Bach, P.; Jensen, A. D., Two-fluid spray atomisation and pneumatic nozzles for fluid bed coating/agglomeration purposes: A review. *Chemical Engineering Science* **2008,** *63* (14), 3821-3842.
104. Tsapis, N.; Bennett, D.; Jackson, B.; Weitz, D. A.; Edwards, D., Trojan particles: large porous carriers of nanoparticles for drug delivery. *Proceedings of the National Academy of Sciences* **2002,** *99* (19), 12001-12005.
105. Osman, A.; Goehring, L.; Patti, A.; Stitt, H.; Shokri, N., Fundamental investigation of the drying of solid suspensions. *Industrial Engineering Chemistry Research* **2017,** *56* (37), 10506-10513.
106. Ren, W.; Wang, Y.; Zhang, Z.; Tan, Q.; Zhong, Z.; Su, F., Carbon-coated porous silicon composites as high performance Li-ion battery anode materials: can the production process be cheaper and greener? *Journal of Materials Chemistry A* **2016,** *4* (2), 552-560.
107. Du, F.-H.; Ni, Y.; Wang, Y.; Wang, D.; Ge, Q.; Chen, S.; Yang, H. Y., Green fabrication of silkworm cocoon-like silicon-based composite for high-performance Li-ion batteries. *ACS nano* **2017,** *11* (9), 8628-8635.
108. Ball, V.; Del Frari, D.; Michel, M.; Buehler, M. J.; Toniazzo, V.; Singh, M. K.; Gracio, J.; Ruch, D. J. B., Deposition mechanism and properties of thin polydopamine films for high added value applications in surface science at the nanoscale. *BioNanoScience* **2012,** *2* (1), 16-34.
109. Wang, J.; Zhou, S.; Huang, J.; Zhao, G.; Liu, Y., Interfacial modification of basalt fiber filling composites with graphene oxide and polydopamine for enhanced mechanical and tribological properties. *RSC advances* **2018,** *8* (22), 12222-12231.
110. Zou, R.; Liu, F.; Hu, N.; Ning, H.; Jiang, X.; Xu, C.; Fu, S.; Li, Y.; Zhou, X.; Yan, C., Carbonized polydopamine nanoparticle reinforced graphene films with superior thermal conductivity. *Carbon* **2019,** *149*, 173-180.
111. Zhou, Y.; Guo, H.; Yong, Y.; Wang, Z.; Li, X.; Zhou, R., Introducing reduced graphene oxide to improve the electrochemical performance of silicon-based materials encapsulated by carbonized polydopamine layer for lithium ion batteries. *Materials Letters* **2017,** *195*, 164-167.

112. Yan, Y.; Xu, Z.; Liu, C.; Dou, H.; Wei, J.; Zhao, X.; Ma, J.; Dong, Q.; Xu, H.; He, Y.-s., Rational Design of the Robust Janus Shell on Silicon Anodes for High-Performance Lithium-Ion Batteries. *ACS applied materials interfaces* **2019,** *11* (19), 17375-17383.
113. Leveau, L.; Laïk, B.; Pereira-Ramos, J.-P.; Gohier, A.; Tran-Van, P.; Cojocaru, C.-S., Silicon nano-trees as high areal capacity anodes for lithium-ion batteries. *Journal of Power Sources* **2016,** *316*, 1-7.
114. Wang, B.; Ryu, J.; Choi, S.; Song, G.; Hong, D.; Hwang, C.; Chen, X.; Wang, B.; Li, W.; Song, H.-K., Folding graphene film yields high areal energy storage in lithium-ion batteries. *ACS nano* **2018,** *12* (2), 1739-1746.
115. Zhang, K.; Chen, H.; Chen, X.; Chen, Z.; Cui, Z.; Yang, B., Monodisperse silica‐polymer core‐shell microspheres via surface grafting and emulsion polymerization. *Macromolecular materials and engineering* **2003,** *288* (4), 380-385.
116. Wegewitz, L.; Prowald, A.; Meuthen, J.; Dahle, S.; Höfft, O.; Endres, F.; Maus-Friedrichs, W., Plasma chemical and chemical functionalization of polystyrene colloidal crystals. *Physical Chemistry Chemical Physics* **2014,** *16* (34), 18261-18267.
117. She, Z.; Ghosh, D.; Pope, M. A., Decorating graphene oxide with ionic liquid nanodroplets: an approach leading to energy-dense, high-voltage supercapacitors. *ACS nano* **2017,** *11* (10), 10077-10087.
118. Chang, H.; Sun, Z.; Saito, M.; Yuan, Q.; Zhang, H.; Li, J.; Wang, Z.; Fujita, T.; Ding, F.; Zheng, Z., Regulating infrared photoresponses in reduced graphene oxide phototransistors by defect and atomic structure control. *ACS nano* **2013,** *7* (7), 6310-6320.
119. Vesel, A., Modification of polystyrene with a highly reactive cold oxygen plasma. *Surface and Coatings Technology* **2010,** *205* (2), 490-497.
120. Hülser, T.; Schnurre, S.; Wiggers, H.; Schulz, C. In *Gas-phase synthesis of highly-specific nanoparticles on the pilot-plant scale*, Proceedings of world congress on particle technology (WCPT6), 2010.
121. Ruffo, R.; Hong, S. S.; Chan, C. K.; Huggins, R. A.; Cui, Y., Impedance analysis of silicon nanowire lithium ion battery anodes. *The Journal of Physical Chemistry C* **2009,** *113* (26), 11390-11398.
122. Kim, H.-W.; Lee, D. J.; Lee, H.; Song, J.; Kim, H.-T.; Park, J.-K., Glucosamine-derived encapsulation of silicon nanoparticles for high-performance lithium ion batteries. *Journal of materials chemistry a* **2014,** *2* (35), 14557-14562.
123. Guo, S.; Hu, X.; Hou, Y.; Wen, Z., Tunable synthesis of yolk–shell porous silicon@ carbon for optimizing Si/C-based anode of lithium-ion batteries. *ACS applied materials & interfaces* **2017,** *9* (48), 42084-42092.
124. Ashuri, M.; He, Q.; Shaw, L. L., Silicon as a potential anode material for Li-ion batteries: where size, geometry and structure matter. *Nanoscale* **2016,** *8* (1), 74-103.
125. Tang, X.; Wen, G.; Zhang, Y.; Wang, D.; Song, Y., Novel silicon nanoparticles with nitrogen-doped carbon shell dispersed in nitrogen-doped graphene and CNTs hybrid electrode for lithium ion battery. *Applied Surface Science* **2017,** *425*, 742-749.
126. Park, G. D.; Choi, J. H.; Jung, D. S.; Park, J.-S.; Kang, Y. C., Three-dimensional porous pitch-derived carbon coated Si nanoparticles-CNT composite microsphere with superior electrochemical performance for lithium ion batteries. *J. Alloys Compd.* **2020,** *821*, 153224.

127. Liu, Y.; Tai, Z.; Zhou, T.; Sencadas, V.; Zhang, J.; Zhang, L.; Konstantinov, K.; Guo, Z.; Liu, H. K., An All‐Integrated Anode via Interlinked Chemical Bonding between Double‐Shelled‐Yolk‐Structured Silicon and Binder for Lithium‐Ion Batteries. *Adv. Mater.* **2017,** *29* (44), 1703028.
128. Zhu, C.; Zhang, Y.; Ma, Z.; Wang, H.; Sly, G. L., Yolk-void-shell Si–C nano-particles with tunable void size for high-performance anode of lithium ion batteries. *Nanotechnology* **2020,** *32* (8), 085403.
129. Wang, F.; Wang, B.; Ruan, T.; Gao, T.; Song, R.; Jin, F.; Zhou, Y.; Wang, D.; Liu, H.; Dou, S., Construction of structure-tunable Si@ void@ C anode materials for lithium-ion batteries through controlling the growth kinetics of resin. *ACS nano* **2019,** *13* (10), 12219-12229.
130. Chen, H.; Hou, X.; Chen, F.; Wang, S.; Wu, B.; Ru, Q.; Qin, H.; Xia, Y., Milled flake graphite/plasma nano-silicon@ carbon composite with void sandwich structure for high performance as lithium ion battery anode at high temperature. *Carbon* **2018,** *130*, 433-440.
131. Ashuri, M.; He, Q.; Zhang, K.; Emani, S.; Shaw, L. L., Synthesis of hollow silicon nanospheres encapsulated with a carbon shell through sol–gel coating of polystyrene nanoparticles. *J. Sol-Gel Sci. Technol.* **2017,** *82* (1), 201-213.
132. Liang, G.; Qin, X.; Zou, J.; Luo, L.; Wang, Y.; Wu, M.; Zhu, H.; Chen, G.; Kang, F.; Li, B., Electrosprayed silicon-embedded porous carbon microspheres as lithium-ion battery anodes with exceptional rate capacities. *Carbon* **2018,** *127*, 424-431.
133. Huang, H.; Rao, P.; Choi, W. M., Carbon-coated silicon/crumpled graphene composite as anode material for lithium-ion batteries. *Current Applied Physics* **2019,** *19* (12), 1349-1354.
134. Guan, P.; Li, J.; Lu, T.; Guan, T.; Ma, Z.; Peng, Z.; Zhu, X.; Zhang, L., Facile and scalable approach to fabricate granadilla-like porous-structured silicon-based anode for lithium ion batteries. *ACS applied materials & interfaces* **2018,** *10* (40), 34283-34290.
135. Zhu, X.; Choi, S. H.; Tao, R.; Jia, X.; Lu, Y., Building high-rate silicon anodes based on hierarchical Si@ C@ CNT nanocomposite. *J. Alloys Compd.* **2019,** *791*, 1105-1113.
136. Wang, Z.; Mao, Z.; Lai, L.; Okubo, M.; Song, Y.; Zhou, Y.; Liu, X.; Huang, W., Sub-micron silicon/pyrolyzed carbon@ natural graphite self-assembly composite anode material for lithium-ion batteries. *Chem. Eng. J.* **2017,** *313*, 187-196.
137. Park, B. H.; Jeong, J. H.; Lee, G.-W.; Kim, Y.-H.; Roh, K. C.; Kim, K.-B., Highly conductive carbon nanotube micro-spherical network for high-rate silicon anode. *J. Power Sources* **2018,** *394*, 94-101.
138. Jiang, J.; Zhang, H.; Zhu, J.; Li, L.; Liu, Y.; Meng, T.; Ma, L.; Xu, M.; Liu, J.; Li, C. M., Putting Nanoarmors on Yolk–Shell Si@ C Nanoparticles: a reliable engineering way to build better Si-based anodes for Li-ion batteries. *ACS applied materials & interfaces* **2018,** *10* (28), 24157-24163.
139. Pan, Q.; Zuo, P.; Lou, S.; Mu, T.; Du, C.; Cheng, X.; Ma, Y.; Gao, Y.; Yin, G., Micro-sized spherical silicon@ carbon@ graphene prepared by spray drying as anode material for lithium-ion batteries. *J. Alloys Compd.* **2017,** *723*, 434-440.

140. Jamaluddin, A.; Umesh, B.; Chen, F.; Chang, J.-K.; Su, C.-Y., Facile synthesis of core–shell structured Si@ graphene balls as a high-performance anode for lithium-ion batteries. *Nanoscale* **2020,** *12* (17), 9616-9627.
141. He, Y.; Han, F.; Wang, F.; Tao, J.; Wu, H.; Zhang, F.; Liu, J., Optimal microstructural design of pitch-derived soft carbon shell in yolk-shell silicon/carbon composite for superior lithium storage. *Electrochim. Acta* **2021,** *373*, 137924.
142. Xie, J.; Tong, L.; Su, L.; Xu, Y.; Wang, L.; Wang, Y., Core-shell yolk-shell Si@ C@ Void@ C nanohybrids as advanced lithium ion battery anodes with good electronic conductivity and corrosion resistance. *J. Power Sources* **2017,** *342*, 529-536.
143. Zhao, H.; Xu, X.; Yao, Y.; Zhu, H.; Li, Y., Assembly of Si@ Void@ Graphene Anodes for Lithium‐Ion Batteries: In Situ Enveloping of Nickel‐Coated Silicon Particles with Graphene. *ChemElectroChem* **2019,** *6* (17), 4617-4625.
144. Chen, Y.; Guo, F.; Jachak, A.; Kim, S.-P.; Datta, D.; Liu, J.; Kulaots, I.; Vaslet, C.; Jang, H. D.; Huang, J., Aerosol synthesis of cargo-filled graphene nanosacks. *ACS nano* **2012,** *12* (4), 1996-2002.
145. Kanafi, N. M.; Rahman, N. A.; Rosdi, N. H., Citric acid cross-linking of highly porous carboxymethyl cellulose/poly (ethylene oxide) composite hydrogel films for controlled release applications. *Materials Today: Proceedings* **2019,** *7*, 721-731.
146. Luo, J.; Jang, H. D.; Sun, T.; Xiao, L.; He, Z.; Katsoulidis, A. P.; Kanatzidis, M. G.; Gibson, J. M.; Huang, J. J. A. n., Compression and aggregation-resistant particles of crumpled soft sheets. **2011,** *5* (11), 8943-8949.
147. Park, S.; An, J.; Potts, J. R.; Velamakanni, A.; Murali, S.; Ruoff, R. S., Hydrazine-reduction of graphite-and graphene oxide. *Carbon* **2011,** *49* (9), 3019-3023.
148. Al-Gaashani, R.; Najjar, A.; Zakaria, Y.; Mansour, S.; Atieh, M., XPS and structural studies of high quality graphene oxide and reduced graphene oxide prepared by different chemical oxidation methods. *Ceram. Int.* **2019,** *45* (11), 14439-14448.
149. Gao, X.; Li, J.; Xie, Y.; Guan, D.; Yuan, C., A multilayered silicon-reduced graphene oxide electrode for high performance lithium-ion batteries. *ACS applied materials & interfaces* **2015,** *7* (15), 7855-7862.
150. Su, M.; Liu, S.; Tao, L.; Tang, Y.; Dou, A.; Lv, J.; Liu, Y. J. J. o. E. C., Silicon@ graphene composite prepared by spray–drying method as anode for lithium ion batteries. **2019,** *844*, 86-90.
151. Sun, Y.; Tang, J.; Zhang, K.; Yuan, J.; Li, J.; Zhu, D.-M.; Ozawa, K.; Qin, L.-C., Comparison of reduction products from graphite oxide and graphene oxide for anode applications in lithium-ion batteries and sodium-ion batteries. *Nanoscale* **2017,** *9* (7), 2585-2595.